The Pennsylvania State University
The Graduate School

A BRITTLE DAMAGE MODEL IN THERMOELASTODYNAMICS

A Dissertation in
Engineering Science and Mechanics
by
Jonathan S. Pitt

Submitted in Partial Fulfillment
of the Requirements
for the Degree of

Doctor of Philosophy

August 2009

The dissertation of Jonathan S. Pitt was reviewed and approved* by the following:

Francesco Costanzo
Professor of Engineering Science and Mechanics
Dissertation Advisor, Chair of Committee

Joseph P. Cusumano
Professor of Engineering Science and Mechanics

Lawrence H. Friedman
Assistant Professor of Engineering Science and Mechanics

Ludmil T. Zikatanov
Associate Professor of Mathematics

Judith A. Todd
P. B. Breneman Department Head Chair,
Department of Engineering Science and Mechanics

*Signatures are on file in the Graduate School.

Abstract

The response of brittle materials subjected to dynamic thermomechanical loading is investigated. In particular, simulations are used to determine the role of material property dependence on the microstructure of a brittle material, and to determine the viability of modeling thermal phenomena associated with brittle failure within the framework of continuum damage mechanics (CDM). A system of equations is derived via the theory of internal state variables that *fully couples* the elastic, thermal, and microstructure evolution of a thermoelastic material with isotropic damage. Dynamic effects in the equations of motion and the intrinsically local nature of the constitutive equations are carefully studied.

A new implementation of the finite element method is proposed for finding approximate solutions to the derived model. The damage variable is treated as a field, as opposed to the common method of considering values of the damage at the quadrature points. In this way, the damage is treated in the general framework of finite element methods. A key element of the proposed numerical formulation is the use of a piecewise constant approximate solution space for the damage variable.

This is physically motivated; not only is the damage variable local, it is most often the result of homogenization over a representative volume element, and therefore evolves in a piecewise constant manner according to the mesh. Adaptive mesh refinement is implemented to keep the size of higher dimensional problems reasonable, and also to properly resolve the morphology of the damage field. Brittle behavior is captured by defining a minimum mesh size and allowing the damage variable to grow rapidly, as is physically the case in fracture.

Failure induced thermal heating is observed in the simulations. To the author's knowledge, this is the first presentation of such a result in the context of CDM for brittle materials. The specific heat and its dependence on the damage variable/microstructure were found to play an extremely important role in this heating. Therefore, further study (both theoretical and experimental) of the effects of failure mechanisms on the specific heat appear to be particularly important to better understand the failure of brittle materials subjected to thermomechanical loading. Specific issues in the modeling of an intrinsically discontinuous phenomena like fracture within a continuous theory are discussed.

Table of Contents

List of Figures vii

List of Tables ix

List of Symbols x

Acknowledgments xiii

Chapter 1
Background and Introduction 1

Chapter 2
Literature Review 5
2.1 Brittle Damage Models 7
2.1.1 Definition of Damage Field 8
2.1.2 Damage Field Evolution 10
2.2 Model Context 11
2.3 Thermal-Damage Relationships 16
2.4 Summary of Contribution 17

Chapter 3
Physical Model Derivation 19
3.1 Kinematics 21
3.2 Governing Equations 22
3.3 Damage Variable Evolution 27
3.4 Linear Thermoelasticity with Damage 29
3.4.1 Heat Flux Linearization 29
3.4.2 Free Energy Linearization 30

3.4.3 Equations of Motion . . . 33
3.5 High Temperature Theory . . . 34
3.5.1 Constitutive Theory . . . 34
3.5.2 High Temperature Equations of Motion . . . 39
3.6 Boundary and Initial Conditions . . . 41

Chapter 4
Numerical Methods **42**
4.1 Linear Thermoelastic-Damage IBVP . . . 43
4.1.1 Spatial Integration . . . 44
4.1.2 Time Integration . . . 47
4.2 Non-Linear Thermoelasticity-Damage IBVP . . . 52
4.2.1 Spatial Integration . . . 54
4.2.2 Time Integration . . . 55
4.3 Solution Space Selection . . . 59
4.3.1 Thermoelastic Verification . . . 60
4.3.2 Damage Variable Solution Space . . . 67
4.4 Summary and Computer Implementation . . . 72

Chapter 5
Numerical Experiments **73**
5.1 1D IBVP Description . . . 75
5.2 Exponent Parameter Study . . . 77
5.3 Damage Evolution Material Properties . . . 91
5.4 Brittle Fracture . . . 96

Chapter 6
Adaptive Mesh Refinement **100**
6.1 h-adaptive Algorithm . . . 103
6.1.1 Damage Derived Scheme . . . 105
6.1.2 Energy Release Rate Derived Scheme . . . 107
6.2 2D Compact Test Specimen . . . 109

Chapter 7
Conclusions and Future Work **118**
7.1 Summary of Work . . . 118
7.2 Findings and Conclusions . . . 120
7.3 Possible Directions for Extension . . . 121
7.3.1 Future Engineering Work . . . 122
7.3.2 Future Scientific Studies . . . 123

Appendix A
Thermoelastic Material Properties **125**

Appendix B
Non-Linear Numerical Details **130**

Appendix C
Non-Technical Abstract **133**

Bibliography **135**

List of Figures

2.1 Damage Variable Definition 9

3.1 Diagram of Kinematic Quantities 22

4.1 Example of Damage Evolution RHS 48
4.2 Linear Solver Flowchart 50
4.3 Non-Linear Solver Flowchart 56
4.4 Linear Model Convergence - $\mathcal{Q}^1$ Elements 63
4.5 Linear Model Convergence - $\mathcal{Q}^2$ Elements 65
4.6 Linear Model Convergence - $\mathcal{Q}^2$ Elements 66
4.7 Non-Linear Model Convergence - $\mathcal{Q}^2$ Elements 67
4.8 Comparison of Damage Solution Spaces 70
4.9 Damage Solution Space - Unstable $\mathcal{Q}^2$ 71

5.1 One-Dimension Problem Geometry 75
5.2 Damage and Temperature Evolution Convergence Study 77
5.3 Exponent-Damage Coupling 79
5.4 1D Space-Time Results 82
5.5 1D Space-Time Results 83
5.6 Damage Variable Evolution 84
5.7 Parameter Study - β 85
5.8 Parameter Study - α 86
5.9 Parameter Study - γ 87
5.10 Parameter Study - τ 88
5.11 Final Damage and Temperature Profiles 89
5.12 Parameter Study Detail - α 90
5.13 Parameter Study Detail - γ 91
5.14 Damage Sensitivity to G_{CR} 93
5.15 Temperature Dependence of η_C 95
5.16 Temperature Dependence of G_{CR} 96
5.17 Temperature and Damage Fields for Brittle Failure 97

5.18 Temperature and Damage Fields for Brittle Failure 98

6.1 Basic *a posteriori* AMR Scheme 104
6.2 Damage-based AMRAlgorithm 106
6.3 Energy-based AMRAlgorithm 108
6.4 2D Compact Test Specimen Setup 109
6.5 2D Initial CTS Meshes 110
6.6 Mesh Dependence of Damage: Manual Refinement 111
6.7 Mesh Dependence of Damage: Automatic Refinement 112
6.8 Refinement Indicator Comparison—Zoom Images 114
6.9 Similar Damage Solutions on Different Meshes 115
6.10 Damage and Temperature—Zoom Images 116
6.11 Example of Mesh Dependence 117

List of Tables

4.1 Linear Model Convergence - $\mathcal{Q}^1$ Elements 63
4.2 Linear Model Convergence - $\mathcal{Q}^2$ Elements 65
4.3 Damage Solution Spaces 69

5.1 Graphite Material Properties 74

List of Symbols

a	Crack propagation parameter temperature dependence exponent
b	Critical energy release rate temperature dependence exponent
$\mathbf{b}_\kappa$	Body force in the reference configuration
$\mathcal{B}_\kappa$	Reference configuration
$\mathcal{B}_t$	Deformed configuration
$\partial\mathcal{B}$	Boundary of the domain
c	Specific Heat
C	Fourth-order elasticity tensor
E	Elastic modulus
E^*	Effective elastic modulus
e_K	Error estimate for a cell K
$\mathbf{E}$	Finite strain
$\mathcal{E}$	Small strain
e_κ	Internal energy in the reference configuration
$\mathbf{F}$	Deformation Gradient
$\mathbf{H}$	Displacement Gradient
G	Energy release rate

G_{CR}	Critical energy release rate
$\mathbf{K}$	Thermal conductivity tensor
$\mathbf{M}$	Thermo-mechanical coupling tensor
$\mathbf{q}_\kappa$	Material heat flux
r_κ	Heat supply per unit volume in the reference configuration
r_K	Refinement indicator for cell K
$\mathbf{S}$	First Piola-Kirchhoff stress tensor
$\mathbf{S}_0$	Residual stress
t	Time
$\mathbf{u}$	Displacement
$\mathbf{v}$	Velocity
x	Coordinates of a point in the deformed configuration
X	Coordinates of a point in the reference configuration
α	Thermal conductivity damage dependence exponent
α_{CTE}	Isotropic coefficient of thermal expansion
β	Elastic moduli damage dependence exponent
β_{TM}	Isotropic thermomechanical coupling
γ	Thermo-mechanical coupling damage dependence exponent
Γ^D	Boundary subset subject to Dirichlet boundary conditions
Γ^N	Boundary subset subject to Neumann boundary conditions
η_κ	Entropy in the reference configuration
η_C	Crack propagation parameter
θ	Absolute temperature
θ_R	Uniform reference temperature

$\tilde{\theta}$	Difference from reference temperature
λ	Lamè parameter
μ	Lamè parameter
ν	Poisson's ratio
ρ_κ	Density in the reference configuration
ρ	Density in the deformed configuration
τ	Specific heat damage dependence exponent
ϕ	Damage variable
χ	Deformation map
ψ_κ	Helmholtz free energy in the reference configuration
ψ_0	Thermal-damage dependent free energy

Acknowledgments

I thank my advisor, Francesco Costanzo, for his guidance and constant support of my research and education. I sincerely appreciated his willingness to let me explore areas of research in which I had a particular personal interest. I would especially like to thank him for enabling me to work as a visiting graduate researcher at The International School for Advanced Studies (SISSA), in Trieste, Italy. Without our many talks about the finer points of mechanics and mathematics, the completion of this thesis would not have been possible.

Additionally, I would like to thank my committee members, Joseph Cusumano, Lawrence Friedman, and Ludmil Zikatanov, for their kind participation and additional insight during the completion of this dissertation.

I would like to acknowledge the United States Office of Naval Research for their funding throughout my degree program, under MURI Grant No. N00014-04-1-0683.

Finally, I am fortunate to have received funding during the last year of my studies through the United States Department of Defense via the Science, Mathematics, and Research for Transformation (SMART) Fellowship.

Chapter 1

Background and Introduction

The erosion and failure of carbon-carbon composite rocket nozzles is well known to be an important and limiting factor in the design of solid fuel rockets (see, e.g., Acharya and Kuo, 2007b; Cortopassi et al., 2008; Evans et al., 2007). The nozzles are subjected to extreme loading conditions, both thermal and mechanical. The loads are applied over very brief time intervals, giving rise to highly dynamic motions on the same timescale as wave propagation in the nozzle. The range of the thermal loading is often characterized by temperature differentials of over two orders of magnitude above room temperature, and the mechanical loading includes both pressures of three orders of magnitude above atmosphere in tandem with extremely high velocity impacts from particulate matter in the fuel.

It has been observed that the nozzle operating environment often erodes the nozzle throat (Evans et al., 2007), thus altering the nozzle geometry enough that the nozzle is no longer able to withstand the loading and therefore suffers sudden and catastrophic failure. While advances have been made in mitigating the throat erosion problem (Acharya and Kuo, 2007a), stress analysis techniques remain critical to the design process. Traditional stress analysis methods lack the fidelity necessary for accurate quantification of failure mechanisms in complex composite materials subjected to dynamic thermo-mechanical loading. In particular, there is a need for incorporating into the model the lessons learned in the study of dynamic fracture of materials.

In the study of dynamic fracture it is often the case that the propagation of cracks causes local thermal softening due to adiabatic heating (see, e.g., Ravi-Chandar

et al., 2000). Modeling of these phenomena is often performed by decoupling the heat equation from the balance of linear momentum, mainly to simplify the numerical analysis of the problem. However, Costanzo and Walton (2002) have shown through analysis that accounting for the thermal dependence of the fracture properties along with the full coupling between thermal and mechanical effects, while not crucial in describing the behavior of the material away from the running crack tip, might play an important role in determining the near crack-tip behavior. In other words, since fracture is highly sensitive to the failure properties of the material immediately surrounding the crack tip, it is important to properly account for the interplay of fracture and temperature at the local level. In this thesis, I intend to use Continuum Damage Mechanics (CDM) to model nucleation and dynamic evolution of microcracks up to the development of macrocracks as shown, for example, in Mazars (1996). In doing so, a damage model is derived that contains full coupling of the damage evolution with the evolution of the thermo-mechanical properties of the material.

This thesis is meant to explore the necessary modeling aspects one must account for to properly predict stress fields, damage nucleation, crack growth, and failure whenever combined thermal and mechanical effects are important. It is believed that the key to any such modeling attempt is the inclusion of full coupling between the mechanical and thermal response of the system via the balance of energy and the accounting of damage evolution in the evolution of the material's constitutive response. Owing to the brittle nature of carbon-carbon composites, thermoelasticity is selected as the framework for the model development. Failure mechanisms in carbon-carbon composites are known to be matrix microcracking, fiber breaking, and matrix-fiber debonding. A key assumption in this work is that the microstructure evolution affects both the mechanical the thermal response of the material.

CDM models abound in the literature, including some that already consider thermal phenomena and elastic-thermal-damage interaction (see, e.g., Stabler and Baker, 2000, or Tenchev and Purnell, 2005). As mentioned earlier, we believe that the nature of this problem requires a fully-coupled dynamic model via the inclusion of the full form of the balance of energy rather than a *one-way* coupling between temperature and stress. However, full thermo-mechanical-damage coupling has often been overlooked. To this end, a full derivation of a thermoelastic material with

damage is presented. In this thesis, the discussion is restricted to thermoelasticity with isotropic scalar damage, i.e., to the case of a material that would behave thermoelastically if the damage evolution were to be held frozen in a given state. The choice of isotropic damage is reasonable as long as we wish to characterize only bulk graphite, which is typically the matrix component of many carbon-carbon composite components such as rocket nozzles. The generalization of damage models applicable to composite materials is already described at length in the body of literature that exists on the use of multiple damage variables (see, for example, discussions on lists of/higher order damage variables in Voyiadjis and Kattan, 2005 or Lemaitre and Desmorat, 2005, or any textbook on CMD).

The dependence on damage of material parameters such as the specific heat, thermo-mechanical coupling,* elastic moduli, and thermal conductivities has been previously explored by Mazars and Pijaudier-Cabot (1989), and later by Stabler and Baker (2000). In the latter it is shown that the specific heat should take a logarithmic form to maintain thermodynamic consistency; however, we show that this constraint is not necessary for the specific damage evolution law corresponding to brittle fracture. Thermodynamic consistency of proposed damage models throughout the literature is not always observed, if even considered. Therefore, in this thesis it is specifically addressed as an important part of the model derivation.

An internal state variable (ISV) model, where the fields representing the state of the microstructure are assumed to be hidden from an observer and for which an evolution law must be prescribed, is employed in this dissertation.† This is done for two reasons. The first is to develop a problem which can be used to assess the performance of adaptive mesh techniques when confronted with localization of the damage field, as well as the resulting mesh-dependency of the solution. The second is to stay in context with a modeling approach that is more commonly used in the field of engineering applications of composite materials.

An original numerical method is proposed for accurately and efficiently integrating the chosen class of dynamic damage models. An operator splitting approach, such as those commonly used in plasticity damage models (see, e.g., Simo and Hughes, 1998), is employed, resulting in an algorithm that is stable without relying

*The thermomechanical coupling is related to the coefficients of thermal expansion (CTE). See Appendix A for a complete explanation.

†Other approaches, such as the theory of configurational forces, are often used as well.

on the addition of artificial stabilizing terms to the equations of motion. The numerical methods for the proper implementation of CDM models is non-trivial, and consequently a large portion of this thesis is devoted to the careful application of numerical techniques. As an additional benefit, these techniques are generalizable to many models with internal state variables.

The objectives of this thesis are the careful derivation of a constitutive framework for the study of the interplay between the evolution of damage and corresponding thermo-mechanical properties of the material, and the investigation into numerical methods that can adequately produce approximate solutions in the context of localization. The fundamental physical issues of constitutive linearization, elastic-thermal-damage coupling, and dynamic effects are investigated thoroughly. The included results simply serve the purpose of offering a "proof of concept" meant to demonstrate some capabilities of the model, along with a basic parameter study to identify which physical couplings are the most important. In this thesis, I do not intend to set forth a new damage model for a specific material, nor make claims that any one approach to modeling failure in solids is correct or superior to another. Rather, I will focus on extending existing continuum models to include the full balance of energy with dynamic effects, and demonstrate the proper derivation of such models from the point of view of ISV theory.

This dissertation is organized as follows: Chapter 2 reviews phase-field damage models, including their link to micromechanics and smaller scales, followed in Chapter 3 by a derivation of the equations of motion for two distinct initial boundary value problems. In Chapter 4 a detailed explanation of the algorithm used to find approximate solutions to the derived equations is presented, including a discussion of convergence and solution spaces for the damage variable. In Chapter 5, numerical experiments are conducted, and ultimately the importance of various physical couplings present in the model is investigated. Chapter 6 contains numerical experiments demonstrating the functionality of the adaptive meshing algorithm. A discussion of conclusions and possible extensions is presented in Chapter 7, including possible experiments for validating the implications of the work in this dissertation.

Chapter 2

Literature Review

Failure analysis and life prediction of components and structures is a fundamental responsibility of the engineering discipline. As society continues to demand safer, more efficient and increasingly innovative products, the accurate quantification of product life and design specifications becomes ever more relevant. The history of such a broad subject, with efforts dating back to at least the work of Griffith (1921), is due more consideration than allowed by the constraints to which this document must conform. Therefore, the following literature review will be limited to the background necessary for developing a continuum model describing the failure of brittle materials (those materials which predominately fail via fracture), where thermal effects are intrinsically included.

In continuum mechanics, phase-field methods use fields to describe additional properties of the material,* such as the plastic strain, porosity, or grain size. Furthermore, those models which use fields to describe some measure of damage within the material are called continuum damage models. Continuum damage mechanics (CDM) provides a framework for performing practical computations while still accounting for the detailed failure of a body at smaller scales. Within this paradigm, the additional physics of microstructure evolution are described in a continuum manner by a collection of additional fields.

A primary claim of this dissertation that, in many cases, the coupling between microstructure evolution and thermal processes cannot be ignored. As such, the

*In this thesis, additional properties are those not usually attributable to a body in general, e.g., fields other than the displacement, temperature, stress, etc. ...

focus here is on the inclusion of thermal processes as an intrinsic part of the model, and not on the traditional topics dedicated to the development of phase-field damage models. Specifically, no original claims or presentations are made regarding the fundamental definition of damage fields or their evolution; however, the effects of considering the problem in a thermoelastic setting as opposed to an isothermal elastic one are explored in depth. An enormous body of literature has been generated detailing the process by which continuous fields that describe the discreet microstructure of a material are derived. Because of this, we are able to borrow from the work of others who have thoroughly investigated the nature of phase-field damage models for brittle materials. Entire monographs exist on this topic, and are founded on well-tested methods of micromechanical analysis and experiment. Thus, the work in this dissertation exists only due to the fact that such fundamental work is readily available.

At the outset of this project, the author surveyed the literature to determine what models, if any, were available for application to the problem of rocket nozzle throat erosion. Specifically, we wanted to find models that included brittle failure mechanisms, dynamic terms, and full coupling with thermal phenomena. Finally, we of course wanted to employ models that were based on accepted physical principles, such as thermodynamic consistency.* However, we quickly realized that very few, if any, such models were already proposed.

The large majority of the damage models in the literature are quasi-static in nature. While this itself is not intrinsically negative, it is not what we needed for this project. It is probable that the tendency toward quasi-static formulations is a result of the culture of presenting stress-strain curves as an end result in many works. Knowledge of the material response is important, and useful for validation of damage models, but does not advance our needs. Thermal effects in existing models are almost without exception included only as temperature dependence of the material properties. Hence, a fixed temperature is prescribed, and the appropriate material properties (e.g., the elastic moduli) are selected. No existing models where found that have two-way coupling between damage and thermal phenomena. No models were found in which dynamic thermal events are present.

*A model is thermodynamically consistent if the formulation does not violate the second law of thermodynamics.

Perhaps the most unsettling fact about the current state of the literature is the lack of attention paid to scientific principles in many of these models. Some models were found which are not thermodynamically consistent, and even more were found which were simply 'ad-hoc' in nature. It is the point of view of the author that well-tested theoretical frameworks should be followed from the beginning when deriving a new model, and that simplifying assumptions have solid footings and clear consequences for the applicability of the model. It is the opinion of the author that in the engineering community, these principles have often and widely been overlooked. Thus, it is necessary for us to begin 'from scratch', and derive a suitable continuum model.

The remainder of this chapter proceeds as follows: an overview of CDM as applied to brittle materials, including a brief background of the development of the simple damage model employed throughout this dissertation, is given first. The methods used to provide physical meaning to the damage field are discussed, as well as the concepts needed for understanding the corresponding evolution equation. The context of the larger class of phase-field damage models, to which the model in this dissertation belongs, is presented. The efforts of others to include thermal effects in phase-field damage models and explore the coupling of thermoelastic-damage quantities are reviewed. A summary of the contribution of this dissertation to the current state of knowledge is given at the end of this chapter.

2.1 Brittle Damage Models

Clearly, the definition of a new field describing the microstructure of a body must be grounded in the physical reality of the material from which that body is constructed. Krajcinovic (1996) provides an enlightening and directing phrase in his monograph:

> "Micromechanical damage models ... should be viewed as a foundation on which the continuum damage theories must be constructed to be considered general, reliable, and rational."

From this point, we will discuss briefly the efforts of other authors to construct a link between the discreet micromechanical and continuum models. The basic tasks necessary for implementing a model describing brittle failure within the framework

of CDM are:

- Defining a damage field consistent with the physics of brittle solids (see, e.g., Krajcinovic, 1996).
- Determining the manner in which the damage field evolves, consistent with the framework of rational thermodynamics (see, e.g., Truesdell and Noll, 1965 and Coleman and Noll, 1963).

2.1.1 Definition of Damage Field

It is well known that the predominant failure mechanism in brittle materials is fracture; damage begins with the nucleation of microcracks, and ultimately ends with their coalesence into one or more macrocracks. Budiansky and O'Connell (1976) provide one of the first definitions of a continuous field describing damage due to microcracking in a brittle material. In its general form, this relation is

$$E^* = E(1-\phi), \text{ where } \phi = \frac{2N\langle a^3\rangle}{15}\left[3\langle f(\overline{\nu})\rangle + 2\langle g(\overline{\nu},\theta)\rangle\right], \tag{2.1}$$

and ϕ is a scalar field representing the extent of microcracking on a pointwise basis. Here E is the elastic modulus of an undamaged isotropic material and E^* is the effective elastic modulus. Considering the case of irreversible damage (the material is never self-healing), one always expects the effective modulus to be less than or equal to the undamaged modulus. The additional parameters in Equation (2.1) are the number of microcracks per unit volume (N), the characteristic crack dimension (a), the effective poisson's ratio ($\overline{\nu}$), a crack orientation angle (θ), and two crack geometry functions (f, g). The angle brackets $\langle\cdot\rangle$ denote the average value of the parameter over a representative volume element.

Equation (2.1) provides an example of a direct link from a micromechanics-based approach of tracking each defect to a phase-field mesoscale continuum model at the representative volume element (RVE) level. This result is achieved by applying the self-consistent method to the free energy of the system (see also Zimmerman, 1985, Horii and Nemat-Nasser, 1983 and Aboudi, 1991) which, in general, is meant to quantify how microcracking affects the free energy of a body. An important observation about (2.1) is that the damage parameter will be constant over a RVE,

as all of the functions pertaining to the direction and orientation of the cracks are averaged and N is assumed to be uniform over a given RVE. This point will prove critical in later discussions about finding approximate numerical solutions to these problems (see Chapter 4).

The variable ϕ introduced in (2.1) is a new field, referred to synonymously as either a damage variable or damage parameter (depending on the author), that quantifies the effects of microcracks on the elastic modulus. The range of the damage parameter can be deduced from (2.1) as well. Clearly, if there are no microcracks per unit volume, $\phi = 0$, and $\phi \to \infty$ as $N \to \infty$. Additionally, after some rearrangement we see that:

$$\phi = 1 - \frac{E^*}{E}, \text{ which implies } \phi \to 1 \text{ as } E^* \to 0. \tag{2.2}$$

Therefore, the physically relevant upper bound for the damage parameter is 1. Thus, as is common in the field of damage mechanics, the damage variable ϕ is restricted to the range $\phi \in [0, 1]$, where $\phi = 0$ corresponds to a material point at which there are no microcracks, and $\phi = 1$ corresponds to a material point at which the material has totally failed, i.e., a macrocrack is present (see Figure 2.1).

The brief outlining here of results from the application of the self-consistent method by Budiansky and O'Connell (1976) is meant to demonstrate that it is

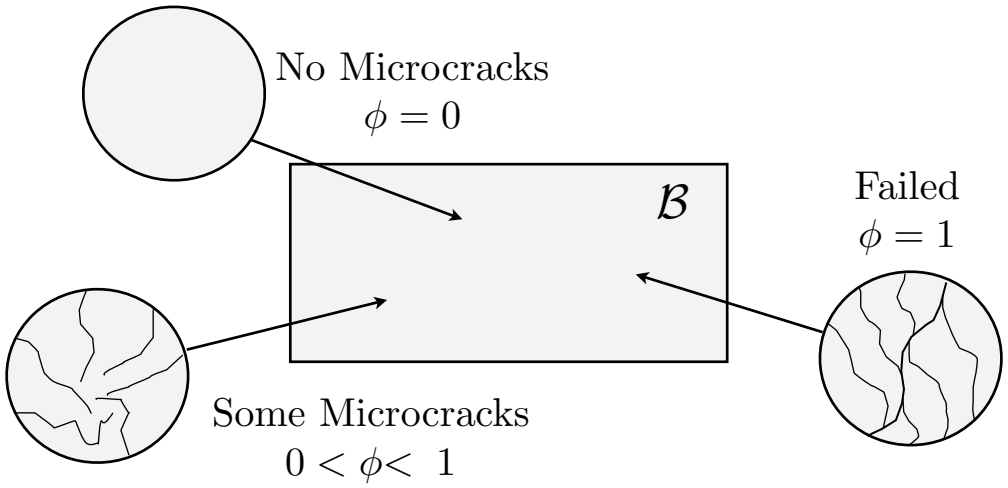

Figure 2.1. Definition of the damage field, demonstrating what the bounds on the field correspond to in the material.

possible to derive a physically reasonable definition of a damage parameter. Due to the maturity of this subject, many other definitions for damage variables describing cracking in brittle materials have been proposed (see, for example, Kachanov, 1987, and Bažant, 1986). The forthcoming chapters do not mention this material in a rigorous fashion, not because it is irrelevant, but rather because the goal of this work is to study the behavior of continuum damage models when thermal processes are introduced rather than contribute to the development of continuum damage fields from micromechanical (or smaller scale) theories.

2.1.2 Damage Field Evolution

The remainder of this section is devoted to deriving an evolution equation for the damage variable described in Section 2.1.1. Krajcinovic (1996) discusses general evolution equations for various damage models and materials, but in this thesis we have selected to use a simple, well known definition for a damage parameter. As such, we also seek to use a simple evolution equation, while simultaneously retaining concepts from fracture mechanics for brittle materials.

In this dissertation, we adapt the general evolution law describing the evolution of microcracking discussed in Caiazzo and Costanzo (2000) to obtain one that is relevant for our needs. The constitutive equation they propose has a form inspired from the field of elastic fracture mechanics,

$$\dot{\phi} = \eta_C \left\langle G - G_{CR} \right\rangle , \tag{2.3}$$

where the energy release rate, G, is defined as

$$G = -\frac{\partial \psi}{\partial \phi}. \tag{2.4}$$

Here $\eta_C > 0$ is the crack propagation parameter, G_{CR} is a critical energy release rate, ψ is the Helmholtz free energy of the body, and $\langle \cdot \rangle$ is defined as

$$\langle \zeta \rangle = \begin{cases} \zeta & \text{for } \zeta > 0, \\ 0 & \text{for } \zeta \leq 0. \end{cases} \tag{2.5}$$

Physically, this constitutive equation states that if the energy release rate with respect to the damage variable reaches some critical value, then the damage variable will increase. Likewise, it is impossible for the damage variable to decrease, and hence preserves the non-healing nature of microcracking in this model. This equation has a built-in nucleation criterion that clearly draws on the well known Griffith criterion from linear elastic fracture mechanics. Assuming the damage variable is directly related to the number of microcracks per unit volume (density) in a body, Equation (2.3) states that if the energy release rate with respect to the number of microcracks reaches a critical level, then the microcracks will begin to grow again at some rate proportional to the excess energy release rate.

The evolution equation (2.3) suits our needs well as it is defined via the Helmholtz free energy, which provides a general coupling to the theory of thermoelasticity. Therefore, if we define the free energy in terms of the thermomechanical and damage fields, then we will automatically have an evolution equation for the damage field that is fully coupled to the rest of the problem. Further comments about the physical and mathematical implications of this constitutive equation are given during the model derivation in Chapter 3 and derivation of numerical methods detailed in Chapter 4.

2.2 Model Context

In this section, the placement of this work into the larger field of CDM is identified. This is important, because different classes of models have distinct concerns during the derivation of the theory and subsequent implementation into numerical codes. Also, it is important to identify what other options are available and used in the CDM community, although not implemented in this thesis. In general, damage models can be classified by two qualities: 1) The dimension of the damage variable(s), and 2) The mathematical characteristics of the evolution equation(s).

CDM provides a framework for including the discrete microstructure of a body via a homogenized, continuous damage field, beginning with the works of Kachanov (1958) and Rabotnov (1963), both of whom developed the use of an order parameter to characterize the creep behavior of metals subject to the formation of voids. An order parameter is an additional unknown, which accounts for some additional

quality of the material. Order parameters are most often associated with phase transitions, where extrema values of the range indicate different phases of a material. For example, if for a solid-liquid phase transition problem an order parameter has the range $[0, 1]$, then the value of zero may indicate the material is in the solid phase, and the value of one would indicate that the material is in the liquid phase. Note that the concept of an order parameter is more general than that of the damage variable, as it may not have relevance to specific physical quantities, but instead is more of a pointwise indicator for the state of the system. The language in the literature is not always clear about the distinction between order parameters and damage variables/parameters; depending on the author or specific sub-field, one may find the terms used interchangeably.

A myriad of damage mechanisms have been described in this manner, and the reader is directed to the works of Capriz (1989), Lemaitre and Sermage (1997), and Voyiadjis and Kattan (2005) for an extensive listing. A survey of these works shows that the field of damage mechanics is rich in concepts and applications; however, there is a lack of communication about the scientific worthiness of the overall approach. While many articles can be found that show good performance of these models when compared to specific experiments, there is a distinct lack of validation for the overall approach. For more background information, the reader is directed to the excellent reviews of the history and theory of the subject that can be found in Chaboche (1988a,b), Kachanov (1986), Krajcinovic (1996), and Lemaitre (1996).

The damage variable defined in Section 2.1 is scalar in nature, but this is not always the case in CDM. A scalar damage variable is often referred to as an isotropic measure of damage, that is, microcracks are counted, but no preferred directionality in their orientation is assumed.* Various authors have proposed methods for introducing higher dimensional damage parameters. In particular, Ladevéze (1983), Voyiadjis and Kattan (2005), and Lemaitre et al. (2000) are among those who have discussed the concept of tensor valued damage variables to capture anisotropic damage phenomena (e.g., microcracks with preferred orientation). It is not immediately clear, however, that these matrix representations of multiple

*However, if one where to take the variables on the right-hand side of Equation (2.1) as the damage variables, then one would have a description of isotropic damage with more than one damage variable.

damage variables are in fact tensors in the strict sense, or rather just a list of order parameters as described in other works (see, for example, Fried and Gurtin, 1994 and Fried and Gurtin, 1993). This thesis does not employ lists of, or higher-ordered damage variables. Instead, a scalar damage variable is used to preserve simplicity for the sake of studying the fundamental coupling of thermoelasticity and damage.

Damage evolution equations are typically derived by either the application of the theory of internal state variables (ISV) (see, e.g., Bowen, 1989), or via an additional balance law as a result of considering the theory of configurational forces (see, e.g., Gurtin, 2000). In the theory of ISV, additional fields (such as the damage variable) are considered to be additional hidden state variables for which an evolution law must be specified. That is, they are added to the list of state variables upon which the constitutive quantities depend, and they are not directly observable or controlled via experimentation. In the theory of configurational forces, a parallel set of balance laws are employed for the forces and kinematics of physics assumed to occur at smaller scales. The behavior of the resulting equations can be grouped into two distinct classes, those which are an ordinary differential equation (ODE) with respect to time, and those which are a partial differential equation (PDE) in both time and space. Clearly, the choice of an evolution law is based on the physics of the problem, and must be made in a careful and consistent manner to ensure that thermodynamic constraints are observed. Note that either the theory of ISV or configurational forces can lead to evolution equations that are either an ODE or PDE, but some distinctions can be made.

The use of ISV methods is widespread throughout the engineering and applied sector of the CDM research community. ISV models are attractive to the engineering community because there exist very few constraints on the form which a damage evolution equation may have, making the machinery of damage mechanics applicable to a large number of problems. However, even though there are fewer restrictions on the form of the damage evolution law, abuses still occur, resulting in models that are not thermodynamically admissible (obey the second law of thermodynamics).

In the theory of internal state variables, the damage variable is considered an additional state variable, and the corresponding evolution equation an additional constitutive relation (see Bowen, 1989 and Coleman and Gurtin, 1967). In an

elastic material, simple constitutive evolution equations typically have the form

$$\dot{\phi} = f(\mathbf{F}, \phi, t), \tag{2.6}$$

where $\mathbf{F}$ is the deformation gradient, ϕ is the scalar damage variable, and t is the time. The fact that (2.6) is an ordinary differential equation in ϕ immediately leads to issues of localization and mesh-dependence of the solution ϕ. (see, e.g., Mariano, 2000a). Noticeably absent from the right-hand side of (2.6) is the gradient of the damage variable, which would make (2.6) a PDE and alleviate the issue of solution localization by introducing a spatial operator. While there is nothing in the theory of ISV preventing one from considering $\nabla\phi$ as an additional state variable, it is not always clear how to reconcile this choice with the consequences of the principle of equipresence* during the Coleman-Noll procedure (see Coleman and Noll, 1963), and as such including the gradient of the damage variable as an additional state variable is often forgone in damage models when using the theory of internal state variables.

The localization resulting from this class of models is often dealt with numerically via specialized techniques. For example, the use of a minimum mesh size is widely known to be a simple method for obtaining repeatable results. Also, additional physical arguments, such as non-local gradient methods have been proposed, but are not explored in this work (see, for example, Zbolt and Bazant, 1996, Pijaudier-Cabot and Bazant, 1988, or Voyiadjis et al., 2001). Such models are representative of the many ad-hoc gradient schemes implemented to control the localization of the damage variable. Within such schemes, gradient terms are included in the evolution equations, often with a tuning parameter to determine a region over which strain and/or damage values are averaged before use in the evolution. The definition of a tuning parameter, or characteristic length, is akin to the notion of defining a minimum mesh size.

Concepts from the theory of configurational forces have also been integrated with

*The principle of equipresence states that every constitutive relation must initially be considered to be a function of all of the state variables. For example, if the state variables are the deformation gradient and damage variable, then all of the constitutive relations need to be assumed to be functions of both state variables before the consequences of material frame indifference are realized. In this case, if the gradient of the damage is considered to be an additional state variable, then an evolution law would also need to be specified for it.

CDM, resulting in a class of models with different characteristics from those based on ISV. Generally (but not strictly), CDM models resulting from configurational force balances have evolution equations that are PDE, i.e., for an elastic material they generally have the form

$$\dot{\phi} = f(\mathbf{F}, \phi, \nabla\phi, t). \tag{2.7}$$

This is due to the balance-law structure relating the micro-stresses and micro-kinematics (see Gurtin, 2000). Many authors have explored damage models and microcracking in the setting of configurational forces, including Agiasofitou and Dascalu (2007), Augusti and Mariano (1999), Mariano (2000b), Gurtin and Podio-Guidugli (1996), and Capriz (1989). Another effect usually present in models derived via the theory of configurational forces (but again, in no manner prohibited from models derived via ISV methods) is microinertia, which is considered an important physical effect (see, e.g., Capriz, 1989 and Cermelli and Fried, 1997) when describing the material motion of the system, and leads to evolution laws of the form

$$\ddot{\phi} = f(\mathbf{F}, \phi, \nabla\phi, \dot{\phi}, t). \tag{2.8}$$

In summary, it must be stressed that it is possible to obtain evolution equations which are either ODE or PDE from either the theory of internal state variables or configurational forces, or even other methods in mechanics. However, in general, evolution equations which are ODE typically arise from the theory of internal state variables and evolution equations which arise from a balance of configurational forces are often PDE with second derivatives of the damage variable with respect to time, accouting for the microinertia. In this thesis, we have chosen to use the simplest model possible, that is, a scalar damage variable that evolves according to an ODE, within the theory of ISV. This preserves the clarity of the thermal-damage relationships in the results, as well as allows us to maintain relevance to the broader engineering community.

2.3 Thermal-Damage Relationships

To date, only a few works in the literature resembling the following presentation on elastic-thermal-damage coupling have been uncovered. The current search has focused on previous manuscripts detailing the constitutive quantities for a thermoelastic body with isotropic damage, and on any works which include the dynamic balance of energy.

A model detailing the application of a fully coupled thermoelastic theory with multiple damage parameters to the high temperature response of concrete is given by Tenchev and Purnell (2005). The authors provide for the dynamic change in temperature in the rate dependent constitutive equations for the stress, and also account for it in the local evolution equation of the damage parameter. Additionally, a particular form of the specific heat is considered, to preserve thermodynamic consistency. The entire work is limited to the framework of linear thermoelasticity, and the details of the numerical methods employed are not well described.

Both Nechnech et al. (2002) and Gawin et al. (1999) also present detailed damage models for describing the behavior of concrete of high temperatures. These articles are instructive to us in some aspects, for example Nechnech et al. (2002) gives specific information about the time stepping and radial return algorithms employed to implement the theory, and Gawin et al. (1999) discusses the boundary conditions of the problem in a proper mathematical setting. However, the theory presented in both of these works does not consider dynamic thermal effects and their effects on damage evolution. That is, they do not account for a full coupling of the temperature and damage evolution, but rather the one-way coupling of temperature into the damage evolution.

The theory applied by Tenchev and Purnell (2005) is derived in detail by Stabler and Baker (2000). Their work considers two damage variables, one representing the 'mechanical damage' and one describing the 'thermal damage'. For a system with different damage mechanisms at different temperatures, this approach may be relevant, but it is not clear that their approach is consistent with the principle of equipresence (see, e.g., Bowen, 1989). The work of Stabler and Baker (2000) discusses many of the same points as this dissertation, the most important of which is the concept that all of the constitutive properties may depend on both temperature

and damage, and the correct forms that they must have to be thermodynamically admissible. Additionally, a generalization of the theory to include high temperature effects is discussed. The derivation is very thorough, and to this date is the only article found which explicitly outlines the fully coupled equations of motion. The motivation cited by Stabler and Baker (2000) is their observation that previous works, which assumed a constant specific heat, let to a violation of the dissipation inequality (and hence the second law of thermodynamics). Perhaps the only overriding concern with this article is that the authors have approached the problem from the point of view that this must be corrected, and a specific resolution to the problem was devised. However, no mention of the effects of evolving microstructure on the heat flux, and subsequently the coefficients of thermal conductivity, is given. Our work aims to be more general and complete, and start with the basic principles of CDM and derive a model with only the most general thermodynamic constraints.

2.4 Summary of Contribution

The primary contribution of this work is the development of a general, fully coupled, dynamic, and thermodynamically consistent thermoelastic-damage model. Specifically, a total derivation of the equations of motion for a thermoelastic material with damage, from the first principles of continuum mechanics with ISV is presented, so that the full extent of the physical coupling can be realized. Additionally, we take the most general view possible when considering the constitutive properties, allowing for damage dependence of any or all of them as necessary to be compatible with experiment. It is demonstrated that this model is more general than most of those already proposed in the literature, which often take an 'ad-hoc' approach to implementing the effects of damage.

The second contribution of this work is the investigation into proper numerical methods for modeling continuum bodies with local constitutive equations. As stated previously, the mathematical problems encountered can be so treacherous that many researchers have focused on theories which eliminate them all together, or address them through various numerical techniques. This dissertation aims to demonstrate that by coupling carefully selected numerical methods with physically based parameters and techniques, one is able to find relatively reliable approximate

solutions for local constitutive equations. Specifically, we treat the entire IBVP in the general framework of the finite element method, as opposed to simply accounting for the damage variable at quadrature points, and employ adaptive mesh techniques to address the localized nature of the damage solution.

Chapter 3

Physical Model Derivation

The goal of this chapter is to derive an initial boundary value problem (IBVP) describing the motion of a body consisting of a brittle material with evolving microstructure, subjected to dynamic thermomechanical loading. Two non-linear systems of equations are derived. In the first model, we linearize the constitutive relations and the balance laws about a displacement gradient and temperature gradient free configuration which is also at a uniform reference temperature. This results in a formulation that, when the microstructure of the system is fixed, is simply linear thermoelasticity. In the second model, we do not linearize the constitutive relations and balance laws about a reference temperature, leading to a formulation that is non-linear due to the presence of damage and due to higher-order terms intrinsic to the thermoelastic nature of the problem. The latter formulation is necessary to develop an IBVP for a thermoelastic material where the material properties may be functions of both temperature and damage. Comparisons between the final equations of motion for each case are discussed.

Permanent deformation and viscous dissipation have been neglected, primarily because the material presented is interesting in its own right, but also because the inclusion of such effects has already been well studied. Throughout the following derivation, various assumptions are used to either permit the derivation to proceed, or simplify the problem without losing physical insight. For example, as is often the case in the study of brittle materials, it is appropriate to limit our model to small-strain elastic deformations. The only mode of failure considered at this time is brittle fracture resulting from the coalescence of microcracks, which is modeled via

a continuous damage variable. No healing is considered; microcracking is assumed to be irreversible and isotropic. The extension to anisotropic damage models can be carried out in a rigorous way, following well documented approaches throughout the literature (see, for example, Voyiadjis and Kattan, 2005 or Lemaitre and Desmorat, 2005).

Throughout much of the following, we will assume that various quantities are small, and through expansion of the constitutive equations into generalized series, we will arrive at linear or non-linear PDE. In both the theory which is linear when the microstructure is fixed and the one which is not, it is assumed that the temperature gradients are small, resulting in the traditional theory of Fourier heat conduction. This allows for the use of standard thermal conductivity material properties, and is necessary for the application of the model developed herein to practical problems. Secondly, the displacement gradient, and its time derivative, will always be assumed to be small, giving rise to the use of standard elastic moduli.

The difference between the two forthcoming formulations is the nature of the difference between the temperature of the body and some reference temperature. The formulation which is fully linear when the damage is fixed assumes that the difference between the temperature and the chosen (fixed) reference temperature is small, while the other does not. Due to this, the latter formulation is often referred to in this work as the 'high-temperature' theory. Note that while one derivation will be called 'linear', and the other 'high-temperature', both will be non-linear due to the presence of the damage variable, which in turn makes the material properties time dependent. Both formulations conform to the theory of internal state variables (see, e.g., Bowen, 1989), and follow the derivation of linear thermoelasticity presented in (Carlson, 1972).

This chapter is organized as follows: a description of the kinematics and damage model is presented first, followed by a derivation of the general governing equations for a thermoelastic material with isotropic damage. Subsequently, the discussion diverges; first the formulation for linear thermoelasticity with damage is presented, followed by the derivation of the high-temperature formulation. The chapter concludes with a note on boundary and initial conditions.

3.1 Kinematics

Let $\mathcal{B} \subset \mathbb{E}^3$ be a continuous body embedded in a three-dimensional Euclidean point space. The reference configuration is chosen so as to coincide with the initial configuration at time $t = 0$, and is denoted by $\mathcal{B}_\kappa$. The deformed configuration at time $t > 0$ is denoted by $\mathcal{B}_t$. Material points in the reference configuration are denoted by $X \in \mathcal{B}_\kappa$ and points in the deformed configuration are denoted by $x \in \mathcal{B}_t$. Let $\chi(X, t)$ be the motion of $\mathcal{B}$, which consists of the collection of configurations over the interval $0 \leq t \leq T$ (where T is some end time). The quantities necessary to describe the motion at time t are:

$$\chi(X,t) = \left[\mathbf{u}(X,t),\ \theta(X,t),\ \phi(X,t)\right]^T, \tag{3.1}$$

where

$$\mathbf{u}(X,t) = x - X, \tag{3.2}$$

$\mathbf{u} \in \mathbb{R}^3$ is the displacement field, $\theta \in \mathbb{R}$ is the absolute temperature field, and $\phi \in \mathbb{R}$ is a "hidden" internal state variable ISV that denotes the extent of the microcracking at a point in the reference configuration. For the purposes of this work, it is not necessary to provide a full accounting of the link between this damage parameter and a specific micromechanical model. The aim here is to study the behavior of phase-field models, and in particular the issues arising in the numerical implementation of appropriate solution schemes. Therefore, the precise nature of the homogenization techniques used to develop the phase field from the micromechanics is not needed, but the reader is referred to Chapter 2 for an overview of techniques and philosophies on the subject.

As is common in CDM, admissible values of ϕ are restricted to the interval $0 \leq \phi \leq 1$, where $\phi = 0$ corresponds to a pristine, un-microcracked material point, and $\phi = 1$ denotes total pointwise failure in the material at $X \in \mathcal{B}_\kappa$. The scalar nature of the ISV chosen here is the result of assuming that microcracking occurs in an isotropic fashion; that is, microcracks are assumed to occur equally in any orientation. Clearly this model is not sufficient for some bulk materials or composite bodies; however, it can be assumed for the following without loss of generality. The

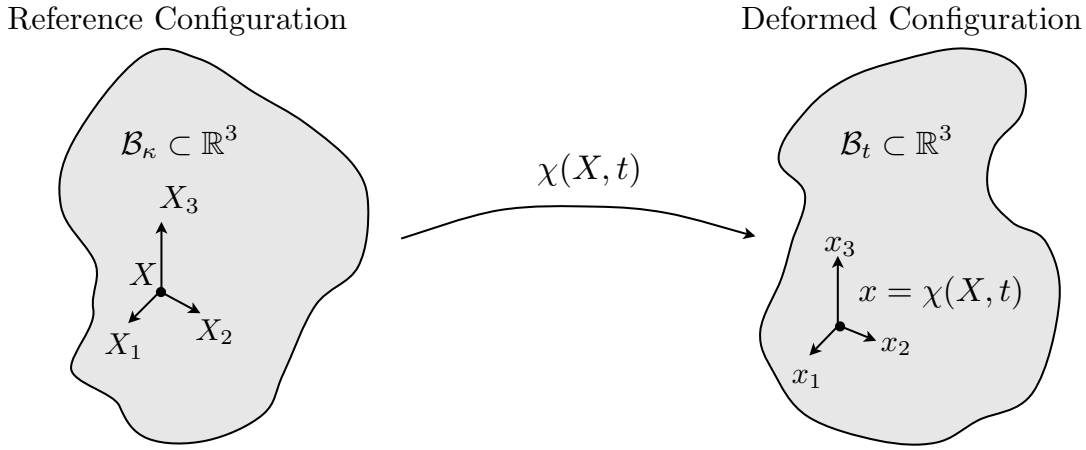

Figure 3.1. Diagram of Kinematic Quantities

deformation and displacement gradients are defined in the usual manner as

$$\mathbf{F} = \frac{\partial \chi}{\partial X} = \mathbf{I} + \mathbf{H} \quad \text{and} \quad \mathbf{H} = \nabla \mathbf{u}, \tag{3.3}$$

respectively. Here $\mathbf{I}$ is the second order identity tensor and $\nabla(\cdot)$ denotes the gradient relative to the reference configuration. The body has a mass density in the reference configuration, $\rho_\kappa(X)$, with units of mass/volume. Note that the spatial dependence of the density is explicitly declared, as modeling bodies with varying density is anticipated. Finally, define θ_R to be a constant *uniform* reference temperature over the body $\mathcal{B}$.

3.2 Governing Equations

A Lagrangian formulation is used throughout the derivation of the equations of motion. For the sake of brevity, take as given the well known balance laws of momenta and energy in referential form

$$\rho_\kappa \ddot{\mathbf{u}} = \operatorname{Div} \mathbf{S} + \mathbf{b}_\kappa, \tag{3.4}$$

$$\mathbf{S}\mathbf{F}^T = \mathbf{F}\mathbf{S}^T, \tag{3.5}$$

$$\dot{e}_\kappa + \operatorname{Div} \mathbf{q}_\kappa = \mathbf{S} \cdot \dot{\mathbf{F}} + r_\kappa. \tag{3.6}$$

Here, $\mathbf{S}$ is the first Piola-Kirchhoff stress tensor*, and $\mathbf{q}_\kappa$ is the material heat flux. The body force and heat supply per unit volume are denoted by $\mathbf{b}_\kappa(X,t)$ and $r_\kappa(X,t)$, with units of force and power per unit volume, respectively. Define the Helmholtz free energy density per unit volume of the body as:

$$\psi_\kappa = e_\kappa - \eta_\kappa \theta, \tag{3.7}$$

where e_κ is the internal energy density and η_κ is the entropy density, both per unit volume. A thermodynamically consistent model is desired, and as such we demand that for closed systems the second law of thermodynamics be satisfied:

$$\dot{\eta}_\kappa \geq \frac{r_\kappa}{\theta} - \mathrm{Div}\left(\frac{\mathbf{q}_\kappa}{\theta}\right). \tag{3.8}$$

Substituting the definition of the free energy in (3.7) and the balance of energy in (3.6) into the inequality in (3.8), the well-known dissipation inequality is obtained (see Bowen, 1989 and Carlson, 1972):

$$\dot{\psi}_\kappa + \eta_\kappa \dot{\theta} - \mathbf{S} \cdot \dot{\mathbf{F}} + \frac{1}{\theta}\mathbf{q}_\kappa \cdot \nabla\theta \leq 0. \tag{3.9}$$

The principle of equipresence (see, e.g., Bowen, 1989 and Truesdell, 1965) requires that all of the constitutive response functions depend on the same state variables. It may turn out, due to physical constraints, that some constitutive quantities do not depend on some of the state variables, but this should not be assumed *a priori* to the identification of such constraints. In thermoelasticity with an ISV, the state variables are $\mathbf{F}$, θ, $\nabla\theta$, and ϕ. The constitutive equations of the model can now be written formally as:

$$\left(\psi_\kappa, \eta_\kappa, \mathbf{S}, \mathbf{q}_\kappa, \dot{\phi}\right) = f\left(\mathbf{F}, \theta, \nabla\theta, \phi, X\right), \tag{3.10}$$

where the evolution of the ISV representing damage will be discussed shortly (see Section 3.3). More specifically, the constitutive response functions are defined as:

$$\eta_\kappa = \hat{\eta}_\kappa\left(\mathbf{F}, \theta, \nabla\theta, \phi, X\right), \tag{3.11}$$

*For general definitions, see any text on continuum mechanics, e.g., Gurtin (1981) or Liu (2002).

$$\psi_\kappa = \hat{\psi}_\kappa \left(\mathbf{F}, \theta, \nabla\theta, \phi, X\right), \tag{3.12}$$

$$\mathbf{q}_\kappa = \hat{\mathbf{q}}_\kappa \left(\mathbf{F}, \theta, \nabla\theta, \phi, X\right), \tag{3.13}$$

$$\mathbf{S} = \hat{\mathbf{S}} \left(\mathbf{F}, \theta, \nabla\theta, \phi, X\right), \tag{3.14}$$

$$\dot{\phi} = \hat{\dot{\phi}} \left(\mathbf{F}, \theta, \nabla\theta, \phi, X\right). \tag{3.15}$$

The use of a caret, $(\hat{\cdot})$, denotes the constitutive response function of a given quantity. Note again that the evolution of the damage is described by an additional constitutive response function; this is a defining characteristic of treating the damage as an internal state variable. Here, all of the response functions are permitted to be dependent on position; however, henceforth the writing of the explicit dependence on X will be dropped for notational convenience, unless it is critical to the presentation. Differentiating the free energy response function with respect to time yields

$$\dot{\hat{\psi}}_\kappa = \frac{\partial \hat{\psi}_\kappa}{\partial \mathbf{F}} \cdot \dot{\mathbf{F}} + \frac{\partial \hat{\psi}_\kappa}{\partial \theta}\dot{\theta} + \frac{\partial \hat{\psi}_\kappa}{\partial (\nabla\theta)} \cdot \nabla\dot{\theta} + \frac{\partial \hat{\psi}_\kappa}{\partial \phi}\dot{\phi}. \tag{3.16}$$

Substituting (3.16) into the dissipation inequality in (3.9) along with the rest of the constitutive response functions, gives:

$$\left(\frac{\partial \hat{\psi}_\kappa}{\partial \mathbf{F}} - \hat{\mathbf{S}}\right) \cdot \dot{\mathbf{F}} + \left(\frac{\partial \hat{\psi}_\kappa}{\partial \theta} + \hat{\eta}_\kappa\right)\dot{\theta} + \frac{\partial \hat{\psi}_\kappa}{\partial (\nabla\theta)} \cdot \nabla\dot{\theta} + \frac{\partial \hat{\psi}_\kappa}{\partial \phi}\dot{\phi} + \frac{1}{\theta}\hat{\mathbf{q}}_\kappa \cdot \nabla\theta \leq 0. \tag{3.17}$$

Since $\mathbf{F}$, θ, and $\nabla\theta$ are *independent* controllable variables in our formulation, we conclude that in order for the above variational inequality to be satisfied at all times for all admissible motions, the coefficients of the first three terms must vanish (for a formal proof of this claim, see either Bowen, 1989 or Gurtin, 1981). The result is the usual set of thermodynamic restrictions on a thermoelastic material with an ISV, namely,

$$\hat{\psi}_\kappa = \hat{\psi}_\kappa \left(\mathbf{F}, \theta, \phi\right), \qquad \hat{\eta}_\kappa = -\frac{\partial \hat{\psi}_\kappa}{\partial \theta}, \tag{3.18}$$

$$\hat{\mathbf{S}} = \frac{\partial \hat{\psi}_\kappa}{\partial \mathbf{F}}, \qquad \frac{\partial \hat{\psi}_\kappa}{\partial \phi}\dot{\phi} \leq -\frac{1}{\theta}\hat{\mathbf{q}}_\kappa \cdot \nabla\theta. \tag{3.19}$$

A full derivation of the consequences of material frame indifference is omitted here, and instead we refer the reader to the results in Carlson (1972). However, the most important consequence of material frame indifference is that the dependence of the response functions on the deformation gradient can be reduced to a dependence on the finite strain, $\mathbf{E}$, where

$$\mathbf{E} = \tfrac{1}{2}\left(\mathbf{F}^T\mathbf{F} - \mathbf{I}\right) = \tfrac{1}{2}\left(\mathbf{H} + \mathbf{H}^T + \mathbf{H}^T\mathbf{H}\right). \tag{3.20}$$

In most of the response functions, this reduces to a simple substitution, i.e.,

$$\hat{\eta}_\kappa\left(\mathbf{F}, \theta, \phi, X\right) = \tilde{\eta}_\kappa\left(\mathbf{E}, \theta, \phi, X\right), \tag{3.21}$$

$$\hat{\psi}_\kappa\left(\mathbf{F}, \theta, \phi, X\right) = \tilde{\psi}_\kappa\left(\mathbf{E}, \theta, \phi, X\right), \tag{3.22}$$

$$\hat{\mathbf{q}}_\kappa\left(\mathbf{F}, \theta, \nabla\theta, \phi, X\right) = \tilde{\mathbf{q}}_\kappa\left(\mathbf{E}, \theta, \nabla\theta, \phi, X\right), \tag{3.23}$$

$$\hat{\dot{\phi}}\left(\mathbf{F}, \theta, \nabla\theta, \phi, X\right) = \tilde{\dot{\phi}}\left(\mathbf{E}, \theta, \nabla\theta, \phi, X\right). \tag{3.24}$$

However, special care must be taken when finding the appropriate relation for the stress,

$$\hat{\mathbf{S}} = \frac{\partial\tilde{\psi}_\kappa(\mathbf{E}, \theta, \phi, X)}{\partial\mathbf{F}}, \tag{3.25}$$

which is computed using the definition of the derivative and the chain rule for tensors:

$$D_{\mathbf{F}}\tilde{\psi}_\kappa[d\mathbf{F}] = \frac{\partial\tilde{\psi}_\kappa}{\partial\mathbf{F}} \cdot d\mathbf{F} \tag{3.26}$$

$$= D_{\mathbf{E}}\tilde{\psi}_\kappa[D_{\mathbf{F}}\mathbf{E}[d\mathbf{F}]] \tag{3.27}$$

$$= \frac{\partial\tilde{\psi}_\kappa}{\partial\mathbf{E}} \cdot \frac{1}{2}(d\mathbf{F}^T\mathbf{F} + \mathbf{F}^T d\mathbf{F}) \tag{3.28}$$

$$= \frac{1}{2}\frac{\partial\tilde{\psi}_\kappa}{\partial\mathbf{E}} \cdot d\mathbf{F}^T\mathbf{F} + \frac{1}{2}\frac{\partial\tilde{\psi}_\kappa}{\partial\mathbf{E}} \cdot \mathbf{F}^T d\mathbf{F} \tag{3.29}$$

$$= \frac{1}{2}\frac{\partial\tilde{\psi}_\kappa}{\partial\mathbf{E}}\mathbf{F}^T \cdot d\mathbf{F}^T + \frac{1}{2}\mathbf{F}\frac{\partial\tilde{\psi}_\kappa}{\partial\mathbf{E}} \cdot d\mathbf{F} \tag{3.30}$$

$$= \mathbf{F}\frac{\partial\tilde{\psi}_\kappa}{\partial\mathbf{E}} \cdot d\mathbf{F}, \tag{3.31}$$

where we have taken advantage of the fact that $\mathbf{A}^T \cdot \mathbf{B}^T = \mathbf{A} \cdot \mathbf{B}$ for any tensors $\mathbf{A}$

and $\mathbf{B}$, and that $\partial\tilde{\psi}_\kappa/\partial\mathbf{E}$ is a symmetric tensor. Thus,

$$\hat{\mathbf{S}} = \mathbf{F}\tilde{\mathbf{S}}, \text{ where } \tilde{\mathbf{S}} = \frac{\partial\tilde{\psi}_\kappa}{\partial\mathbf{E}}. \tag{3.32}$$

Here $\tilde{\mathbf{S}}$ is the Second Piola-Kirchhoff stress tensor. Note that because $\mathbf{E}$ is symmetric, (3.32) causes the balance of angular momentum (3.5) to be automatically satisfied.

The complete set of non-linear governing field equations has now been derived, and consists of :

1. The kinematic relations:

$$\mathbf{F} = \mathbf{I} + \mathbf{H}, \tag{3.33}$$

$$\mathbf{E} = \frac{1}{2}\left(\mathbf{F}^T\mathbf{F} - \mathbf{I}\right). \tag{3.34}$$

2. The balance laws, see (3.4–3.6).

3. The constitutive response functions:

$$\eta_\kappa = \tilde{\eta}_\kappa\left(\mathbf{E}, \theta, \phi\right), \tag{3.35}$$

$$\psi_\kappa = \tilde{\psi}_\kappa\left(\mathbf{E}, \theta, \phi\right), \tag{3.36}$$

$$\mathbf{q}_\kappa = \tilde{\mathbf{q}}_\kappa\left(\mathbf{E}, \theta, \nabla\theta, \phi\right), \tag{3.37}$$

$$\mathbf{S} = \mathbf{F}\tilde{\mathbf{S}}\left(\mathbf{E}, \theta, \phi\right), \tag{3.38}$$

$$\dot{\phi} = \dot{\tilde{\phi}}\left(\mathbf{E}, \theta, \nabla\theta, \phi\right), \tag{3.39}$$

$$e_\kappa = \tilde{\psi}_\kappa - \tilde{\eta}_\kappa\theta. \tag{3.40}$$

4. The thermodynamic restrictions

$$\tilde{\eta}_\kappa = -\frac{\partial\tilde{\psi}_\kappa}{\partial\theta}, \quad \tilde{\mathbf{S}} = \frac{\partial\tilde{\psi}_\kappa}{\partial\mathbf{E}}, \quad \text{and} \quad \frac{\partial\tilde{\psi}_\kappa}{\partial\phi}\dot{\tilde{\phi}} + \frac{1}{\theta}\tilde{\mathbf{q}}_\kappa \cdot \nabla\theta \leq 0. \tag{3.41}$$

A precise set of governing equations can now be obtained by specifying forms for the frame-indifferent free energy ($\tilde{\psi}_\kappa$), the material heat flux ($\tilde{\mathbf{q}}_\kappa$), and damage evolution ($\dot{\tilde{\phi}}$). However, there is no *a priori* reason to suspect any specific form of the aforementioned quantities.

The balance of energy given in (3.6) can be rewritten using the results of the second law and the definition of the free energy. Recalling the definition of the internal energy

$$\tilde{e}_\kappa = \tilde{\psi}_\kappa + \tilde{\eta}_\kappa \theta, \tag{3.42}$$

the time derivative can be computed directly as

$$\dot{\tilde{e}}_\kappa = \dot{\tilde{\psi}}_\kappa + \dot{\tilde{\eta}}_\kappa \theta + \tilde{\eta}_\kappa \dot{\theta}. \tag{3.43}$$

Taking the total time derivative of the thermodynamically constrained version of the free energy density (3.18), and considering the other thermodynamic constraints, yields the following expression for the time derivative of the internal energy:

$$\dot{\tilde{e}}_\kappa = \mathbf{S} \cdot \dot{\mathbf{H}} - \tilde{\eta}_\kappa \dot{\theta} + \frac{\partial \tilde{\psi}_\kappa}{\partial \phi} \dot{\tilde{\phi}} + \dot{\tilde{\eta}}_\kappa \theta + \tilde{\eta}_\kappa \dot{\theta}. \tag{3.44}$$

Substituting this into the balance of energy (3.6), and dropping the tilde, leads to a convenient alternative expression for the balance of energy

$$\frac{\partial \psi_\kappa}{\partial \phi} \dot{\phi} + \dot{\eta}_\kappa \theta = \operatorname{Div} \mathbf{q}_\kappa + r. \tag{3.45}$$

3.3 Damage Variable Evolution

The development of an evolution law for the damage variable begins with the assumption that microcracking is an irreversible phenomenon, and thus the rate of change of the damage variable must always be non-negative:

$$\dot{\phi} \geq 0. \tag{3.46}$$

The energy release rate, with respect to the damage variable, is defined as:

$$G = -\frac{\partial \psi_\kappa}{\partial \phi}. \tag{3.47}$$

This is simply the rate at which the free energy changes with respect to the change in damage on a pointwise basis, and it is a measure of the energy (per unit volume)

available for damage growth. Because it is presumed that the damage will always increase, and that the formation of microcracks requires energy as a dissipative process with respect to the underlying thermoelastic nature of the material, the free energy will always be decreasing with respect to growing damage, and hence to have G be a positive value, we need the minus sign in (3.47).

Inspired by the Griffith criterion (see Griffith, 1921), we define $G_{CR}(\mathbf{E}, \theta, \nabla\theta, \phi)$ to be the critical energy release rate that must be met before the damage variable can grow. Thus, we have a criterion for *when* the damage variable can grow, but not *at what rate* it will grow. An elementary evolution equation for ϕ that answers this question is

$$\dot{\phi} = \eta_C \left\langle G - G_{CR} \right\rangle , \tag{3.48}$$

where $\eta_C(\mathbf{E}, \theta, \nabla\theta, \phi, X)$ is a constitutive response function that relates the excess energy release rate $G - G_{CR}$ to the time rate of microcrack growth $\dot{\phi}$. For a more detailed discussion of this evolution law, see Caiazzo and Costanzo (2000). Clearly, $\eta_C > 0$ and $G_{CR} > 0$ are additional constitutive quantities, and their proper forms are still open for debate. The effects of both damage and temperature dependence of these quantities are investigated in Chapter 5, where the specific forms are defined.

Note that η_C has a direct influence on the behavior of the model. If this value is very small, then one is essentially assuming that the damage will grow slowly. This is appropriate for materials with a high fatigue life, over-which microcracking densities grow very slowly. However, the topic of this work is brittle fracture, and as such requires that damage grows very quickly. Therefore, the focus from this point forward will be on the aspects of using very large values of η_C. To further emphasize this point, observe that as $\eta_C \to \infty$, the damage will jump to $\phi(X, 0) = 1$ for each $X \in \mathcal{B}_\kappa$ where $G > G_{CR}$ *the instant that the loading exceeds the critical threshold.*

The preservation of thermodynamic consistency is considered to be of paramount importance during this work, and as such we check that the damage evolution equation in (3.48) satisfies the thermodynamic constraints. Recalling the relevant constraint in (3.19),

$$\frac{\partial \tilde{\psi}_\kappa}{\partial \phi} \dot{\phi} \leq 0 \tag{3.49}$$

must hold for all admissible motions. Clearly, because the damage variable will never decrease, there are two distinct scenarios for this term:

1. The damage variable is not evolving ($\dot{\phi} = 0$). Thus, (3.49) is trivially satisfied.
2. The damage variable is evolving ($\dot{\phi} > 0$). If $\dot{\phi} > 0$, then $G > G_{CR} > 0$, regardless of the forms of either G or G_{CR}, as long as $\eta_C > 0$. Thus, since $G = -\partial\tilde{\psi}_\kappa/\partial\phi$, $\partial\tilde{\psi}_\kappa/\partial\phi < 0$, and (3.49) is satisfied.

Therefore, this evolution law preserves the thermodynamic consistency of the model.

3.4 Linear Thermoelasticity with Damage

The special case of linear thermoelasticity with damage is so important to this work that its derivation is now presented in full. This particular model will be very useful for preliminary analysis and eventually may be employed for preconditioning and/or predictor/corrector schemes for numerically solving the high-temperature problem. Following the traditional theory of linear thermoelasticity, we consider motions such that

$$\|\mathbf{H}\|, \|\nabla\theta\|, \|\vartheta\|, \|\dot{\mathbf{H}}\| \backsim \mathcal{O}(\delta) \tag{3.50}$$

where $\vartheta = \theta - \theta_R$ and $\delta << 1$. Following Carlson (1972), we expand the constitutive response functions about the appropriate reference state ($\mathbf{H} = \mathbf{0}$, $\nabla\theta = \mathbf{0}$, $\dot{\mathbf{H}} = \mathbf{0}$, and $\vartheta = 0$) up to terms of order δ. We then substitute the resulting linearized response functions into the balance laws and drop all of the terms of order greater than δ.

In this process, it is convenient to define the symmetric small strain tensor, $\mathcal{E}$, as the linear part of the finite strain $\mathbf{E}$ with respect to the displacement gradient $\mathbf{H}$, i.e.,

$$\mathbf{E} = \frac{1}{2}\left(\mathbf{H} + \mathbf{H}^T + \mathbf{H}^T\mathbf{H}\right) = \frac{1}{2}\left(\mathbf{H} + \mathbf{H}^T\right) + \mathcal{O}(\delta^2) = \mathcal{E} + \mathcal{O}(\delta^2). \tag{3.51}$$

3.4.1 Heat Flux Linearization

The standard procedure for linearizing the heat flux about the reference temperature gradient ($\nabla\theta = \mathbf{0}$) yields the familiar Fourier Law of heat conduction. When

expanded about $\mathbf{E} = \mathbf{0}$, $\theta = \theta_R$, and $\nabla\theta = \mathbf{0}$, the heat flux takes the form:

$$\tilde{\mathbf{q}}_\kappa(\mathbf{E}, \theta, \nabla\theta, \phi) \approx \tilde{\mathbf{q}}_\kappa(\mathbf{0}, \theta_R, \mathbf{0}, \phi) + \frac{\partial \tilde{\mathbf{q}}_\kappa(\mathbf{0}, \theta_R, \mathbf{0}, \phi)}{\partial \mathbf{E}} \cdot \mathbf{E} + \frac{\partial \tilde{\mathbf{q}}_\kappa(\mathbf{0}, \theta_R, \mathbf{0}, \phi)}{\partial \theta} \cdot \vartheta + \frac{\partial \tilde{\mathbf{q}}_\kappa(\mathbf{0}, \theta_R, \mathbf{0}, \phi)}{\partial (\nabla\theta)} \cdot \nabla\theta. \tag{3.52}$$

Assuming that $\tilde{\mathbf{q}}_\kappa$ is a smooth function of its arguments, it is possible to show that consistency with the dissipation inequality in (3.9) demands that the heat flux must vanish when the temperature gradient is zero (see Bowen, 1989) for any value of $\mathbf{E}$ and θ. In turn, this yields

$$\tilde{\mathbf{q}}_\kappa = -\mathbf{K}[\nabla\theta], \tag{3.53}$$

where the second-order heat conductivity tensor, $\mathbf{K}$, is given as:

$$\mathbf{K}(\phi, X) = -\frac{\partial \tilde{\mathbf{q}}_\kappa(\mathbf{0}, \theta_R, \mathbf{0}, \phi, X)}{\partial (\nabla\theta)}. \tag{3.54}$$

The dependence of the thermal conductivity values on the damage variable is discussed shortly.

3.4.2 Free Energy Linearization

We now wish to expand the free energy about $\mathbf{E} = \mathbf{0}$ and $\theta = \theta_R$, and retain up to and including terms that are of second order in $\mathbf{E}$ and ϑ. This form of the free energy is subsequently used to calculate the entropy and stress, which are then reduced to contain terms of only order δ. To expand and reduce the free energy to retain terms of only order δ^2 at this point is premature, and results in confusion for subsequent calculations.

$$\tilde{\psi}(\mathbf{E}, \theta, \phi) \approx \tilde{\psi}(\mathbf{0}, \theta_R, \phi) + \frac{\partial \tilde{\psi}(\mathbf{0}, \theta_R, \phi)}{\partial \mathbf{E}} \cdot \mathbf{E} + \frac{\partial \tilde{\psi}(\mathbf{0}, \theta_R, \phi)}{\partial \theta}\vartheta + \frac{1}{2}\frac{\partial^2 \tilde{\psi}(\mathbf{0}, \theta_R, \phi)}{\partial \mathbf{E} \partial \mathbf{E}}[\mathbf{E}] \cdot \mathbf{E} + \frac{1}{2}\frac{\partial^2 \tilde{\psi}(\mathbf{0}, \theta_R, \phi)}{\partial \mathbf{E} \partial \theta}\vartheta \cdot \mathbf{E} + \frac{1}{2}\frac{\partial^2 \tilde{\psi}(\mathbf{0}, \theta_R, \phi)}{\partial \theta^2}\vartheta^2. \tag{3.55}$$

Traditionally, by assuming that there is no stored energy when the body is strain free and at the reference temperature, the first term of the expansion is set to zero. However, we must make the additional assumption that the damage variable, and hence a non-uniform density of microcracks, does not give rise to recoverable mechanical energy. Furthermore, the partial derivatives present in the second and third terms in (3.55) are the stress and entropy of the undeformed body at the reference temperature, which are assumed to be zero for any given distribution of damage. Therefore, the free energy, up to and including terms of $\mathcal{O}(\delta^2)$ is:

$$\hat{\psi}(\mathcal{E}, \theta, \phi) = \frac{1}{2}\mathsf{C}[\mathcal{E}] \cdot \mathcal{E} + \mathbf{M}\vartheta \cdot \mathcal{E} - \frac{c}{2\theta_R}\vartheta^2, \tag{3.56}$$

where

$$\mathsf{C}(\phi, X) = \frac{\partial^2 \tilde{\psi}(\mathbf{0}, \theta_R, \phi)}{\partial \mathbf{E} \partial \mathbf{E}} \tag{3.57}$$

is the fourth-order elasticity tensor,

$$\mathbf{M}(\phi, X) = \frac{1}{2}\frac{\partial^2 \tilde{\psi}(\mathbf{0}, \theta_R, \phi)}{\partial \mathbf{E} \partial \theta} \tag{3.58}$$

is the second-order thermo-mechanical coupling tensor, and

$$c(\phi, X) = -\theta_R \frac{\partial^2 \tilde{\psi}(\mathbf{0}, \theta_R, \phi)}{\partial \theta^2} \tag{3.59}$$

is the specific heat capacity at constant volume. The choice of these expressions may seem arbitrary, and again the reader is referred to Carlson (1972) for further explanation.

The stress can now be computed using the thermodynamic constraint and expression for the free energy in (3.55):

$$\begin{aligned}
\hat{\mathbf{S}} &= \mathbf{F}\frac{\partial \tilde{\psi}_\kappa(\mathbf{E}, \theta, \phi)}{\partial \mathbf{E}} \\
&= (\mathbf{I} + \mathbf{H})\left(\mathsf{C}[\mathbf{E}] + \mathbf{M}\vartheta\right) \\
&= \mathsf{C}[\mathcal{E}] + \mathbf{M}\vartheta + \mathcal{O}(\delta^2) \\
&\approx \mathsf{C}[\mathcal{E}] + \mathbf{M}\vartheta.
\end{aligned} \tag{3.60}$$

Note that because $\tilde{\mathbf{S}}$ is symmetric, $\mathbf{M}$ must be symmetric, and thus the first Piola-Kirchhoff stress tensor is symmetric in the linearized theory. Furthermore, because of the symmetry of the elasticity tensor, the small strain tensor can be replaced with the displacement gradient. Considering these comments, the balance of linear momentum becomes the familiar linear expression:

$$\rho_\kappa \ddot{\mathbf{u}} = \mathrm{Div}\left[\mathsf{C}(\phi)[\nabla \mathbf{u}] + \mathbf{M}(\phi)\vartheta\right] + \mathbf{b}_\kappa. \tag{3.61}$$

What remains now is to determine the linearized form of the balance of energy. Considering the term representing the stress power and the previously derived expression for the stress response function, we have

$$\begin{aligned}
\hat{\mathbf{S}} \cdot \dot{\mathbf{F}} &= (\mathbf{I} + \mathbf{H})\left[\mathsf{C}(\phi)[\mathbf{E}] + \mathbf{M}(\phi)\vartheta\right] \cdot \dot{\mathbf{H}} \\
&= -\theta_R \mathbf{M}(\phi) \cdot \nabla \dot{\mathbf{u}} + \mathcal{O}(\delta^2) \\
&\approx -\theta_R \mathbf{M}(\phi) \cdot \nabla \dot{\mathbf{u}}.
\end{aligned} \tag{3.62}$$

As far as the linearization of e_κ is concerned, using the definition of the Helmholtz free energy, we have

$$\begin{aligned}
\tilde{e}_\kappa(\mathbf{E}, \theta, \phi) &= \tilde{\psi}_\kappa(\mathbf{E}, \theta, \phi) + \tilde{\eta}_\kappa(\mathbf{E}, \theta, \phi)\theta \\
&\approx \tilde{\psi}_\kappa(\mathbf{0}, \theta_R, \phi) + \tilde{\eta}_\kappa(\mathbf{0}, \theta_R, \phi)\theta_R + \frac{\partial \tilde{\psi}_\kappa(\mathbf{0}, \theta_R, \phi)}{\partial \mathbf{E}} \cdot \mathbf{E} \\
&\quad + \theta_R \frac{\partial \tilde{\eta}_\kappa(\mathbf{0}, \theta_R, \phi)}{\partial \mathbf{E}} \cdot \mathbf{E} + \frac{\partial \tilde{\psi}_\kappa(\mathbf{0}, \theta_R, \phi)}{\partial \theta}\vartheta + \theta_R \frac{\partial \tilde{\eta}_\kappa(\mathbf{0}, \theta_R, \phi)}{\partial \theta}\vartheta.
\end{aligned} \tag{3.63}$$

Again considering that in a deformation-free configuration at the reference temperature we expect no stored energy and no residual stress, the response function for the internal energy reduces to

$$\begin{aligned}
\tilde{e}_\kappa(\mathbf{E}, \theta, \phi) &\approx \theta_R \frac{\partial \tilde{\eta}_\kappa(\mathbf{0}, \theta_R, \phi)}{\partial \mathbf{E}} \cdot \mathbf{E} + \theta_R \frac{\partial \tilde{\eta}_\kappa(\mathbf{0}, \theta_R, \phi)}{\partial \theta}\vartheta \\
&\approx -\theta_R \frac{\partial^2 \tilde{\psi}_\kappa(\mathbf{0}, \theta_R, \phi)}{\partial \theta \partial \mathbf{E}} \cdot \mathbf{E} - \theta_R \frac{\partial^2 \tilde{\psi}_\kappa(\mathbf{0}, \theta_R, \phi)}{\partial \theta^2}\vartheta \\
&\approx -2\theta_R \mathbf{M}(\phi) \cdot \mathcal{E} + c(\phi)\vartheta.
\end{aligned} \tag{3.64}$$

Using the symmetry of $\mathbf{M}$ allows the small strain tensor to be replaced with the

displacement gradient, and the balance of energy takes the form:

$$\dot{c}(\phi)\vartheta + c(\phi)\dot{\theta} - 2\theta_R\dot{\mathbf{M}}(\phi)\cdot\nabla\mathbf{u} - \text{Div}\left[\mathbf{K}(\phi)[\nabla\theta]\right] - \mathbf{M}(\phi)\cdot\nabla\dot{\mathbf{u}} = r_\kappa. \tag{3.65}$$

At this point, we have derived four material properties that are dependent on damage, but have yet to specify that dependence. For the case of the elastic moduli, there is overwhelming literature available supporting various forms of this dependence (see Chapter 2), but for the additional material parameters of thermoelasticity, there is very little precedence. However, for the purposes of numerical experiments we must choose some concrete forms, under the constraint that they do no violate thermodynamic admissibility or basic physical common sense. In this thesis, the following expressions are assumed,

$$\mathsf{C}(\phi) = (1-\phi)^\beta\,\mathsf{C}_0, \tag{3.66}$$

$$\mathbf{M}(\phi) = (1-\phi)^\gamma\,\mathbf{M}_0, \tag{3.67}$$

$$\mathbf{K}(\phi) = (1-\phi)^\alpha\,\mathbf{K}_0, \tag{3.68}$$

$$c(\phi) = (1-\phi)^\tau\,c_0, \tag{3.69}$$

where $\alpha, \beta, \gamma, \tau \in \mathbb{R}$, and C_0, $\mathbf{M}_0$, $\mathbf{K}_0$, c_0 are the material properties when the body is undamaged. These exponents are new parameters, and serve to extend existing theories which often assume only a linear dependence.

3.4.3 Equations of Motion for the Linearized Problem

Equations (3.61) and (3.65) together with the damage evolution equation given in (3.48) give the following equations of motion for a linear thermoelastic material with simple microcracking

$$\rho_\kappa\ddot{\mathbf{u}} - \text{Div}\left[(1-\phi)^\beta\mathsf{C}_0[\nabla\mathbf{u}] + (1-\phi)^\gamma\mathbf{M}_0\vartheta\right] = \mathbf{b}_\kappa, \tag{3.70}$$

$$\begin{aligned} c_0(1-\phi)^\tau\dot{\theta} + \left[2\theta_R\gamma(1-\phi)^{\gamma-1}\mathbf{M}_0\cdot\nabla\mathbf{u} - c_0\tau(1-\phi)^{\tau-1}\vartheta\right]\dot{\phi} \\ - \text{Div}\left[(1-\phi)^\alpha\mathbf{K}_0\nabla\theta\right] - \theta_R(1-\phi)^\gamma\mathbf{M}_0\cdot\nabla\dot{\mathbf{u}} = r_\kappa, \end{aligned} \tag{3.71}$$

$$\dot{\phi} - \eta_C \left\langle \frac{\beta}{2}(1-\phi)^{\beta-1}\mathsf{C}_0[\mathbf{H}]\cdot\mathbf{H} + \gamma(\theta-\theta_R)(1-\phi)^{\gamma-1}\mathbf{M}_0\cdot\mathbf{H} - \frac{c_0\tau}{2\theta_R}(1-\phi)^{\tau-1}(\theta-\theta_R)^2 - G_{CR}\right\rangle = 0. \tag{3.72}$$

3.5 High Temperature Theory

A non-linear theory which allows for large temperature variations is presented in this section. Here we relax the assumption that the temperature variation from a reference temperature must be small, but still assume that the displacement gradient, its time derivative, and the temperature gradient are small. These assumptions retain the well documented behavior of Fourier heat conduction and linear elasticity (specifically, the use of standard elastic moduli). An additional consequence of allowing large temperature deviations from the reference temperature is that the theory now allows for temperature dependent material properties. For completeness, we assume that the displacement gradient, velocity gradient, and temperature gradient are small,

$$||\mathbf{H}||, ||\dot{\mathbf{H}}||, ||\nabla\theta|| \backsim \mathcal{O}(\delta), \text{ where } \delta << 1, \tag{3.73}$$

3.5.1 Constitutive Theory

Expanding the heat flux in a Taylor series about $\mathbf{E}=\mathbf{0}$ and $\nabla\theta=\mathbf{0}$ yields

$$\tilde{\mathbf{q}}_\kappa(\mathbf{E},\theta,\nabla\theta,\phi) \approx \tilde{\mathbf{q}}_\kappa(\mathbf{0},\theta,\mathbf{0},\phi) + \frac{\partial\tilde{\mathbf{q}}_\kappa(\mathbf{0},\theta,\mathbf{0},\phi)}{\partial\mathbf{E}}\cdot\mathbf{E} + \frac{\partial\tilde{\mathbf{q}}_\kappa(\mathbf{0},\theta,\mathbf{0},\phi)}{\partial(\nabla\theta)}\cdot\nabla\theta + \mathcal{O}(\delta^2). \tag{3.74}$$

The conditions placed on the material heat flux by the second law of thermodynamics insist only that the heat flux satisfy the dissipation inequality in (3.19). Therefore, after dropping the higher order terms and the first two terms of the expansion (which are eliminated by equilibrium conditions in linear thermoelasticity), one arrives at:

$$\tilde{\mathbf{q}}_\kappa = -\mathbf{K}[\nabla\theta], \tag{3.75}$$

where

$$\mathbf{K}(\theta, \phi, X) = -\frac{\partial \tilde{\mathbf{q}}_\kappa(\mathbf{0}, \theta, \mathbf{0}, \phi, X)}{\partial(\nabla\theta)}. \tag{3.76}$$

Here $\mathbf{K} = \mathbf{K}(\theta, \phi, X)$ is the second order heat conductivity tensor, the component values of which are dependent on both the temperature and the damage on a pointwise basis. Note that this immediately cause the equations of motion to be non-linear in the temperature, but is able to capture the physics of temperature and microstructure dependent Fourier heat conduction. The precise nature of these dependencies is outlined shortly.

The free energy of the system is expanded following the same procedure used to obtain (3.55), where first it is expanded about the finite strain, subsequently used to calculated the stress, and then reduced to contain only terms of order δ^2. Thus, expanding about $\mathbf{E} = \mathbf{0}$ yields

$$\tilde{\psi}_\kappa(\mathbf{E}, \theta, \phi) \approx \psi_0 + \mathbf{S}_0 \cdot \mathbf{E} + \frac{1}{2}\mathsf{C}[\mathbf{E}] \cdot \mathbf{E}, \tag{3.77}$$

where

$$\psi_0(\theta, \phi, X) = \tilde{\psi}_\kappa(\mathbf{0}, \theta, \phi, X), \tag{3.78}$$

$$\mathbf{S}_0(\theta, \phi, X) = \frac{\partial \tilde{\psi}_\kappa(\mathbf{0}, \theta, \phi, X)}{\partial \mathbf{E}}, \tag{3.79}$$

$$\mathsf{C}(\theta, \phi, X) = \frac{\partial^2 \tilde{\psi}_\kappa(\mathbf{0}, \theta, \phi, X)}{\partial \mathbf{E} \partial \mathbf{E}}. \tag{3.80}$$

Here ψ_0 is the part of the free energy which is solely dependent on temperature and damage, $\mathbf{S}_0$ is a second order tensor expressing the temperature and damage dependent response of the residual stress, and C is the fourth order tensor of the temperature and damage dependent elastic moduli. Note that since the finite strain tensor is symmetric, the residual stress must be symmetric and the elastic moduli will have the usual major and minor symmetries.

The residual stress is assumed to vanish, on a pointwise basis, at a reference temperature $\theta_R(X)$. Earlier, it was stated that the reference temperature must be uniform, but in this case no such restriction is necessary. Which reference

temperature is appropriate will be clear from context. Thus, if the residual stress vanishes on a pointwise basis at a given reference temperature, it must have the form

$$\mathbf{S}_0 = \mathbf{M}(\theta - \theta_R), \tag{3.81}$$

where $\mathbf{M}(\theta, \phi)$ is the temperature and damage dependent thermomechanical coupling tensor.* Considering this form for the residual stress, the stress can be calculated as

$$\begin{aligned}\mathbf{S} &= \mathbf{F}\frac{\partial \tilde{\psi}_\kappa}{\partial \mathbf{E}} \\ &= (\mathbf{I} + \mathbf{H})\left(\mathbf{M}\left(\theta - \theta_R\right) + \mathsf{C}[\mathbf{E}]\right) \\ &= (\mathbf{I} + \mathbf{H})\,\mathbf{M}\left(\theta - \theta_R\right) + \mathsf{C}[\mathbf{H}] + \mathcal{O}(\delta^2).\end{aligned} \tag{3.82}$$

The final simplification in (3.82) takes into account that the action of a symmetric fourth order tensor on a second order tensor is the same as the action on the symmetric part of the second order tensor. At this point, the balance of momenta are fully determined.

As balance of energy, here we will use the expression in (3.45), which requires us to first calculate an expression for the quantity $\dot{\eta}_\kappa$. Recalling that we have $\eta_\kappa = \tilde{\eta}_\kappa(\mathbf{E}, \theta, \phi)$, then $\dot{\eta}$ can be written as

$$\begin{aligned}\dot{\eta} &= \frac{\partial \tilde{\eta}_\kappa}{\partial \theta}\dot{\theta} + \frac{\partial \tilde{\eta}_\kappa}{\partial \mathbf{E}} \cdot \dot{\mathbf{E}} + \frac{\partial \tilde{\eta}_\kappa}{\partial \phi}\dot{\phi}, \\ &= -\frac{\partial^2 \tilde{\psi}_\kappa}{\partial \theta^2}\dot{\theta} - \frac{\partial^2 \tilde{\psi}_\kappa}{\partial \theta \partial \mathbf{E}} \cdot \dot{\mathbf{E}} - \frac{\partial^2 \tilde{\psi}_\kappa}{\partial \theta \partial \phi}\dot{\phi}.\end{aligned} \tag{3.83}$$

Recalling that

$$\tilde{\psi}_\kappa = \psi_0(\theta, \phi) + \mathbf{M}(\theta, \phi)(\theta - \theta_R) \cdot \mathbf{E} + \frac{1}{2}\mathsf{C}(\theta, \phi)[\mathbf{E}] \cdot \mathbf{E}, \tag{3.84}$$

and retaining only the terms of $\mathcal{O}(\delta)$, the following forms of the coefficents in (3.83) are obtained

$$\frac{\partial^2 \tilde{\psi}_\kappa}{\partial \theta^2} = \frac{\partial^2 \psi_0}{\partial \theta^2} + \frac{\partial^2 \mathbf{M}}{\partial \theta^2}(\theta - \theta_R) \cdot \mathbf{H} + 2\frac{\partial \mathbf{M}}{\partial \theta} \cdot \mathbf{H}, \tag{3.85}$$

*Related to the Coefficients of Thermal Expension (CTE), see Appendix A.

$$\frac{\partial^2 \tilde{\psi}_\kappa}{\partial\theta\partial\mathbf{E}} = \frac{\partial \mathbf{M}}{\partial\theta}(\theta - \theta_R) + \mathbf{M} + \frac{\partial \mathsf{C}}{\partial\theta}[\mathbf{H}], \tag{3.86}$$

$$\frac{\partial^2 \tilde{\psi}_\kappa}{\partial\theta\partial\phi} = \frac{\partial^2 \psi_0}{\partial\theta\partial\phi} + \frac{\partial^2 \mathbf{M}}{\partial\theta\partial\phi}(\theta - \theta_R)\cdot\mathbf{H} + \frac{\partial \mathbf{M}}{\partial\phi}\cdot\mathbf{H}, \tag{3.87}$$

where, for $\|\mathbf{H}\| \backsim \mathcal{O}(\delta)$, $\mathbf{M}\cdot\mathbf{E} = \mathbf{M}\cdot\mathbf{H}$, $\mathsf{C}[\mathbf{E}]\cdot[\mathbf{E}] \backsim o(\delta)$, and $\mathsf{C}[\mathbf{E}] = \mathsf{C}[\mathbf{H}]$. Provided with information about $\psi_0(\theta,\phi)$, $\mathbf{M}(\theta,\phi)$, and $\mathsf{C}(\theta,\phi)$ at the reference state ($\mathbf{E} = \mathbf{0}$), once could simply substitute (3.85)-(3.87) into the balance of energy, and have a working equation of motion. However, this is not what we expect; rather, we expect to be given information about $c_0(\theta,\phi)$, $\mathbf{M}(\theta,\phi)$, and $\mathsf{C}(\theta,\phi)$ at the reference state, where $c_0(\theta,\phi)$ is the temperature and damage dependent specific heat at constant volume at the strain-free reference state. Therefore, a bit more work is necessary to deduce $\psi_0(\theta,\phi)$ from $c_0(\theta,\phi)$.

Formally, define the specific heat in the standard way (Carlson, 1972)

$$c(\mathbf{E},\theta,\phi) = -\theta\frac{\partial^2 \psi_\kappa(\mathbf{E},\theta,\phi)}{\partial\theta^2}. \tag{3.88}$$

Combining (3.85) and the definition of the specific heat in (3.88), one can define the specific heat at the strain-free reference state as

$$c_0(\theta,\phi) := c(\mathbf{0},\theta,\phi) = -\theta\frac{\partial^2 \psi_\kappa(\mathbf{0},\theta,\phi)}{\partial\theta^2} = -\theta\frac{\partial^2 \psi_0(\theta,\phi)}{\partial\theta^2}. \tag{3.89}$$

Observing that we can now deduce $\psi_0(\theta,\phi)$ from the given specific heat at the reference configuration, and assuming that $\psi_0(\theta,\phi)$ is sufficiently smooth, we have

$$c_0(\theta,\phi) = -\theta\frac{\partial^2 \psi_0(\theta,\phi)}{\partial\theta^2}, \tag{3.90}$$

$$\frac{\partial c_0(\theta,\phi)}{\partial\phi} = -\theta\frac{\partial}{\partial\phi}\left(\frac{\partial^2 \psi_0(\theta,\phi)}{\partial\theta^2}\right), \tag{3.91}$$

$$-\frac{1}{\theta}\frac{\partial c_0(\theta,\phi)}{\partial\phi} = \frac{\partial}{\partial\theta}\left(\frac{\partial^2 \psi_0(\theta,\phi)}{\partial\theta\partial\phi}\right), \tag{3.92}$$

and hence

$$\frac{\partial^2 \psi_0(\theta,\phi)}{\partial\theta\partial\phi} = -\int \frac{1}{\theta}\frac{\partial c_0(\theta,\phi)}{\partial\phi}\, d\theta + f(\phi), \tag{3.93}$$

where $f(\phi)$ denotes a function dependent only on the damage. There is no *a priori*

reason to suspect any particular form for $f(\phi)$. To gain some insight, if one assumes that $\partial\psi_0/\partial\theta\partial\phi = 0$ at the reference state ($\mathbf{E} = 0$ and $\theta = \theta_R$), and that the specific heat and thermomechanical coupling are only functions of damage, having been measured at the reference temperature, then substituting (3.93) into (3.87) gives

$$\begin{aligned}\frac{\partial^2\psi_\kappa(\theta,\phi)}{\partial\theta\partial\phi} &= -\frac{\partial c(\theta_R,\phi)}{\partial\phi}\int_{\theta_R}^{\theta}\frac{1}{\theta}\,d\theta + \frac{\partial\mathbf{M}(\theta_R,\phi)}{\partial\phi}\cdot\mathbf{H}, \\ &= -\frac{\partial c(\theta_R,\phi)}{\partial\phi}\log\frac{\theta}{\theta_R} + \frac{\partial\mathbf{M}(\theta_R,\phi)}{\partial\phi}\cdot\mathbf{H} \qquad (3.94) \\ &\approx -\frac{\partial c(\theta_R,\phi)}{\partial\phi}\frac{\theta-\theta_R}{\theta_R} + \frac{\partial\mathbf{M}(\theta_R,\phi)}{\partial\phi}\cdot\mathbf{H}. \qquad (3.95)\end{aligned}$$

Comparing this to the expression obtained when using the fully linear free energy in (3.56), we see that the linear case has in fact been recovered,

$$\frac{\partial^2\tilde{\psi}_\kappa(\theta,\phi)}{\partial\theta\partial\phi} = \frac{\partial\mathbf{M}(\theta_R,\phi)}{\partial\phi}\cdot\mathbf{H} - \frac{\partial c(\theta_R,\phi)}{\partial\phi}\frac{(\theta-\theta_R)}{\theta_R}, \qquad (3.96)$$

and thus we decide on the final form of (3.93) as

$$\frac{\partial^2\psi_0(\theta,\phi)}{\partial\theta\partial\phi} = -\int_{\theta_R}^{\theta}\frac{1}{\theta}\frac{\partial c_0(\theta,\phi)}{\partial\phi}\,d\theta. \qquad (3.97)$$

For completeness, after dropping the explicit dependence of the material properties on the temperature and damage, (3.85-3.87) take the final form

$$\frac{\partial^2\tilde{\psi}_\kappa}{\partial\theta^2} = -\frac{1}{\theta}c_0 + \frac{\partial^2\mathbf{M}}{\partial\theta^2}(\theta-\theta_R)\cdot\mathbf{H} + 2\frac{\partial\mathbf{M}}{\partial\theta}\cdot\mathbf{H}, \qquad (3.98)$$

$$\frac{\partial^2\tilde{\psi}_\kappa}{\partial\theta\partial\mathbf{E}} = \frac{\partial\mathbf{M}}{\partial\theta}(\theta-\theta_R) + \mathbf{M} + \frac{\partial\mathsf{C}}{\partial\theta}[\mathbf{H}], \qquad (3.99)$$

$$\frac{\partial^2\tilde{\psi}_\kappa}{\partial\theta\partial\phi} = -\int_{\theta_R}^{\theta}\frac{1}{\theta}\frac{\partial c_0}{\partial\phi}\,d\theta + \frac{\partial^2\mathbf{M}}{\partial\theta\partial\phi}(\theta-\theta_R)\cdot\mathbf{H} + \frac{\partial\mathbf{M}}{\partial\phi}\cdot\mathbf{H}. \qquad (3.100)$$

Additionally, the derivative of the free energy with respect to the damage variable is needed for the balance of energy given in (3.45). Because this expression will be substituted directly into the balance of energy (3.45), we retain only the terms of

order δ, to obtain

$$\frac{\partial \psi_\kappa}{\partial \phi} = \frac{\partial \psi_0(\theta,\phi)}{\partial \phi} + \frac{\mathbf{M}(\theta,\phi)}{\partial \phi}(\theta - \theta_R)\cdot \mathbf{H}. \tag{3.101}$$

Again, we expect to be given an expression for $c_0(\theta,\phi)$, and not $\psi_0(\theta,\phi)$, so we deduce $\partial\psi_0(\theta,\phi)/\partial\phi$ from $c_0(\theta,\phi)$. Recalling (3.90),

$$\begin{aligned} c_0(\theta,\phi) &= -\theta \frac{\partial^2 \psi_0(\theta,\phi)}{\partial \theta^2}, \\ -\frac{1}{\theta}\frac{c_0(\theta,\phi)}{\partial \phi} &= \frac{\partial}{\partial \phi}\left(\frac{\partial^2 \psi_0(\theta,\phi)}{\partial \theta^2}\right) = \frac{\partial^2}{\partial \theta^2}\left(\frac{\partial \psi_0(\theta,\phi)}{\partial \phi}\right), \end{aligned} \tag{3.102}$$

and therefore,

$$\frac{\partial \psi_0}{\partial \phi} = -\int_{\theta_R}^{\theta}\int_{\theta_R}^{\theta} \frac{1}{\theta}\frac{\partial c_0(\theta,\phi)}{\partial \phi}\, d\theta\, d\theta. \tag{3.103}$$

3.5.2 High Temperature Equations of Motion

Substituting (3.82) into (3.4), as well as (3.98-3.100) and (3.101) into (3.45), we arrive at the full equations of motion for a thermoelastic material undergoing small strains, small temperature gradients, and with evolving microstructure.

$$\rho_\kappa \ddot{\mathbf{u}} - \mathrm{Div}\left[(\mathbf{I}+\mathbf{H})\mathbf{M}\,(\theta-\theta_R) + \mathsf{C}[\mathbf{H}]\right] = \mathbf{b}_\kappa, \tag{3.104}$$

$$\begin{aligned} &\left(c - \theta\frac{\partial^2 \mathbf{M}}{\partial \theta^2}(\theta-\theta_R)\cdot\mathbf{H} - 2\theta\frac{\partial \mathbf{M}}{\partial \theta}\cdot\mathbf{H}\right)\dot{\theta} - \left(\theta\frac{\partial \mathbf{M}}{\partial \theta}(\theta-\theta_R) + \theta\mathbf{M}\right)\cdot\dot{\mathbf{H}} \\ &+\left(\theta\int_{\theta_R}^{\theta}\frac{1}{\theta}\frac{\partial c}{\partial \phi}d\theta - \iint_{\theta_R}^{\theta}\frac{1}{\theta}\frac{\partial c}{\partial \phi}\, d\theta d\theta - \left(\frac{\partial \mathbf{M}}{\partial \phi}\theta_R + \theta\frac{\partial^2 \mathbf{M}}{\partial \theta \partial \phi}(\theta-\theta_R)\right)\cdot\mathbf{H}\right)\dot{\phi} \\ &\qquad - \mathrm{Div}\left[\mathbf{K}[\nabla\theta]\right] = r_\kappa, \end{aligned} \tag{3.105}$$

$$\dot{\phi} - \eta_C\left\langle \iint_{\theta_R}^{\theta}\frac{1}{\theta}\frac{\partial c}{\partial \phi}\, d\theta d\theta - \frac{\partial \mathbf{S}_0}{\partial \phi}\cdot\mathbf{E} - \frac{1}{2}\frac{\partial \mathsf{C}}{\partial \phi}[\mathbf{E}]\cdot\mathbf{E} - G_{CR}\right\rangle = 0 \tag{3.106}$$

The most important observation about (3.104)–(3.106) is that these equations do contain terms of $\mathcal{O}(\delta^2)$ which have not been removed from the balance laws.

This results in a semi-linear formulation, and is done for convenience. Comparing the above to the equations of motion for the fully linear case, we notice that the equations for the balance of momentum are of the same general form. In fact, if one were to assume that the temperature variation is also small, and that the thermomechanical coupling tensor and elastic moduli tensor are not functions of temperature, but instead measured at the reference temperature, one would recover the linear case.

To this point, the dependence of material properties on the temperature and damage has been left in a general form. Commonly, experimental data for material property dependence on temperature would be used to determine the proper relation, but, owing to the general nature of this work, we do not consider a specific material. Instead, we consider the fact that at a minimum, the material properties would be given at discrete temperature values. If this information is available, a simple piecewise linear interpolation function of temperature can be constructed for the material property in question, thus we can define the following material parameters

$$\mathbf{K}(\theta,\phi) = \mathbf{K}_i(\phi) + \mathbf{K}_{i+1}(\phi)\theta, \tag{3.107}$$

$$\mathsf{C}(\theta,\phi) = \mathsf{C}_i(\phi) + \mathsf{C}_{i+1}(\phi)\theta, \tag{3.108}$$

$$\mathbf{M}(\theta,\phi) = \mathbf{M}_i(\phi) + \mathbf{M}_{i+1}(\phi)\theta, \tag{3.109}$$

$$c_0(\theta,\phi) = (c_0)_i(\phi) + (c_0)_{i+1}(\phi)\theta, \tag{3.110}$$

where the subscript i denotes the value of a constitutive property at the i-th temperature value used in the experimental measurements. If the values of $\mathbf{K}$ are known at θ_1 and θ_2, then $(K_0)_{ij}$ and $(K_1)_{ij}$ are computed via

$$(K_1)_{ij} = \frac{K_{ij}(\theta_2) - K_{ij}(\theta_1)}{\theta_2 - \theta_1} \quad \text{and} \quad (K_0)_{ij} = K_{ij}(\theta_2) - (K_1)_{ij}\theta_2. \tag{3.111}$$

Note that this formulation assumes that each component of the various tensor-valued material properties varies linearly, but this clearly may not be the case. However, without a loss of generality we can proceed. The final question for the constitutive quantities is the dependence on damage. Using the same argument as in the linear theory, which assumes a simplest damage coupling, we arrive at the

final form of the constitutive equations

$$\mathbf{K}(\theta,\phi) = (1-\phi)^{\alpha}\left(\mathbf{K}_0 + \mathbf{K}_1\theta\right), \tag{3.112}$$

$$\mathsf{C}(\theta,\phi) = (1-\phi)^{\beta}\left(\mathsf{C}_0 + \mathsf{C}_1\theta\right), \tag{3.113}$$

$$\mathbf{M}(\theta,\phi) = (1-\phi)^{\gamma}\left(\mathbf{M}_0 + \mathbf{M}_1\theta\right), \tag{3.114}$$

$$c(\theta,\phi) = (1-\phi)^{\tau}\left(c_0 + c_1\theta\right), \tag{3.115}$$

With these relationships, Equations (3.104-3.106) are now fully defined.

3.6 Boundary and Initial Conditions

Boundary and initial conditions have been largely neglected to this point, but it is important to mention them before moving forward with the numerical implementation. The boundary of the body $\mathcal{B}$ is denoted by $\partial\mathcal{B}$ and is partitioned in the following manner

$$\partial\mathcal{B} = \Gamma^D_{\mathbf{u}} \cup \Gamma^N_{\mathbf{u}} = \Gamma^D_{\theta} \cup \Gamma^N_{\theta}. \tag{3.116}$$

Here $\Gamma^D_{(\cdot)}$ denotes the portion of the boundary subject to Dirichlet conditions, and $\Gamma^N_{(\cdot)}$ denotes the portion of the boundary subject to Neumann conditions for the subscripted unknown. Note that there are no boundary conditions for the damage parameter, as it is governed only by an ODE with respect to time. Physically, this means that the damage on the boundary is treated in the same manner as the interior, and will simply evolve as necessary.

Initial conditions for the displacement, velocity, and temperature are considered to be smooth and compatible with the boundary conditions and loading at time zero. Initial conditions for the damage are intentionally allowed to be discontinuous. Finally, we require that any set of initial conditions corresponds to an equilibrium state of the system so as not to induce discontinuities in the time dependent response of the system.

Chapter 4

Numerical Methods

This chapter details the numerical techniques employed to find approximate solutions to the initial boundary value problems derived in the previous chapter. Significant care is required to develop an algorithm that will yield trustworthy solutions. Linear thermoelasticity in itself is known to be challenging when solved numerically, as it consists of a very stiff set of partial differential equations (PDE). The addition of damage into the physics of the problem results in a non-linear system of PDE coupled to an ordinary differential equation (ODE) which describes the evolution of the damage. Furthermore, when the high-temperature theory is considered, the problem gains extra complexity from the now nonlinear nature intrinsic to the thermoelastic part of the problem.

The damage evolution ODE is of course free of spatial operators on the damage variable, allowing for localization of the damage variable in the solution. While this may be beneficial to the effort of modeling brittle fracture, it becomes somewhat problematic for obtaining reliable calculations. The numerical solutions exhibit a pathological dependence on the mesh used in the spatial discretization; that is, different discretizations of the same domain may produce radically different solutions. Further complicating the matter is that the right-hand side of the damage evolution is continuous, but not always differentiable. These problems are addressed through the judicious use of time stepping schemes, appropriate approximate solution spaces, and adaptive mesh refinement (AMR).

In this thesis, the damage variable is truly considered to be an additional field within the formulation. This differs significantly from many other implementations

in the engineering community, where the damage variable is stored as an internal variable defined at the quadrature point level. While this is familiar (the same process is used through the field of computational plasticity to store the plastic strain and hardening parameters), and permits easy implementation in commercial codes via user defined constitutive routines, it does not treat the IBVP in a manner consistent with a more general framework of finite element methods. Commercial finite element packages lack the functionality to solve this problem in the manner desired. The only commercial finite element analysis (FEA) software package the author is aware of and has access to which permits the definition of arbitrary equations of motion is Comsol Multiphysics. However, Comsol does not support adaptive mesh refinement with a dynamic solver, and does not support the time integration schemes and approximate solution spaces (i.e., discontinuous finite elements) that will be shown to be critical to obtaining reliable calculations. Therefore, we proceed with an original numerical formulation and subsequently implement it into a custom computer program.

In this chapter, the application of the Finite Element Method (FEM) to the IBVP resulting from the theory of the fully-linear thermoelastic material with damage is detailed first, leading to a system of ODE. An original two-step staggered algorithm for performing the time integration of the subsequent ODE is explained. The necessary changes to handle the high-temperature theory are discussed. A key point of the presentation is the selection of the approximate solutions spaces (i.e., the specific finite elements) necessary to obtain a stable solution. An outline of the computer implementation of the overall algorithm is given, summarizing how parallel techniques are used to improve performance of the code. Convergence results are given throughout the chapter.

4.1 Linear Thermoelastic-Damage IBVP

The theory that is fully-linear when damage is fixed at a given state, becomes non-linear, solely because of the damage variable, when the damage is evolving. Additionally, the damage variable will always be increasing. Therefore, it is natural to look for an algorithm that will, with some trade-off, reduce the non-linear problem into a series of linear ones, and ensure that the damage parameter will

monotonically increase. To not design an algorithm in this manner can lead to serious problems with the approximate solutions, as the author has discovered through much trial and error.

For example, if one naively applies the well know Newton-Raphson method to the entire system of equations, it is quite possible that the solutions which minimize the residual may actual have the damage decrease from one time-step to the next. While small fluctuations may be acceptable, there is not room for decreases that lead to negative values of the damage, which is what the author has encountered. Additionally, the use of inappropriate time-stepping schemes or combinations of finite elements can lead to instability in the solution, usually manifesting themselves in non-physical temperature variations or non-physical damage evolutions. Thus, while the approach described in this chapter may be able to be improved upon, it was selected only after many failures were encountered, as the only one which met the basic criteria of monotonically increasing temperature and stable solutions to the thermoelastic fields.

A semi-discrete approach, where the finite element method is used to perform the spatial integration, resulting in a system of ODE to be discretized by a finite difference method, is used in this algorithm. The application of the finite element method to the equations of motion is shown first. This is followed by the two step operator-splitting style algorithm to perform the integration of the resulting ODE in time. Key points are the selection of the approximate solution space for the damage variable, and method of time integration.

4.1.1 Spatial Integration

Let us begin by restating the IBVP for the case of linear thermoelasticity with damage. Throughout the following the velocity ($\mathbf{v}$) has been introduced to convert the system of PDE into a first order system in time. Let $\mathcal{B}$ be the domain, with the boundary partitioned such that

$$\partial\mathcal{B} = \Gamma^D_{\mathbf{u}} \cup \Gamma^N_{\mathbf{u}} = \Gamma^D_{\mathbf{v}} \cup \Gamma^N_{\mathbf{v}} = \Gamma^D_{\theta} \cup \Gamma^N_{\theta}. \tag{4.1}$$

Here $\Gamma^D_{(\cdot)}$ denotes the portion of the boundary subject to Dirichlet conditions, and $\Gamma^N_{(\cdot)}$ denotes the portion of the boundary subject to Neumann conditions for the

subscripted unknown. Note that there are no boundary conditions for the damage parameter, as it is governed only by an ODE with respect to time. The field equations are:

$$\dot{\mathbf{u}} - \mathbf{v} = \mathbf{0} \tag{4.2}$$

$$\rho_\kappa \dot{\mathbf{v}} - \text{Div}\left[(1-\phi)^\beta \mathsf{C}[\nabla \mathbf{u}] + (1-\phi)^\gamma \mathbf{M}(\theta - \theta_R)\right] = \mathbf{b}_\kappa, \tag{4.3}$$

$$\begin{aligned} c(1-\phi)^\tau \dot{\theta} + \left[2\theta_R \gamma (1-\phi)^{\gamma-1} \mathbf{M} \cdot \nabla \mathbf{u} - c\tau(1-\phi)^{\tau-1}(\theta - \theta_R)\right] \dot{\phi} \\ - \text{Div}\left[(1-\phi)^\alpha \mathbf{K}[\nabla \theta]\right] - (1-\phi)^\gamma \theta_R \mathbf{M} \cdot \nabla \mathbf{v} = r_\kappa, \end{aligned} \tag{4.4}$$

$$\dot{\phi} - \eta_C \left\langle -\frac{\partial \psi}{\partial \phi} - G_{CR} \right\rangle = 0, \tag{4.5}$$

where

$$\begin{aligned} -\frac{\partial \psi_\kappa}{\partial \phi} = \frac{\beta}{2}(1-\phi)^{\beta-1} \mathsf{C}[\nabla \mathbf{u}] \cdot \nabla \mathbf{u} + \gamma (1-\phi)^{\gamma-1}(\theta - \theta_R)\mathbf{M} \cdot \nabla \mathbf{u} \\ - \frac{c\tau}{2\theta_R}(1-\phi)^{\tau-1}(\theta - \theta_R)^2. \end{aligned} \tag{4.6}$$

The initial conditions for the displacement, velocity, and temperature are smooth, while the initial microstate may be anywhere from uniform to randomly distributed.

Let $\xi(t) = [\mathbf{u}(t), \mathbf{v}(t), \theta(t), \phi(t)]^T \in \mathcal{V} \times [0, T]$ be a solution to the IBVP above, where

$$\mathcal{V} = H^1_{\Gamma^D_{\mathbf{u}}}(\mathcal{B})^3 \times H^1_{\Gamma^D_{\mathbf{u}}}(\mathcal{B})^3 \times H^1_{\Gamma^D_{\theta}}(\mathcal{B}) \times L^2(\mathcal{B}), \tag{4.7}$$

is an infinite dimensional function space and T is some fixed end time. Note that this space is comprised of the cartesian product of Sobolev spaces, which conform to the imposed Dirichlet boundary conditions for the associated unknown, and the space of square integrable functions for the damage parameter. If we view the system of equations (4.2)-(4.6) in the abstract form of the action of an operator on $\xi(t)$,

$$\mathcal{F}(\xi(t)) = 0, \tag{4.8}$$

we can then concisely write the problem's weak form as: Find $\xi(t) \in \mathcal{V} \times [0, T]$ such that:

$$(\mathcal{F}(\xi(t)), \zeta) := \int_{\mathcal{B}} \mathcal{F}(\xi(t)) \cdot \zeta \; d\mathcal{B} = 0 \quad \forall \zeta \in \mathcal{V}, \quad \forall t \in [0, T], \tag{4.9}$$

where $(\cdot,\cdot)$ is the inner product on $\mathcal{V}$. As is customary with the Ritz-Galerkin Method (see, e.g., Brenner and Scott, 1994 or Eriksson et al., 1996), we now introduce a finite dimensional space $\mathcal{V}_h \subset \mathcal{V}$, and let $\xi_h \in \mathcal{V}_h$ denote an element from this space. We let $\Xi = \{[\varphi^i, \varphi^i, \varpi^i, \varsigma^i]\}$ denote a basis for $\mathcal{V}_h$ (i.e., span$(\Xi) = \mathcal{V}_h$), where φ^i are vector valued with dimension equal to the physical space dimension, and ϖ^i, ς^i are scalar valued functions of position. Due to the nature of the physical problem, we do not immediately expect that the same same basis functions will be necessary, or even satisfactory, for the different equations of motion. Therefore, we have left the definition of Ξ as general as possible, with the only assumption being that the basis functions for the displacement and velocity will be the same. This is done purely because it seems physically unreasonable to have them not be the same. The precise definition of Ξ will be explored in Section 4.3, where it is demonstrated that not every choice of solution space combinations results in a stable formulation.

We can now reformulate the weak form of the partially discretized problem: Find $\xi_h(t) \in \mathcal{V}_h \times [0,T]$ such that:

$$\left(\mathcal{F}(\xi_h(t)), \Xi^i\right) = 0 \quad \forall \Xi^i \in \Xi, \quad \forall t \in [0,T], \tag{4.10}$$

where $\xi_h(t) = [\mathbf{u}_h, \mathbf{v}_h, \theta_h, \phi_h]^T$ and the trial functions have the form

$$\mathbf{u}_h = U^j(t)\varphi^j(X), \quad \mathbf{v}_h = V^j(t)\varphi^j(X), \tag{4.11}$$

$$\theta_h = \Theta^j(t)\varpi^j(X), \quad \phi_h = \Phi^j(t)\varsigma^j(X). \tag{4.12}$$

To perform concrete numerical simulations, we will have to determine the details of Equation (4.10). This is achieved by substituting (4.2)-(4.6) and (4.11-4.12) into (4.10). The result can be clearly summarized in matrix form.

$$\begin{bmatrix} M & 0 & 0 & 0 \\ 0 & M^\rho & 0 & 0 \\ 0 & 0 & M^c & 0 \\ 0 & 0 & 0 & M^\phi \end{bmatrix} \begin{bmatrix} \dot{U}^j \\ \dot{V}^j \\ \dot{\Theta}^j \\ \dot{\Phi}^j \end{bmatrix} + \begin{bmatrix} 0 & -M & 0 & 0 \\ A^E & 0 & B & 0 \\ D & -B^T & A^K & 0 \\ 0 & 0 & 0 & 0 \end{bmatrix} \begin{bmatrix} U^j \\ V^j \\ \Theta^j \\ \Phi^j \end{bmatrix} = \begin{bmatrix} 0 \\ F_i^{\mathbf{v}} \\ F_i^\theta \\ F_i^\phi \end{bmatrix} \tag{4.13}$$

$$M_{ij} = (\varphi^i, \varphi^j) \qquad\qquad M^\rho_{ij} = (\rho_\kappa \varphi^i, \varphi^j) \tag{4.14}$$

$$D_{ij} = \left(2\theta_R\gamma\dot{\phi}_h(1-\phi)^{\gamma-1}\mathbf{M}\cdot\nabla\varphi^j, \varpi^i\right) \quad M^{\phi}_{ij} = (\varsigma^j, \varsigma^i) \tag{4.15}$$

$$A^E_{ij} = \left((1-\phi_h)^{\beta}\mathsf{C}[\nabla\varphi^j], \nabla\varphi^i\right) \quad B_{ij} = \left((1-\phi_h)^{\gamma}\mathbf{M}\varpi^j, \nabla\varphi^i\right) \tag{4.16}$$

$$B^T_{ij} = \left(\theta_R(1-\phi_h)^{\gamma}\mathbf{M}\cdot\nabla\varphi^j, \varpi^i\right) \quad M^c_{ij} = \left(c(1-\phi_h)^{\tau}\varpi^j, \varpi^i\right) \tag{4.17}$$

$$A^K_{ij} = \left((1-\phi_h)^{\alpha}\mathbf{K}[\nabla\varpi^j], \nabla\varpi^i\right) - \left(c\tau\dot{\phi}_h(1-\phi_h)^{\tau-1}\varpi^j, \varpi^i\right) \tag{4.18}$$

$$F^{\mathbf{v}}_i = (\mathbf{b}, \varphi^i) + \left(\theta_R(1-\phi_h)^{\gamma}\mathbf{M}, \nabla\varphi^i\right) + \left(\mathbf{s}^p, \varphi^i\right)_A \tag{4.19}$$

$$F^{\theta}_i = \left(r, \varpi^i\right) - \left(c\tau\theta_R\dot{\phi}_h(1-\phi_h)^{\tau-1}, \varpi^i\right) + \left(q^p, \varpi^i\right)_A \tag{4.20}$$

$$F^{\varphi}_i = \left(\eta_C\left\langle G_h - G_{CR}\right\rangle, \varsigma^i\right) \tag{4.21}$$

where

$$G_h = \frac{\beta}{2}(1-\phi_h)^{\beta-1}\mathsf{C}[\nabla\mathbf{u}_h]\cdot\nabla\mathbf{u}_h + \gamma(1-\phi_h)^{\gamma-1}(\theta_h-\theta_R)\mathbf{M}\cdot\nabla\mathbf{u}_h - \frac{c\tau}{2\theta_R}(1-\phi_h)^{\tau-1}(\theta_h-\theta_R)^2. \tag{4.22}$$

Clearly, for a nonlinear system like the one presented in Chapter 3, there is no unique way to write the system in matrix form. This particular organization has been selected to benefit the decoupling of the problem for the time integration scheme. Inspection of (4.13) reveals two sources of non-linearites. In the equations relating to the thermoelastic part of the problem, the non-linearity is caused solely by the damage parameter, while the damage evolution ODE is fully nonlinear in both the damage parameter and thermoelastic quantities.

4.1.2 Time Integration

A staggered time integration algorithm is well suited for taking advantage of the specific nonlinear properties of the system. The values of the unknowns for the next time step are found sequentially, rather than simultaneously. In general, we will explicitly calculate the values of the damage variable at the next timestep, and then use these values to make an implicit calculation for the values of the thermoelastic quantities at the next timestep. In this manner, the non-linear and monotonically increasing nature of the damage evolution equation is addressed, and the need for an energy preserving implicit method for the equations of thermoelasticity is satisfied. Note that this approach is the reverse of many standard algorithms

for integrating systems resulting from continuum models with internal variables, such as plasticity (see, for example, Simo and Hughes, 1998), where an elastic predictor-internal variable corrector scheme is often implemented. As mentioned earlier, this approach is chosen over the application of a Newton-Raphson scheme, which would require, at a minimum, the inclusion of constraints on the damage parameter. This approach is likely to perform better and be less error-prone then the coding of a constrained non-linear solver.

The overall approach of the time integration algorithm is to split the calculation of the current time step values for the damage and thermoelastic quantities. The algorithm is as follows, where n denotes the time step number. A flow-chart of the algorithm is also given in Figure 4.2.

1. Solve explicitly for $\Phi^{j,n+1} = \mathcal{F}_1(\Phi^{j,n}; U^{j,n}, V^{j,n}, \Theta^{j,n})$ using the first order accurate forward Euler method, where $\mathcal{F}_1$ is $\mathcal{F}$ when $\dot{u}$, $\dot{v}$, and $\dot{\theta}$ are set to zero. A simple explicit algorithm is chosen because the right-hand side of the damage evolution equation is non-smooth, as illustrated in Figure 4.1, and is not captured appropriately by the use of higher order methods.

Additionally, it is expected that for brittle materials the damage will grow quickly, such that in the course of a few timesteps the damage may evolve from its initial value to its final value of $\phi = 1$. The choice of a first order Euler method, and the resulting stability and accuracy problems, are thus not a major concern. The primary problem encountered with the use of higher order schemes is the artificial decreasing of the damage variable, sometimes even into the realm of negative values. Such non-physical behavior can be avoided by using this method; however, it is certainly acknowledged that this procedure may not be the optimal or unique

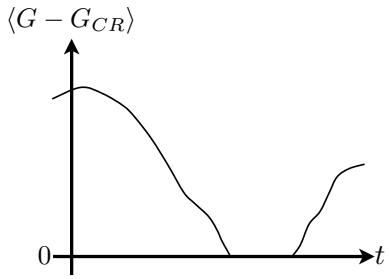

Figure 4.1. Illustration of the behavior of the damage evolution equation's RHS.

remedy.

The resulting linear system that is solved for the damage is

$$M_{ij}^{\phi}\Phi^{j,n+1} = M_{ij}^{\phi}\Phi^{j,n} + \Delta t F_i^{\phi,n} \tag{4.23}$$

where

$$F_i^{\phi,n} = \left(\eta_C^n \left\langle G_h^n - G_{CR}^n \right\rangle, \varsigma^i\right) \tag{4.24}$$

and

$$G_h^n = \frac{\beta}{2}(1-\phi_h^n)^{\beta-1}\mathsf{C}[\nabla \mathbf{u}_h^n]\cdot\nabla\mathbf{u}_h^n + \gamma(1-\phi_h^n)^{\gamma-1}(\theta_h^n-\theta_R)\mathbf{M}\cdot\nabla\mathbf{u}_h^n - \frac{c\tau}{2\theta_R}(1-\phi_h^n)^{\tau-1}(\theta_h^n-\theta_R)^2. \tag{4.25}$$

This formulation allows for easy implementation of temperature or damage dependence of η_C^n and G_{CR}^n, which are of course both time dependent. An additional consideration when using an explicit method for a field with a fixed range is that one must be careful not to let the field deviate from the fixed range. In this situation, it is possible that through either a slightly too large timestep or unexpected material properties that the damage can 'overshoot' the upper limit of $\phi = 1$. For this reason, the algorithm must contain a check to see if damage has exceeded $\phi = 1$ at any location, and if so, project it back into the realm of legitimate physical meaning.

2. Solve implicitly for

$$[U^{j,n+1}, V^{j,n+1}, \Theta^{j,n+1}] = \mathcal{F}_2\left(U^{j,n+1}, V^{j,n+1}, \Theta^{j,n+1}; U^{j,n}, V^{j,n}, \Theta^{j,n}, \Phi^{j,n+1}, \Phi^{j,n}\right), \tag{4.26}$$

where $\mathcal{F}_2$ is $\mathcal{F}$ when $\dot{\phi}$ is set to zero.

Note that since we already have the values of $\Phi^{j,n+1}$, the resulting system is linear. However, in such a system the matrices and right-hand side are not constant, so that some additional care must be exercised when implementing this process

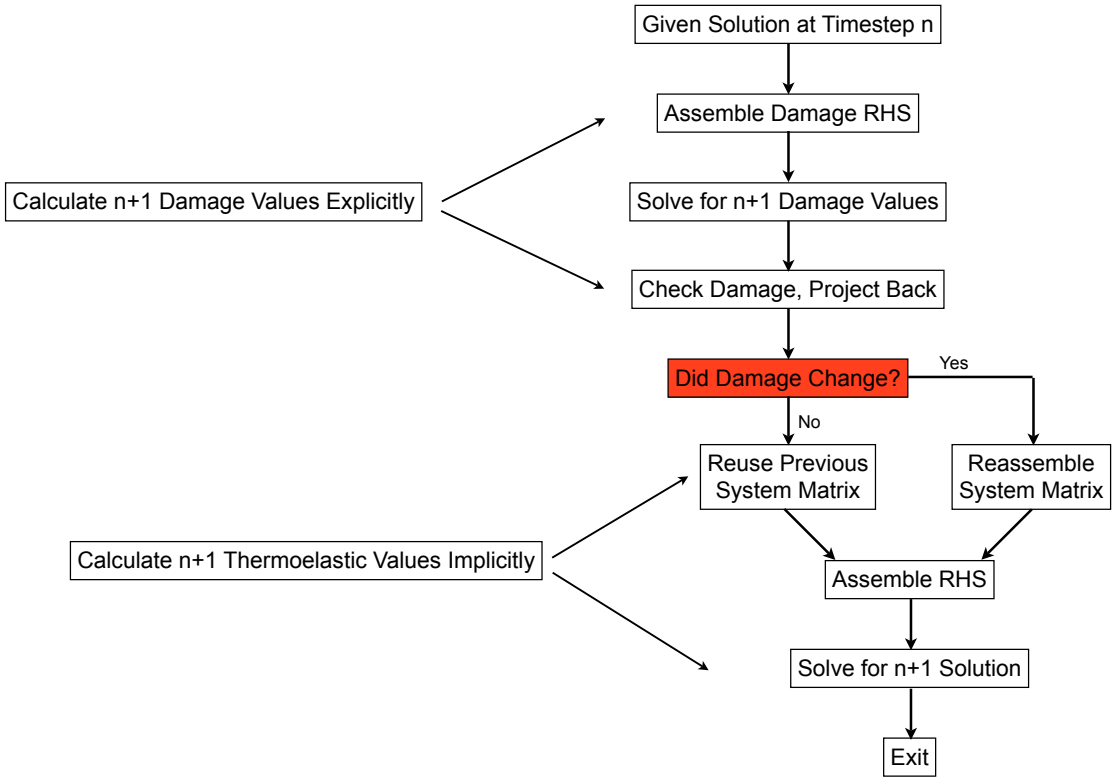

Figure 4.2. Flow-chart of the time-stepping algorithm for the theory which is fully-linear when the damage is at a fixed state. The red background of a box indicates that it is a logical step in the algorithm.

into a computer code. The system we wish to solve is:

$$\begin{bmatrix} M & 0 & 0 \\ 0 & M^{\rho} & 0 \\ 0 & 0 & M^{c} \end{bmatrix} \begin{bmatrix} \dot{U}^{j} \\ \dot{V}^{j} \\ \dot{\Theta}^{j} \end{bmatrix} + \begin{bmatrix} 0 & -M & 0 \\ A^{E} & 0 & B \\ -D & -B^{T} & A^{K} \end{bmatrix} \begin{bmatrix} U^{j} \\ V^{j} \\ \Theta^{j} \end{bmatrix} = \begin{bmatrix} 0 \\ F^{v} \\ F^{\theta} \end{bmatrix}, \tag{4.27}$$

which can be more compactly written as:

$$\mathcal{M}\dot{\xi} + \mathcal{K}\xi = \mathcal{F}, \tag{4.28}$$

where $\mathcal{M}$ is the mass matrix on the left-hand side of (4.27), $\mathcal{K}$ is the stiffness matrix on the left-hand side of (4.27), and where $\mathcal{F} = [0, F^{v}, F^{\theta}]^{T}$. Applying the Crank-Nicholson scheme (see, e.g., Quarteroni et al., 2000) to the above yields the

discrete form of (4.27),

$$\left(\mathcal{M}^{n+1}+\frac{\Delta t}{2}\mathcal{K}^{n+1}\right)\xi^{n+1}=\left(\mathcal{M}^{n+1}-\frac{\Delta t}{2}\mathcal{M}^{n+1}\left(\mathcal{M}^{n}\right)^{-1}\mathcal{K}^{n}\right)\xi^{n} + \frac{\Delta t}{2}\left(\mathcal{F}^{n+1}+\mathcal{M}^{n+1}\left(\mathcal{M}^{n}\right)^{-1}\mathcal{F}^{n}\right). \tag{4.29}$$

Note that the mass matrix ($\mathcal{M}$) and the stiffness matrix ($\mathcal{K}$) are dependent on the time step only through the damage variable, which, due to the staggered solution algorithm, is now simply a parameter. The difficulty in dealing with (4.29) lies in the fact that it contains the term

$$\mathcal{M}^{n+1}\left(\mathcal{M}^{n}\right)^{-1}, \tag{4.30}$$

in which the inverse of the mass matrix must be known. Examining this product more closely reveals the following simplification

$$\mathcal{M}^{n+1}\left(\mathcal{M}^{n}\right)^{-1}=\begin{bmatrix} I & 0 & 0 \\ 0 & I & 0 \\ 0 & 0 & (M^{c})^{n+1}\left((M^{c})^{n}\right)^{-1} \end{bmatrix}. \tag{4.31}$$

In the most general situation, the inverse of the mass matrix for the balance of energy would need to be computed at each timestep for which the damage is evolving. In the calculations presented in this paper the specific heat was assumed to be uniform over the chosen spatial domain. In this case, (4.31) takes on the following simpler form

$$\mathcal{M}^{n+1}\left(\mathcal{M}^{n}\right)^{-1}=\begin{bmatrix} I & 0 & 0 \\ 0 & I & 0 \\ 0 & 0 & c_{\text{eff}}I \end{bmatrix}, \tag{4.32}$$

where

$$c_{\text{eff}}=\frac{c^{n+1}}{c^{n}}=\left(\frac{1-\phi^{n+1}}{1-\phi^{n}}\right)^{\tau}. \tag{4.33}$$

Therefore, so long as we assume uniformity of the specific heat over each cell, the effect of this term will simply be a scalar multiplication against the necessary matrix

blocks in the system matrix and right-hand side. Of course, if the specific heat is free of dependence on the damage (i.e., $\tau = 0$), then c_{eff} is always one. Finally, the time-step is chosen based on the concepts of the Courant-Friedrichs-Lewy (CFL) limit (again, see Quarteroni et al., 2000); we employ the wavespeed to determine the time-step via

$$\Delta t = \min_{K \in \mathcal{T}_h} \frac{h_K}{4} \sqrt{\frac{\rho(X_K^{\text{center}})}{\mu(X_K^{\text{center}})}}. \tag{4.34}$$

Here K denotes a cell in the triangulation, $\mathcal{T}_h$, or discretized form, of the domain $\mathcal{B}$, and μ is the shear modulus. For completeness, the final system matrix is

$$\mathcal{A}^{n+1} = \left(\mathcal{M}^{n+1} + \sigma \mathcal{K}^{n+1}\right) = \begin{bmatrix} M & -\sigma M & 0 \\ \sigma A^E & M^\rho & \sigma B \\ \sigma D & -\sigma B^T & M^c + \sigma A^K \end{bmatrix}, \tag{4.35}$$

where $\sigma = \Delta t/2$. Only general preconditioning is implemented at this time, and sparse direct linear solvers are used whenever possible, but it is clear that the problem may benefit from a custom preconditioner. Additionally, the lower right block of the system matrix, $M^c + \sigma A^K$, will develop zero values as individual cells become fully damaged, for values of $\tau > 0$.

4.2 Non-Linear Thermoelasticity-Damage IBVP

The numerical methods for the high-temperature theory employ the operator-splitting time-stepping algorithm detailed in the section for the fully-linear theory; however, due to the now intrinsically non-linear nature of the thermoelastic part of the problem, a Newton-Raphson like scheme must be added to the overall algorithm. The nature of the governing equations and the Newton method add a considerable amount of complexity to the algorithm. Recalling the equations of motion for the high-temperature theory, we introduce the velocity ($\mathbf{v}$), and convert the equations to a first order system in time

$$\dot{\mathbf{u}} - \mathbf{v} = \mathbf{0} \tag{4.36}$$

$$\rho_\kappa \dot{\mathbf{v}} - \text{Div}\left[(\mathbf{I} + \nabla \mathbf{u})\mathbf{M}\left(\theta - \theta_R\right) + \mathsf{C}[\mathbf{H}]\right] = \mathbf{b}_\kappa, \tag{4.37}$$

$$\left(c - 2\theta\frac{\partial \mathbf{M}}{\partial \theta}\cdot\nabla\mathbf{u}\right)\dot{\theta} - \left(\theta\frac{\partial \mathbf{M}}{\partial \theta}(\theta-\theta_R)+\theta\mathbf{M}\right)\cdot\nabla\mathbf{v} - \mathrm{Div}\left[\mathbf{K}[\nabla\theta]\right] +$$
$$\left(\theta\int_{\theta_R}^{\theta}\frac{1}{\theta}\frac{\partial c}{\partial \phi}d\theta - \iint_{\theta_R}^{\theta}\frac{1}{\theta}\frac{\partial c}{\partial \phi}d\theta d\theta - \left(\frac{\partial \mathbf{M}}{\partial \phi}\theta_R + \theta\frac{\partial^2 \mathbf{M}}{\partial\theta\partial\phi}(\theta-\theta_R)\right)\cdot\nabla\mathbf{u}\right)\dot{\phi} = r_\kappa, \quad (4.38)$$
$$\dot{\phi} - \eta_C\left\langle \iint_{\theta_R}^{\theta}\frac{1}{\theta}\frac{\partial c}{\partial \phi}d\theta d\theta - \frac{\partial \mathbf{M}}{\partial \phi}(\theta-\theta_R)\cdot\nabla\mathbf{u} - \frac{1}{2}\frac{\partial \mathsf{C}}{\partial \phi}[\nabla\mathbf{u}]\cdot\nabla\mathbf{u} - G_{CR}\right\rangle = 0, \quad (4.39)$$

where the material properties are

$$\mathbf{K}(\theta,\phi) = (1-\phi)^{\alpha}\left(\mathbf{K}_0 + \mathbf{K}_1\theta\right), \quad (4.40)$$
$$\mathsf{C}(\theta,\phi) = (1-\phi)^{\beta}\left(\mathsf{C}_0 + \mathsf{C}_1\theta\right), \quad (4.41)$$
$$\mathbf{M}(\theta,\phi) = (1-\phi)^{\gamma}\left(\mathbf{M}_0 + \mathbf{M}_1\theta\right), \quad (4.42)$$
$$c(\theta,\phi) = (1-\phi)^{\tau}\left(c_0 + c_1\theta\right), \quad (4.43)$$

as defined in Chapter 3. Substituting the material properties into (4.36)-(4.39) yields the equations of motion totally in terms of the unknowns, given body forces, and given material properties

$$\dot{\mathbf{u}} - \mathbf{v} = \mathbf{0}, \quad (4.44)$$
$$\rho_\kappa\dot{\mathbf{v}} - \mathrm{Div}\left[(\mathbf{I}+\nabla\mathbf{u})(1-\phi)^{\gamma}(\mathbf{M}_0+\mathbf{M}_1\theta)(\theta-\theta_R) + (1-\phi)^{\beta}(\mathsf{C}_0+\mathsf{C}_1\theta)[\nabla\mathbf{u}]\right] = \mathbf{b}_\kappa, \quad (4.45)$$
$$\begin{aligned}&((1-\phi)^{\tau}(c_0+c_1\theta) - 2\theta(1-\phi)^{\gamma}\mathbf{M}_1\cdot\nabla\mathbf{u})\dot{\theta}\\ &\quad - \mathrm{Div}\left[(1-\phi)^{\alpha}(\mathbf{K}_0+\mathbf{K}_1\theta)[\nabla\theta]\right]\\ &\quad - (\theta(1-\phi)^{\gamma}(\mathbf{M}_0+\mathbf{M}_1(2\theta-\theta_R)))\cdot\nabla\mathbf{v}\\ &\quad + \left(\gamma(1-\phi)^{\gamma-1}(\mathbf{M}_0\theta_R+\mathbf{M}_1\theta^2)\cdot\nabla\mathbf{u}\right)\dot{\phi}\\ &\quad - \left(\tau(1-\phi)^{\tau-1}(c_0(\theta-\theta_R)+c_1(\theta^2-\theta_R^2)/2)\right)\dot{\phi} = r_\kappa,\end{aligned} \quad (4.46)$$
$$\begin{aligned}\dot{\phi} - \eta_C\Big\langle &-\tau(1-\phi)^{\tau-1}\left[c_0\left(\theta\log\left(\theta/\theta_R\right)-(\theta-\theta_R)\right)+c_1\left(\theta-\theta_R\right)^2/2\right]\\ &+\gamma(1-\phi)^{\gamma-1}(\theta-\theta_R)(\mathbf{M}_0+\mathbf{M}_1\theta)\cdot\nabla\mathbf{u}\\ &+\frac{\beta}{2}(1-\phi)^{\beta-1}(\mathsf{C}_0+\mathsf{C}_1\theta)[\nabla\mathbf{u}]\cdot\nabla\mathbf{u}] - G_{CR}\Big\rangle = 0.\end{aligned} \quad (4.47)$$

Traditionally, to define a Newton-Raphson scheme for iteratively solving a non-linear system of equations, one needs to define a residual as a function of a given solution, and a corresponding jacobian that is also a function of the solution at the current iteration.

4.2.1 Spatial Integration

To begin, we again treat (4.44)–(4.47) as an abstract operator $\mathcal{F}$ acting on the solution $\xi(t) = [\mathbf{u}(t), \mathbf{v}(t), \theta(t), \phi(t)]^T \in \mathcal{V} \times [0, T]$, where

$$\mathcal{V} = H^1_{\Gamma^D_{\mathbf{u}}}(\mathcal{B})^3 \times H^1_{\Gamma^D_{\mathbf{u}}}(\mathcal{B})^3 \times H^1_{\Gamma^D_{\theta}}(\mathcal{B}) \times L^2(\mathcal{B}), \tag{4.48}$$

and write the equations of motion as

$$\mathcal{F}(\xi(t)) = 0. \tag{4.49}$$

The problem's weak form can then be concisely written as: Find $\xi(t) \in \mathcal{V} \times [0, T]$ such that:

$$(\mathcal{F}(\xi(t)), \zeta) := \int_{\mathcal{B}} \mathcal{F}(\xi(t)) \cdot \zeta \; d\mathcal{B} = 0 \quad \forall \zeta \in \mathcal{V}, \quad \forall t \in [0, T], \tag{4.50}$$

Again, introduce a finite dimensional space $\mathcal{V}_h \subset \mathcal{V}$, and let $\xi_h \in \mathcal{V}_h$ denote an element from this space. We let $\Xi = \{[\varphi^i, \varphi^i, \varpi^i, \varsigma^i]\}$ denote a basis for $\mathcal{V}_h$ (i.e., $\text{span}(\Xi) = \mathcal{V}_h$), where φ^i are vector valued with dimension equal to the physical space dimension, and ϖ^i, ς^i are scalar valued functions of position. The discrete version of the weak form of the problem is then: Find $\xi_h(t) \in \mathcal{V}_h \times [0, T]$ such that:

$$\left(\mathcal{F}(\xi_h(t)), \Xi^i\right) = 0 \quad \forall \Xi^i \in \Xi, \quad \forall t \in [0, T], \tag{4.51}$$

where $\xi_h(t) = [\mathbf{u}_h, \mathbf{v}_h, \theta_h, \phi_h]^T$ and the trial functions have the same form

$$\mathbf{u}_h = U^j(t)\varphi^j(X), \quad \mathbf{v}_h = V^j(t)\varphi^j(X), \tag{4.52}$$

$$\theta_h = \Theta^j(t)\varpi^j(X), \quad \phi_h = \Phi^j(t)\varsigma^j(X). \tag{4.53}$$

Substituting (4.52)-(4.53) and (4.44)-(4.47) into (4.51), we arrive at a matrix form of (4.51)

$$\begin{bmatrix} M & 0 & 0 & 0 \\ 0 & M^{\rho} & 0 & 0 \\ 0 & 0 & M^{c} & 0 \\ 0 & 0 & 0 & M^{\phi} \end{bmatrix} \begin{bmatrix} \dot{U}^j \\ \dot{V}^j \\ \dot{\Theta}^j \\ \dot{\Phi}^j \end{bmatrix} = \begin{bmatrix} F_i^{\mathbf{u}} \\ F_i^{\mathbf{v}} \\ F_i^{\theta} \\ F_i^{\phi}, \end{bmatrix} \tag{4.54}$$

where the matrix and vector blocks are defined as

$$M_{ij} = (\varphi^i, \varphi^j), \qquad M^{\rho}_{ij} = (\rho_\kappa \varphi^i, \varphi^j), \qquad M^{\phi}_{ij} = (\varsigma^j, \varsigma^i), \tag{4.55}$$

$$M^c_{ij} = ([(1-\phi_h)^{\tau}(c_0 + c_1\theta_h) - 2\theta_h(1-\phi_h)^{\gamma}\mathbf{M}_1 \cdot \nabla \mathbf{u}_h]\varpi^j, \varpi^i), \tag{4.56}$$

$$F_i^{\mathbf{u}} = (\mathbf{v}_h, \varphi^i), \tag{4.57}$$

$$\begin{aligned} F_i^{\mathbf{v}} = &- \left((\mathbf{I} + \nabla \mathbf{u}_h)(1-\phi_h)^{\gamma}(\mathbf{M}_0 + \mathbf{M}_1\theta_h)(\theta_h - \theta_R), \nabla\varphi^i\right) \\ &- \left((1-\phi_h)^{\beta}(\mathsf{C}_0 + \mathsf{C}_1\theta_h)[\nabla \mathbf{u}_h], \nabla\varphi^i\right) + (\mathbf{b}_\kappa, \varphi^i) + (\mathbf{s}_p, \varphi^i)_A, \end{aligned} \tag{4.58}$$

$$\begin{aligned} F_i^{\theta} = &- \left((1-\phi_h)^{\alpha}(\mathbf{K}_0 + \mathbf{K}_1\theta_h)[\nabla\theta], \nabla\varpi^i\right) \\ &+ (\theta_h(1-\phi_h)^{\gamma}(\mathbf{M}_0 + \mathbf{M}_1(2\theta_h - \theta_R)) \cdot \nabla \mathbf{v}, \varpi^i) \\ &- \left(\gamma(1-\phi_h)^{\gamma-1}(\theta_R\mathbf{M}_0 + \mathbf{M}_1\theta_h^2) \cdot \dot{\phi}_h \nabla \mathbf{u}_h, \varpi^i\right) \\ &+ \left(\tau(1-\phi_h)^{\tau-1}(c_0(\theta_h - \theta_R) + c_1(\theta_h^2 - \theta_R^2)/2)\dot{\phi}_h, \varpi^i\right) \\ &+ (r_\kappa, \varpi^i) + (q_p, \varpi^i), \end{aligned} \tag{4.59}$$

$$\begin{aligned} F_i^{\phi} = &\left(\eta_C \left\langle -\tau(1-\phi_h)^{\tau-1}\left[c_0\left(\theta_h \log\frac{\theta_h}{\theta_R} - (\theta_h - \theta_R)\right) + c_1(\theta_h - \theta_R)^2/2\right]\right. \right. \\ &+ \gamma(1-\phi_h)^{\gamma-1}(\theta_h - \theta_R)(\mathbf{M}_0 + \mathbf{M}_1\theta_h) \cdot \nabla \mathbf{u}_h \\ &\left. \left. + \frac{\beta}{2}(1-\phi_h)^{\beta-1}(\mathsf{C}_0 + \mathsf{C}_1\theta_h)[\nabla \mathbf{u}_h] \cdot [\nabla \mathbf{u}_h] - G_{CR}\right\rangle, \varsigma^i\right). \end{aligned} \tag{4.60}$$

Comparing (4.54) to its linear counterpart in (4.13), one sees that no stiffness matrix has been defined in the non-linear case. This is because, as will be shown shortly, it is not beneficial to the calculations.

4.2.2 Time Integration

A similar operator-splitting style time-stepping scheme is used to integrate the ODE in (4.54). This is necessary because the nature of the thermoelastic-damage

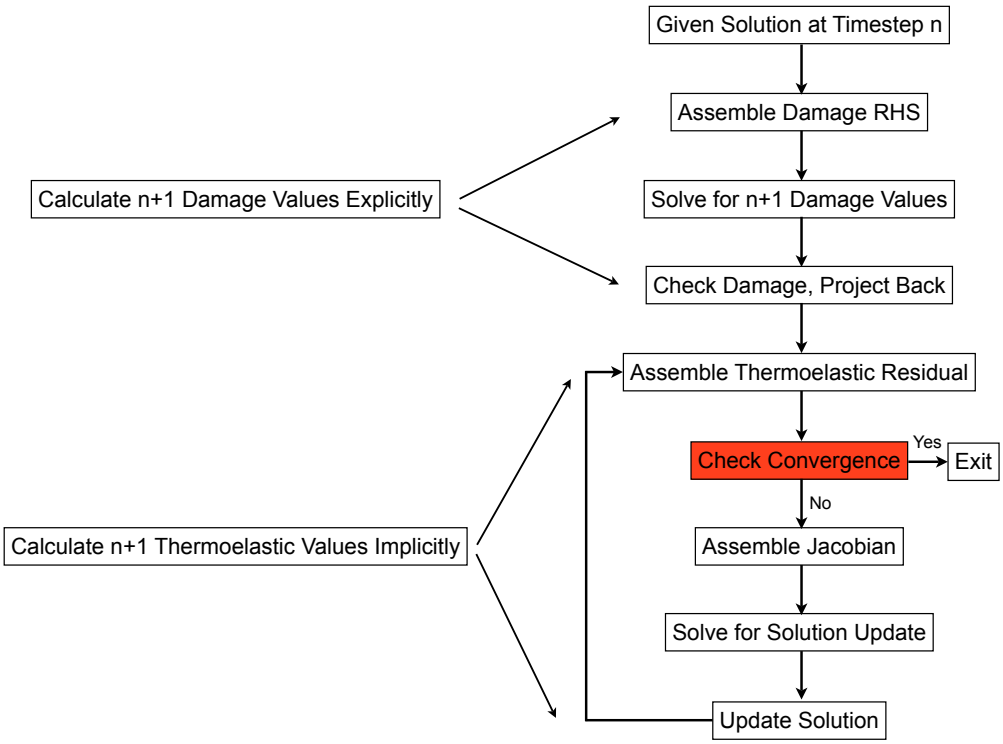

Figure 4.3. Flow-chart of the time-stepping algorithm for the theory which is non-linear when the damage is fixed. The red background of a box indicates a logical step in the algorithm.

equations of motion has not changed, and their is still a need for different numerical methods for the thermoelastic and damage parts of the system. Again, the values of the unknowns for the next time step are found sequentially, first for the damage variable and then for the thermoelastic quantities, rather than simultaneously. A flow chart of the algorithm for finding the solution at the next timestep is given in Figure 4.3. The algorithm is as follows, where n denotes the time step number. A flow-chart of the algorithm is also given in Figure 4.2.

1. Solve explicitly for $\Phi^{j,n+1} = \mathcal{F}_1(\Phi^{j,n}; U^{j,n}, V^{j,n}, \Theta^{j,n})$ using the first order accurate forward Euler method, where $\mathcal{F}_1$ is $\mathcal{F}$ when $\dot{u}$, $\dot{v}$, and $\dot{\theta}$ are set to zero. As in the fully-linear theory, a simple explicit algorithm is chosen to integrate the evolution equation for the damage variable.

The resulting linear system that is solved for the damage variable at the $n+1$ timestep is

$$M_{ij}^{\phi}\Phi^{j,n+1} = M_{ij}^{\phi}\Phi^{j,n} + \Delta t F_i^{\phi,n} \tag{4.61}$$

where

$$F_i^{\phi,n} = \left(\eta_C^n \left\langle G_h^n - G_{CR}^n \right\rangle, \varsigma^i\right) \tag{4.62}$$

and

$$\begin{aligned} G_h^n = -\tau(1-\phi_h^n)^{\tau-1}\left[c_0\left(\theta_h^n \log\frac{\theta_h^n}{\theta_R} - (\theta_h^n - \theta_R)\right) + c_1\left(\theta_h^n - \theta_R\right)^2/2\right] \\ + \gamma(1-\phi_h^n)^{\gamma-1}(\theta_h^n - \theta_R)(\mathbf{M}_0 + \mathbf{M}_1\theta_h^n)\cdot\nabla\mathbf{u}_h^n \\ + \frac{\beta}{2}(1-\phi_h^n)^{\beta-1}(\mathsf{C}_0 + \mathsf{C}_1\theta_h^n)[\nabla\mathbf{u}_h^n]\cdot[\nabla\mathbf{u}_h^n]. \end{aligned} \tag{4.63}$$

As with the linear theory, this part of the algorithm must also contain a check to ascertain whether the value of the damage has exceed the physically reasonable limit ($\phi = 1$), and employ a mechanism for projecting the values back into the proper range.

2. Solve implicitly for

$$\begin{aligned} &[U^{j,n+1}, V^{j,n+1}, \Theta^{j,n+1}] \\ &\qquad = \mathcal{F}_2\left(U^{j,n+1}, V^{j,n+1}, \Theta^{j,n+1}; U^{j,n}, V^{j,n}, \Theta^{j,n}, \Phi^{j,n+1}, \Phi^{j,n}\right), \end{aligned} \tag{4.64}$$

   where $\mathcal{F}_2$ is $\mathcal{F}$ when $\dot{\phi}$ is set to zero.

Note that, unlike the linear theory, even though we already have the values of $\Phi^{j,n+1}$, the resulting system is still nonlinear in the thermoelastic unknowns:

$$\begin{bmatrix} M & 0 & 0 \\ 0 & M^{\rho} & 0 \\ 0 & 0 & M^{c} \end{bmatrix} \begin{bmatrix} \dot{U}^j \\ \dot{V}^j \\ \dot{\Theta}^j \end{bmatrix} = \begin{bmatrix} F_i^{\mathbf{u}} \\ F_i^{\mathbf{v}} \\ F_i^{\theta} \end{bmatrix}. \tag{4.65}$$

Rewriting this system as

$$\mathcal{M}(\xi)\dot{\xi} = \mathcal{F}(\xi), \tag{4.66}$$

where $\mathcal{M}(\xi)$ is the solution-dependent mass matrix on the left-hand side of (4.65), $\mathcal{F}(\xi) = [F^{\mathbf{u}}, F^{\mathbf{v}}, F^{\theta}]^T$ is the solution-dependent right-hand side of (4.65), and applying the Crank-Nicholson scheme (again, see, e.g., Quarteroni et al., 2000) to (4.65) yields its fully-discrete form,

$$\mathcal{M}(\xi^{n+1})\xi^{n+1} = \mathcal{M}(\xi^{n+1})\xi^{n} + \frac{\Delta t}{2}\mathcal{F}(\xi^{n+1}) + \frac{\Delta t}{2}\mathcal{M}(\xi^{n+1})\mathcal{M}^{-1}(\xi^{n})\mathcal{F}(\xi^{n}). \tag{4.67}$$

Equation (4.69) contains a similar problematic term, namely $\mathcal{M}(\xi^{n+1})\mathcal{M}^{-1}(\xi^{n})$, as in its counterpart from the fully-linear theory (4.29). We can similarly simplify the matrix to

$$\mathcal{M}(\xi^{n+1})\mathcal{M}^{-1}(\xi^{n}) = \begin{bmatrix} I & 0 & 0 \\ 0 & I & 0 \\ 0 & 0 & M^{c}(\xi^{n+1})(M^{c}(\xi^{n}))^{-1} \end{bmatrix}, \tag{4.68}$$

but cannot further deduce that the term simplifies in the same manner as before. Therefore, we are left with a more general solution, where (4.69) becomes

$$\mathcal{M}(\xi^{n+1})\xi^{n+1} = \mathcal{M}(\xi^{n+1})\xi^{n} + \frac{\Delta t}{2}\mathcal{F}(\xi^{n+1}) + \frac{\Delta t}{2}\tilde{\mathcal{F}}(\xi^{n+1}, \xi^{n}), \tag{4.69}$$

such that

$$\tilde{\mathcal{F}}(\xi^{n+1}, \xi^{n}) = \begin{bmatrix} F^{\mathbf{u}}(\xi^{n}) \\ F^{\mathbf{v}}(\xi^{n}) \\ M^{c}(\xi^{n+1})\tilde{F}^{\theta}(\xi^{n}) \end{bmatrix} \quad \text{and} \quad \tilde{F}^{\theta}(\xi^{n}) = (M^{c})^{-1}(\xi^{n})F^{\theta}(\xi^{n}). \tag{4.70}$$

Equation (4.70) finalizes the assembly process for the overall system. First, $\tilde{F}^{\theta}(\xi^{n})$ is calculated by solving a small linear system, and then $\tilde{\mathcal{F}}(\xi^{n})$ is determined by the additional assembly of $F^{\mathbf{u}}(\xi^{n})$ and $F^{\mathbf{v}}(\xi^{n})$ and the matrix-vector multiplication of $M^{c}(\xi^{n+1})\tilde{F}^{\theta}(\xi^{n})$.

Clearly, the system defined in (4.69)-(4.70) is non-linear with respect to the solution at the $n+1$ timestep (ξ^{n+1}). We therefore define a residual,

$$\mathcal{R}(\xi_k^{n+1}, \xi^n) = \mathcal{M}(\xi_k^{n+1}) \left[\xi_k^{n+1} - \xi^n\right] - \frac{\Delta t}{2} \left[\mathcal{F}(\xi_k^{n+1}) + \tilde{\mathcal{F}}(\xi_k^{n+1}, \xi^n)\right], \tag{4.71}$$

where ξ_k^{n+1} is the solution to the thermoelastic part of the problem at k-th Newton iteration at the $n+1$ timestep. Assembly of this residual is straight forward, given the a solution at Newton iteration k, $\tilde{\mathcal{F}}(\xi_k^{n+1}, \xi^n)$ and $\mathcal{F}(\xi_k^{n+1})$ are calculated, followed by $\mathcal{M}(\xi_k^{n+1})$. The residual in (4.71) is then found through a series of matrix-vector multiplications and vector additions. As is customary in the linearization of problems, the residual is expanded about the solution at iteration k, and truncated after linear terms, and set to its ideal value of zero to obtain a linear system of the type

$$\mathcal{J}(\xi_k^{n+1}) \left[\delta\xi_k^{n+1}\right] = -\mathcal{R}(\xi_k^{n+1}, \xi^n). \tag{4.72}$$

Here $\mathcal{J}(\xi_k^{n+1})$ is the jacobian of the system, defined as

$$\mathcal{J}(\xi_k^{n+1}) = \frac{\partial \mathcal{R}(\xi_k^{n+1}, \xi^n)}{\partial \xi_k^{n+1}}. \tag{4.73}$$

Detailed expressions for the jacobian are given in Appendix B, and the timestep is chosen in the same manner as the linear model, in (4.34).

4.3 Solution Space Selection

A key point in the presentation of these numerical methods is the selection of approximate solution spaces, in conjunction with the proper finite elements, for the unknowns. The displacement, velocity, and temperature are treated in a standard manner throughout this formulation, therefore it is natural to simply select solution spaces that are rich enough to produce reasonable solutions. Shocks and other discontinuous phenomena intrinsic to the thermoelastic fields have not been explicitly considered in this model, and as such, we choose to use globally continuous polynomials. To determine if a given combination of elements (solution spaces) is appropriate for the thermoelastic fields, we choose a simplified set of

material parameters for the fully linear problem over the domain $\mathcal{B} = [0, 1]$,

$$\rho_\kappa = 1, \quad c = 1, \quad M = -1, \quad K = 1, \quad \alpha, \beta, \gamma, \tau = 0, \tag{4.74}$$

$$L = 1, \quad E = 1, \quad \theta_R = 10, \quad \eta_C = 0, \quad G_{CR} = 0, \tag{4.75}$$

which reduces the equations of motion for the fully-linear problem to

$$\dot{u} - v = 0, \tag{4.76}$$

$$\dot{v} - \text{Div}\left[\nabla u - (\theta - 10)\right] = b_\kappa, \tag{4.77}$$

$$\dot{\theta} - \text{Div}[\nabla\theta] - 10\nabla v = r_\kappa, \tag{4.78}$$

$$\dot{\phi} = 0. \tag{4.79}$$

Thus, the damage does not evolve, and we can study the choice of solution spaces for the thermoelastic fields independently of damage evolution. This is important as it will let us evaluate the performance of the integration of the thermoelasticty model.

4.3.1 Thermoelastic Verification

Verification is the practice of determining whether or not the proposed algorithm for finding an approximate numerical solution of a problem is indeed finding the correct solution. In other words, we follow a procedure to determine if the algorithm is solving the mathematical statement of the model correctly. This is disinctly different from the concept of validation, which seeks to determine if the physical model is correctly describing the natural world; one must be confident that the IBVP is being solved reliably before any comparison of the model to experiments or other analytical results can be made.

In the following procedure, a set of exact solutions are chosen and subsequently substituted into the simplified equations of motion (4.76-4.79). The resulting expressions are set equal to the body forces. These body forces, material properties, and boundary conditions are implemented in the code, and the resulting approximate solution is then compared to the exact solution. In this dissertation, the comparison is performed by finding the L^2, H^1, and L^∞ norms of the difference between the

exact and computed solutions. For a function $u(x)$, with a computed approximate solution $u_h(x)$, these norms are defined over the K-th cell as (see, e.g., Quarteroni et al., 2000)

$$\|u - u_h\|_{L^2(K)} = \left(\int_K |u(x) - u_h(x)| dx \right)^{1/2}, \tag{4.80}$$

$$\|u - u_h\|_{L^\infty(K)} = \max_{x \in K} |u(x) - u_h(x)|, \tag{4.81}$$

$$\|u - u_h\|_{H^1(K)} = \left(\|u - u_h\|^2_{L^2(K)} + \int_K |\nabla u(x) - \nabla u_h(x)|^2 dx \right)^{1/2}. \tag{4.82}$$

In summary, this procedure determines if the finite element method and Crank-Nicholson scheme are functioning correctly.

We select the following exact solutions,

$$u^*(x,t) = \sin(5\pi x)\,(\pi t - \sin \pi t)\,, \tag{4.83}$$

$$v^*(x,t) = \sin(5\pi x)\,(\pi - \pi \cos \pi t)\,, \tag{4.84}$$

$$\theta^*(x,t) = \cos(7\pi x)\,(\pi - \pi \sin \pi t) + 10, \tag{4.85}$$

$$\phi^*(x,t) = 0.001. \tag{4.86}$$

After substituting (4.83)-(4.86) into (4.76)-(4.79), one arrives at:

$$\begin{aligned} b_\kappa &= 25\pi^2(\pi t - \sin(\pi t)) \sin(5\pi x) + \pi^2 \sin(\pi t) \sin(5\pi x) \\ &\quad - 7\pi(\pi t - \sin(\pi t)) \sin(7\pi x), \end{aligned} \tag{4.87}$$

$$\begin{aligned} r_\kappa &= 50\pi(\pi - \pi \cos(\pi t)) \cos(5\pi x) + (\pi - \pi \cos(\pi t)) \cos(7\pi x) \\ &\quad + 49\pi^2 \cos(7\pi x)(\pi t - \sin(\pi t)), \end{aligned} \tag{4.88}$$

where the first two equations have been omitted because they are clearly automatically satisfied by the choice of exact solution in (4.83)-(4.86). Boundary conditions and initial conditions are the exact solutions evaluated at the boundaries and $t = 0$, respectively. From here, the general procedure is to solve the problem on successively uniformly refined grids, and observe the error at each calculation cycle.

Table 4.1 and Figure 4.4 show the errors and convergences rates when the

approximate solution space is defined as

$$\mathcal{V}_h = \mathcal{Q}^1(K) \times \mathcal{Q}^1(K) \times \mathcal{Q}^1(K) \times \mathcal{P}^0(K), \tag{4.89}$$

where $\mathcal{Q}^N(K)$ is the set of globally continuous polynomials resulting from the tensor product of N-degree polynomials over the the K^{th} cell, and $\mathcal{P}^0(K)$ is the set of piecewise constant polynomials over each cell. More specifically,

$$u_h, v_h, \theta_h \in \mathcal{Q}^1(K) \text{ and } \phi_h \in \mathcal{P}^0(K), \tag{4.90}$$

where in our one-dimensional example $\mathcal{Q}^1(K)$ is the space of linear polynomials. Both spaces correspond to the use of Lagrange finite elements. Because the damage is assumed to be uniform in the initial conditions, and is not evolving, the choice of solution space for the damage variable is irrelevant at this point. The convergence rates in Table 4.1 are calculated by comparing the error and mesh-size of successive refinement levels. From the theory of finite element methods, (see Brenner and Scott, 1994), the error (denoted by $\|e\|$) using polynomials of degree p is related to the mesh-size (denoted by h) as

$$\|e\| = ch^{p+a}, \tag{4.91}$$

where c is some constant and a is dependent on the nature of the selected norm. For the L^2 and L^∞ norms, one expects that the optimal error is obtained if $a = 1$, while for the H^1 norm, one expects that $a = 0$ (see, e.g., Brenner and Scott, 1994 and Antonietti and Heltai, 2007). Taking the logarithm of this relation yields

$$\log \|e\| = (p + a) \log ch, \tag{4.92}$$

where $p + a$ is the rate reported in Table 4.1. Following tradition, convergence charts usually have negative slopes, and thus the comparison of the error and $(1/h)$ in Figure 4.4. Clearly, for $\mathcal{Q}^1$ elements we are achieving an optimal convergence rate, which is encouraging considering that we have chosen very strong coupling between the equations, however, better absolute error can be obtained with higher order elements, thus we check these convergence cases as well.

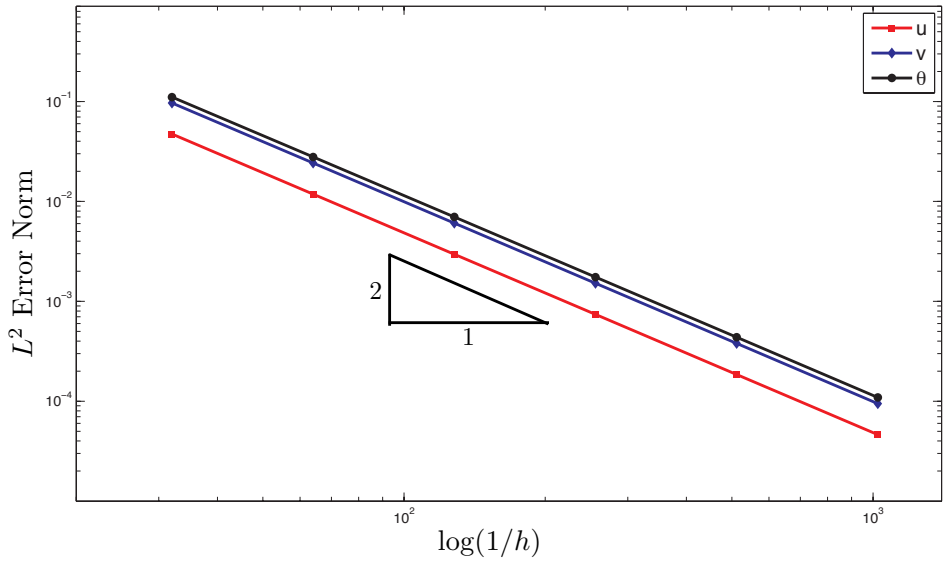

Figure 4.4. Log-Log plot of L^2-error as a function of cell length for $u_h, v_h, \theta_h \in \mathcal{Q}^1(K)$. The L^2 error is converging quadratically, as is expected with the use of linear elements.

Table 4.1. Table of errors and convergence rates for $u_h, v_h, \theta_h \in \mathcal{Q}^1(K)$.

# cells	# dofs	$\|u-u_h\|_{L^\infty}$		$\|u-u_h\|_{L^2}$		$\|u-u_h\|_{H^1}$	
32	131	8.872e-02	-	4.726e-02	-	4.926e+00	-
64	259	2.242e-02	1.98	1.184e-02	2.00	2.470e+00	1.00
128	515	5.609e-03	2.00	2.961e-03	2.00	1.236e+00	1.00
256	1027	1.403e-03	2.00	7.405e-04	2.00	6.180e-01	1.00
512	2051	3.507e-04	2.00	1.851e-04	2.00	3.090e-01	1.00
1024	4099	8.769e-05	2.00	4.628e-05	2.00	1.545e-01	1.00

# cells	# dofs	$\|v-v_h\|_{L^\infty}$		$\|v-v_h\|_{L^2}$		$\|v-v_h\|_{H^1}$	
32	131	1.795e-01	-	9.663e-02	-	9.852e+00	-
64	259	4.548e-02	1.98	2.423e-02	2.00	4.940e+00	1.00
128	515	1.141e-02	1.99	6.061e-03	2.00	2.472e+00	1.00
256	1027	2.856e-03	2.00	1.515e-03	2.00	1.236e+00	1.00
512	2051	7.142e-04	2.00	3.789e-04	2.00	6.181e-01	1.00
1024	4099	1.786e-04	2.00	9.472e-05	2.00	3.090e-01	1.00

# cells	# dofs	$\|\theta-\theta_h\|_{L^\infty}$		$\|\theta-\theta_h\|_{L^2}$		$\|\theta-\theta_h\|_{H^1}$	
32	131	2.217e-01	-	1.110e-01	-	9.649e+00	-
64	259	5.572e-02	1.99	2.791e-02	1.99	4.840e+00	1.00
128	515	1.400e-02	1.99	6.987e-03	2.00	2.422e+00	1.00
256	1027	3.502e-03	2.00	1.747e-03	2.00	1.211e+00	1.00
512	2051	8.751e-04	2.00	4.369e-04	2.00	6.057e-01	1.00
1024	4099	2.188e-04	2.00	1.092e-04	2.00	3.029e-01	1.00

Table 4.2 and Figure 4.5 show the results of using quadratic elements, and hence an approximate solution space of

$$\mathcal{V}_h = \mathcal{Q}^2(K) \times \mathcal{Q}^2(K) \times \mathcal{Q}^2(K) \times \mathcal{P}^0(K). \tag{4.93}$$

We note that the convergence rates for the L^∞ and L^2 norms are not optimal, as they are less than $p + a = 3$, but still very good, while the H^1 norm convergence rates are optimal. As explained in Antonietti and Heltai, 2007, certain choices of solution spaces, combined with non-symmetric system matrices, may result in less than optimal convergence. To investigate this, the coupling between the elastic and thermal equation is varied. As the coupling is decreased, the problem becomes more symmetric in the sense that the elastic and thermal equations 'see' less of each other, and hence their intrinsically symmetric nature dominates. Figure 4.6 shows the L^2 norm of the displacement error as the thermomechanical coupling is varied from zero (totally decoupled) to minus one (coupling on the same order as the other material properties). As expected, better convergence is obtained as the coupling is decreased; however, comparison of the absolute error values in Tables 4.2 and 4.2 demonstrate that the use of $\mathcal{Q}^2$ solution space is still preferable. Additionally, in practice, the thermomechanical coupling will be much smaller than the other material properties, so we are encouraged that good convergence properties will be present in later simulations.

It is important to remember that the convergence results here are also a function of the error accrued from the finite difference time-stepping. As described earlier, the timestep is chosen as a function of the mesh size*, and we can be comfortable with our choice based on the reasonable convergence rates just demonstrated. It is clear that the choices of

$$\mathcal{V}_h = \mathcal{Q}^2(K) \times \mathcal{Q}^2(K) \times \mathcal{Q}^2(K) \times \mathcal{P}^0(K) \tag{4.94}$$

as an approximate solution space, and the Crank-Nicholson finite difference timestepping with CFL based timestep, are adequate for the linear thermoelastic problem.

For the high-temperature, nonlinear thermoelastic theory, we simply want to

*A fixed CFL based time-step may not strictly be necessary, as adaptive time-stepping schemes could be used.

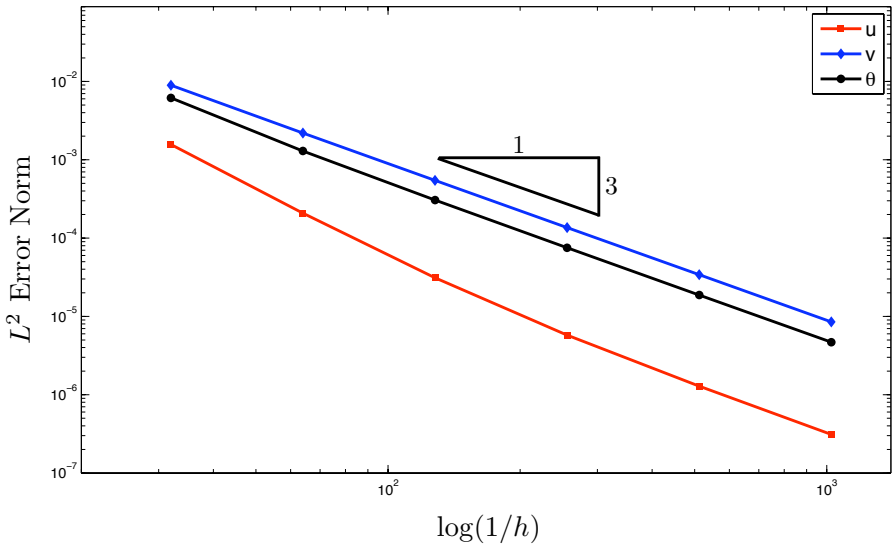

Figure 4.5. Log-Log plot of L^2-error as a function of cell length for $u_h, v_h, \theta_h \in \mathcal{Q}^2(K)$, when damage is fixed and uniform.

Table 4.2. Table of errors and convergence rates for $u_h, v_h, \theta_h \in \mathcal{Q}^2(K)$.

# cells	# dofs	$\|u-u_h\|_{L^\infty}$		$\|u-u_h\|_{L^2}$		$\|u-u_h\|_{H^1}$	
32	227	3.106e-03	-	1.565e-03	-	3.123e-01	-
64	451	4.247e-04	2.87	2.078e-04	2.91	7.828e-02	2.00
128	899	6.461e-05	2.72	3.108e-05	2.74	1.958e-02	2.00
256	1795	1.194e-05	2.44	5.767e-06	2.43	4.896e-03	2.00
512	3587	2.636e-06	2.18	1.286e-06	2.16	1.224e-03	2.00
1024	7171	6.347e-07	2.05	3.111e-07	2.05	3.060e-04	2.00

# cells	# dofs	$\|v-v_h\|_{L^\infty}$		$\|v-v_h\|_{L^2}$		$\|v-v_h\|_{H^1}$	
32	227	1.683e-02	-	8.950e-03	-	6.363e-01	-
64	451	4.075e-03	2.05	2.192e-03	2.03	1.594e-01	2.00
128	899	1.011e-03	2.01	5.456e-04	2.01	3.988e-02	2.00
256	1795	2.521e-04	2.00	1.363e-04	2.00	9.971e-03	2.00
512	3587	6.301e-05	2.00	3.405e-05	2.00	2.493e-03	2.00
1024	7171	1.584e-05	1.99	8.513e-06	2.00	6.910e-04	1.85

# cells	# dofs	$\|\theta-\theta_h\|_{L^\infty}$		$\|\theta-\theta_h\|_{L^2}$		$\|\theta-\theta_h\|_{H^1}$	
32	227	1.516e-02	-	6.169e-03	-	8.570e-01	-
64	451	2.878e-03	2.40	1.292e-03	2.26	2.153e-01	1.99
128	899	6.011e-04	2.26	3.055e-04	2.08	5.389e-02	2.00
256	1795	1.358e-04	2.15	7.526e-05	2.02	1.348e-02	2.00
512	3587	3.215e-05	2.08	1.874e-05	2.01	3.369e-03	2.00
1024	7171	7.819e-06	2.04	4.681e-06	2.00	8.424e-04	2.00

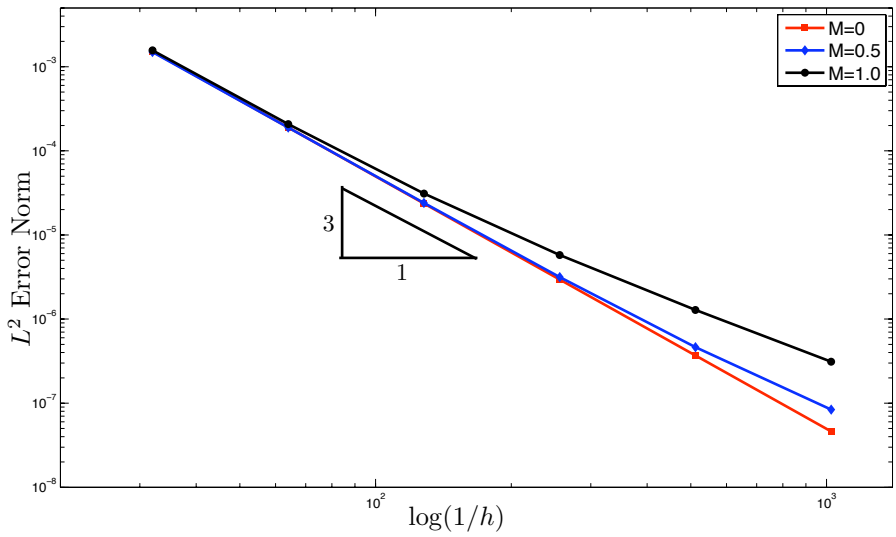

Figure 4.6. Log-Log plot of L^2-error of the displacement as a function of cell length for $u_h, v_h, \theta_h \in \mathcal{Q}^2(K)$, with varying values of M. We see that increasing the strength of the thermomechanical coupling decreases the convergence of the displacement field. This is most likely due to an increase in numerical diffusion (damping) associated with the dissipative nature of the thermoelastic equations.

verify that this element selection is also valid. For this model, we need values for the material properties at two different temperatures, as described in Section 3.5.2. Choosing the following values, where $\theta_2 = 110$ and $\theta_1 = 10$,

$$c|_{\theta_2} = 2 \quad c|_{\theta_1} = 1, \quad K|_{\theta_2} = 2 \quad K|_{\theta_1} = 1, \tag{4.95}$$

$$E|_{\theta_2} = 2 \quad E|_{\theta_1} = 1 \quad M|_{\theta_2} = -0.02 \quad M|_{\theta_1} = -0.01, \tag{4.96}$$

$$\eta_C|_{\theta_2} = 0 \quad \eta_C|_{\theta_1} = 0, \quad G_{CR}|_{\theta_2} = 0 \quad G_{CR}|_{\theta_1} = 0 \tag{4.97}$$

yields the values necessary for the equations of motion

$$\rho_\kappa = 1, \quad \theta_R = 10, \quad G_{CR} = 0, \quad \eta_C = 0, \quad L = 1, \tag{4.98}$$

$$c_0 = 0.9, \quad c_1 = 0.01, \quad M_0 = -0.009, \quad M_1 = -0.0001, \quad \alpha, \beta = 0 \tag{4.99}$$

$$E_0 = 0.9, \quad E_1 = 0.01, \quad K_0 = 0.9, \quad K_1 = 0.01, \quad \gamma, \tau = 0. \tag{4.100}$$

The temperature dependence of the material properties given in (4.95)–(4.95) can be considered to be quite strong. The material parameters for the bulk graphite used in the rocket nozzle MURI project fluctuate only at most by 100% over a two

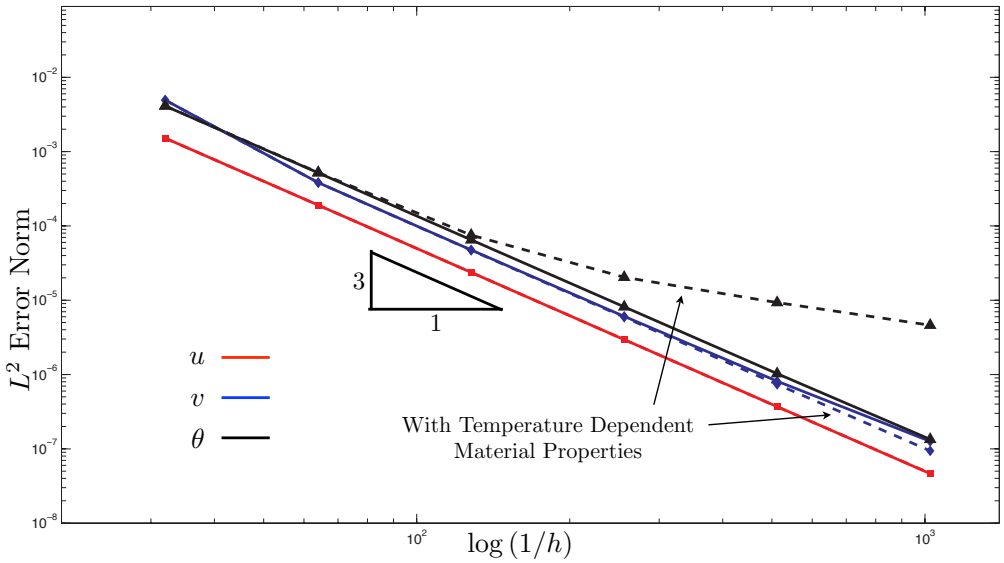

Figure 4.7. Log-Log plot of the L^2-error generated by the non-linear model as a function of cell length for $u_h, v_h, \theta_h \in \mathcal{Q}^2(K)$. The error is shown for both the cases when the material properties are not a function of temperature (solid lines), and when they are strongly a function of temperature (dashed lines). The temperature loses at least an order of convergence when the material properties are strongly dependent on the temperature; however, this is not surprising given that the temperature field is the only field which was not linearized in the derivation of the high temperature problem.

thousand degree change in temperature. Thus, the fact that here the change in the material properties is assumed to be the same, but instead over only one hundred degrees, will test the performance of the algorithm in Figrure 4.3 under a worst case scenario.

Following the same procedure used for the linear problem, we substitute (4.44)–(4.47) into the equations of motions, and subsequently implement the resulting forcing functions (not shown) into the code, along with the exact solutions as the boundary values and initial conditions, to obtain an approximate solution. The numerical solution is compared to the exact solution, and the errors are given in Figure 4.7.

4.3.2 Damage Variable Solution Space

The proper approximate solution spaces for the damage variable are investigated in this section. While verifying that the thermoelastic part of the problem is being

solved corrected, we used the approximate solution spaces

$$\mathcal{V}_h = \mathcal{Q}^1(K) \times \mathcal{Q}^1(K) \times \mathcal{Q}^1(K) \times \mathcal{P}^0(K) \tag{4.101}$$

and

$$\mathcal{V}_h = \mathcal{Q}^2(K) \times \mathcal{Q}^2(K) \times \mathcal{Q}^2(K) \times \mathcal{P}^0(K), \tag{4.102}$$

where the approximate solution for the damage was constant and uniform, and thus perfectly resolved in the piece-wise constant space of $\mathcal{P}^0(K)$. We now seek to explore the ability of various solution spaces when the more interesting situation of non-uniform evolving damage is present. The material properties for this problem are still idealized, similarly to those in (4.74)-(4.75) for the fully-linear problem, and are given below in (4.103)-(4.104).

$$\rho_\kappa = 1, \quad c = 1, \quad M = -0.01, \quad K = 1, \quad \alpha, \gamma, \tau = 2, \quad \beta = 1 \tag{4.103}$$

$$L = 1, \quad E = 1, \quad \theta_R = 10, \quad \eta_C = 10, \quad G_{CR} = 0, \tag{4.104}$$

The boundary conditions are different than those in the thermoelastic verification, and consist of

$$u(0,t) = 0, \qquad v(0,t) = 0, \qquad q_p(0,t) = q_p(1,t) = 0, \tag{4.105}$$

and the applied force

$$s_\kappa(1,t) = \begin{cases} \frac{1}{2} s_0 \left[1 - \cos\left(2\pi t / t_0\right)\right] & t < t_0 \\ 0 & \text{otherwise} \end{cases}, \tag{4.106}$$

where $s_0 = 1$ and $t_0 = 0.1$. The boundary conditions correspond to a bar which is fixed on the left-hand side ($X = 0$), and subjected to a force applied on the right-hand side ($X = 1$) for a relatively short time interval, all the while being perfectly insulated. The initial conditions are

$$u(X,0) = 0, \qquad v(X,0) = 0, \qquad \theta(X,0) = \theta_R, \qquad \phi(X,0) = 0.0001. \tag{4.107}$$

Table 4.3. Summary of damage approximate solution spaces and their level of functionality with approximate solution spaces for the thermoelastic problem. It is clear that some sort of stability condition is present.

	Thermoelastic Solution Space		
	$\mathcal{Q}^1(K) \times \mathcal{Q}^1(K) \times \mathcal{Q}^1(K)$	$\mathcal{Q}^2(K) \times \mathcal{Q}^2(K) \times \mathcal{Q}^2(K)$	$\mathcal{Q}^3(K) \times \mathcal{Q}^3(K) \times \mathcal{Q}^3(K)$
$\mathcal{Q}^2(K)$	Not Functional	Not Functional	Unstable
$\mathcal{Q}^1(K)$	Not Functional	Functional	Functional
$\mathcal{P}^0(K)$	Stable	Stable	Stable
$\mathcal{P}^1(K)$	Not Functional	Functional	Functional
$\mathcal{P}^2(K)$	Not Functional	Not Functional	Unstable

Thus, in this simulation we see a wave travel from right to left across the bar, and reflect back to the right-hand side. Because $G_{CR} = 0$, we expect the damage variable to increase all across the bar as the wave travels along it, as there is no threshold for the damage to overcome before it starts to evolve. This particular simulation is run for the amount of time necessary for the wave to traverse the bar and back.

Table 4.3 lists the viability of using different combinations of thermoelastic solution spaces (columns) with damage variable solution spaces (rows). An entry of 'Not Functional' means that the solution space is so inappropriate that the simulation fails, usually by means of the linear solver* not being able to invert the system matrix. If the situation were such that damage values were very large, we may have cause to suspect some other reason for the failure, but as shown in Figure 4.8, the values of the damage variable are not exceeding even one-third of the maximum value of ϕ. Such combinations, in the context of the algorithm proposed here, are not viable for our purposes.

A combination of solution spaces with an entry of 'Functional' means that the simulation is able to proceed, and the results are at least mathematically reasonable. As shown in Figure 4.8 (right), when $\mathcal{Q}^2$-elements are used as a solution space for the thermoelastic fields, the use of solution spaces of $\mathcal{P}^1$ and $\mathcal{Q}^1$, which are piece-wise linear discontinuous and continuous polynomials respectively, can lead to non-physical decreases in damage locally. While mathematically this is not a problem, especially from the approximation theory point of view (see, e.g., Deutsch,

*In this case, a direct linear solver is used, specifically UMFPACK (see Davis, 2004b and Davis, 2004a), because of its advanced capabilities for inverting problematic matrices.

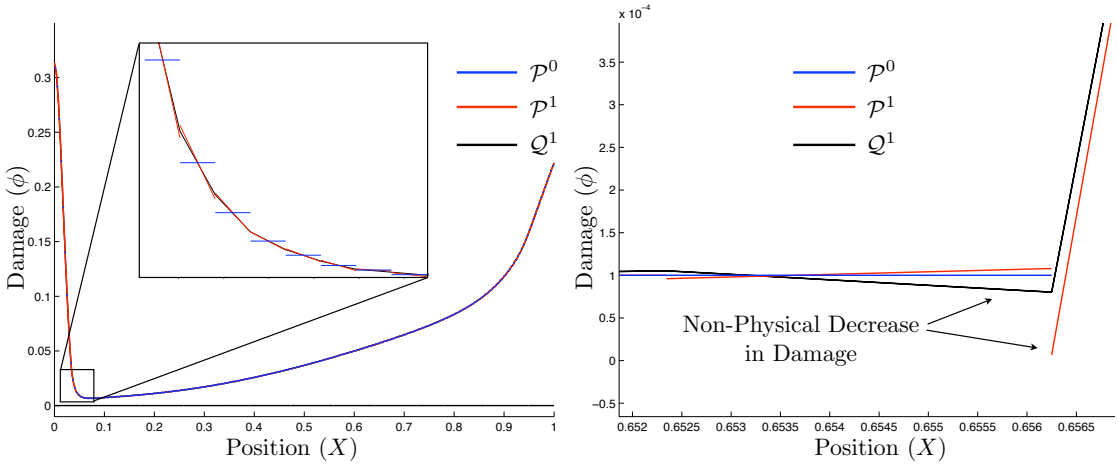

Figure 4.8. Comparison of solutions for the damage variable in multiple approximate solution spaces when the thermoelastic solution space is comprised totally of $\mathcal{Q}^2$-elements. The entire domain is given (left), showing that in general, the solution is reasonably similar; however, a zoom-in (right) reveals that the use of $\mathcal{Q}^1$ and $\mathcal{P}^1$ elements for the damage results in oscillations of the solution. All simulations are performed with 256 cells in the triangulation.

2001), it is physically of significant concern for us. From the physical model, we know that $\dot{\phi} < 0$ corresponds to the healing of cracks, which have have explicitly assumed does not occur. Therefore, even though these solution spaces are functional and mathematically reasonable, we hesitate to use them because they may lead to physical inconsistencies.

Finally, some combinations of spaces are labeled either 'Stable' or 'Unstable' in Table 4.3. With all combinations of solutions spaces for the thermoelastic fields, the use of piecewise constant discontinuous elements ($\mathcal{P}^0$) is non-oscillatory, and produces solutions consistent with the physical nature of the system, as seen in Figure 4.8 (right). The use of $\mathcal{Q}^3$-elements for the thermoelastic fields and $\mathcal{Q}^2$ or $\mathcal{P}^2$-elements for the damage solution space results in solutions that are highly oscillatory, as seen in Figure 4.9, and hence the label 'Unstable'. This behavior is not reasonable, and rules out the use of quadratic-elements for the damage variable approximate solution space.

In conclusion, the information in Table 4.3 clearly indicates that the piecewise constant, by cell, discontinuous approximate solution space is favored for subsequent simulations. Physically, this may be reconcilable with the method in which damage parameters are defined, namely homogenization over a representative

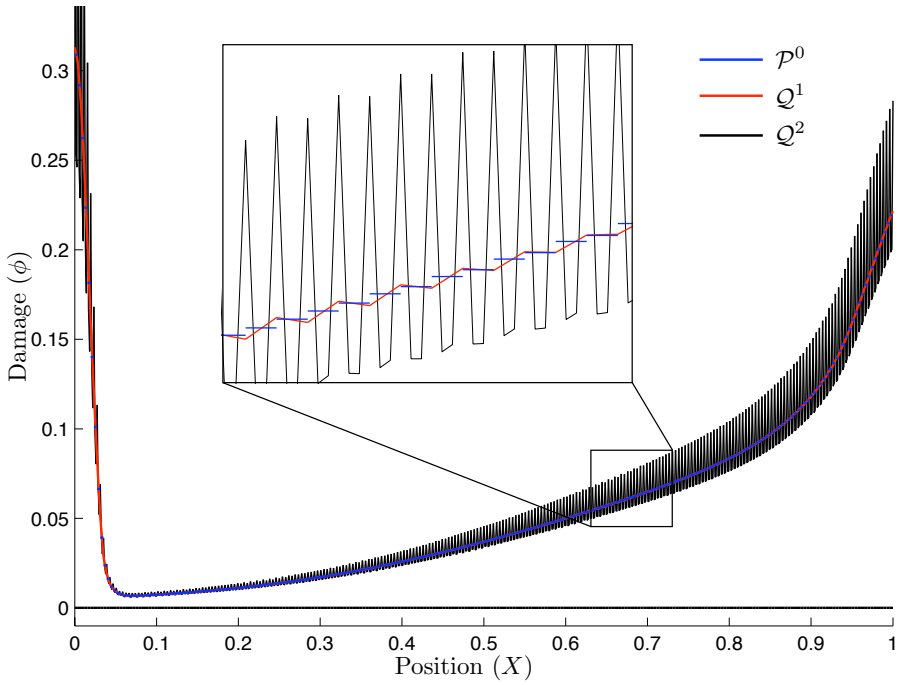

Figure 4.9. Even when functional, using $\mathcal{Q}^2$-elements for the damage variable leads to an unstable solution in this case. All simulations are performed with 256 cells in the triangulation, and a thermoelastic solution space of all $\mathcal{Q}^3$-elements.

volume element. This is the first known attempt to explore in any manner the proper solution spaces for the damage variable, and is a significant departure from the usual method of keeping track of the damage variable at the quadrature point in, say, a tabular format.

There appears to be an intrinsic stability condition in the problem as well. From the entries in Table 4.3, one can deduce that to at least have a functional formulation, although possibly unstable, the dimension of the damage approximate solution space must be at least one less than the approximate solution spaces for the thermoelastic unknowns. This is like the well known inf-sup, or Babuška-Brezzi, condition in mixed finite element methods (see, e.g., Babuška, 1971 and Brezzi, 1974); however, there is no proof at the current time to support a claim that it *is* actually this effect. The results presented in this section should be regarded as purely empirical, as additional analysis is necessary before more claims can be made.

4.4 Summary and Computer Implementation

The above numerical algorithms have been implemented into a custom C++ code. The entire program relies heavily on the deal.ii finite element library (see Bangerth et al., 2006) for most of the low level functions associated with implementing the finite element method. A major benefit of using such a library is the ability to write an extensible, dimension independent code. Element types are selected at run time via a text input file, and boundary conditions that are functions of both time and space are implemented into an input file as well. Additionally, the adaptive meshing algorithms presented in Chapter 6 rely heavily on the implementation of an adaptive triangulation in the deal.ii library.

Parallelization is supported natively in the deal.ii library through the use of the PETSc parallel computing libraries distributed by Argonne National Laboratory (ANL). These libraries are highly optimized, and are recognized by many for being reliable and efficient. The largest single benefit from implementing parallel methods is the distributed assembly and storage of the system matrix. Additional benefits include distributed linear solvers and data file writing, but it must be emphasized again that the run-time dominant part of the code is matrix assembly. When adaptive meshing algorithms are introduced to dynamic, semi-discrete formulations, most expectations of reasonable speedup are quickly disqualified.

As a final remark, we note that the decision to use $\mathcal{P}^0$ elements to approximate the damage field is satisfactory in this instance, but may not be under all situations. For example, all of the convergence analysis presented in this chapter is the result of one-dimensional models. We make no claim that Table 4.3 is definitive or complete, in the sense that there may be other dimensions to the table, such as the spatial dimension of the problem. Perhaps in higher dimension problems the use of higher order discontinuous elements for the damage field is possible and even preferable. Due to these possibilities, the author feels that the study of solution spaces for the damage variable is a step in the right direction, and hopes it will serve as a starting point for future discussions.

Chapter 5

Numerical Experiments

During the derivation of both the linear and non-linear models, various parameters and material properties have been introduced. Some of these quantities are familiar, such as the elastic moduli (C), specific heat (c), thermomechanical coupling ($\mathbf{M}$), and thermal conductivity ($\mathbf{K}$). Others are specific to the class of models and constitutive relations we have chosen, such as the crack propagation parameter η_C and critical energy release rate G_{CR}, while yet others are intrinsic to this model, even if only to offer a generalization from the previous work of other authors. The new parameters are the exponents in the constitutive relations, α, β, γ, and τ.

The purpose of this chapter is to begin to understand how the material parameters affect the motion of a thermoelastic material with damage. The dependence of the model on the material parameters, especially those intrinsic to this dissertation, is investigated. The resulting changes in behavior induced by the exponents α, β, γ, and τ will provide insight into which quantities are most sensitive to the damage evolution, and in turn reveal which quantities warrant further study of their dependence on damage.

In this chapter, numerical complications are removed by reducing the domain of the problem to one dimension (as has already been considered in Chapter 4 for convergence studies). In this manner, the concerns with adaptive meshing and varying mesh size can be isolated and ignored for the sake of clarifying the study of the physics at hand. Because of the reduced size of the problem, a uniform mesh with a sufficiently small element size can be used from the start of the simulation. Not only does this mathematically reduce the complexity of the algorithm, it

further reduces the computational overhead and programming complexity. This simplification allows us to focus on the physical aspects of the model.

The fully linear model is used to determine the effect that the new parameters, namely the exponents α, β, γ, and τ, in the constitutive equations have on the resulting evolution of the system. A set of values for the exponents is chosen, and then used in subsequent simulations. During the investigation of what values are proper for the exponents, the material properties relevant to the damage evolution, i.e., η_C and G_{CR}, are chosen such that they are within a range that produces routine motions, rather than ones where other phenomena may dominate the behavior, and hence blur the affect on the model of the values of the exponents. For example, if η_C is very large, the damage will grow very quickly, and the difference in damage evolution caused by different values of the exponents may be indistinguishable. Once a set of values for the exponents is chosen, a limited study of the effect the damage evolution due to the temperature dependence of the material properties (η_C and G_{CR}) is examined. In all of the simulations presented, the thermoelastic material parameters used are are those of brittle bulk graphite, as detailed in Appendix A and summarized in Table 5.1.

Table 5.1. Representative material properties for high density graphite at room and elevated temperature.

Quantity	Symbol	At 300 K	At 2588.15 K
Mass Density	ρ_κ	$1.87 \times 10^3\,\mathrm{kg/m^3}$	$1.87 \times 10^3\,\mathrm{kg/m^3}$
Elastic Modulus	E	$1.16 \times 10^{10}\,\mathrm{Pa}$	$2.23 \times 10^{10}\,\mathrm{Pa}$
Bulk Modulus	k_{bulk}	$9.65 \times 10^9\,\mathrm{Pa}$	$1.86 \times 10^{10}\,\mathrm{Pa}$
Lamé Parameter	λ	$6.68 \times 10^9\,\mathrm{Pa}$	$1.29 \times 10^{10}\,\mathrm{Pa}$
Lamé Parameter	μ	$4.45 \times 10^9\,\mathrm{Pa}$	$8.59 \times 10^9\,\mathrm{Pa}$
Thermal Conductivity	k_{th}	$1.74 \times 10^2\,\mathrm{W/(m{\cdot}K)}$	$1.53 \times 10^2\,\mathrm{W/(m{\cdot}K)}$
Specific Heat	c	$1.31 \times 10^6\,\mathrm{J/(m^3{\cdot}K)}$	$1.49 \times 10^6\,\mathrm{J/(m^3{\cdot}K)}$
Thermomechanical Coupling	β_{TM}	$3.13 \times 10^4\,\mathrm{N/(m^2{\cdot}K)}$	$1.81 \times 10^5\,\mathrm{N/(m^2{\cdot}K)}$

5.1 1D IBVP Description

The following numerical experiments are based of the problem of a one-dimensional uniform bar subjected to an applied force at one end, and clamped on the other, as show in Figure 5.1. More specifically, consider the domain $\mathcal{B}$ to be the interval $[0, L]$, with mechanical boundary conditions

$$u(0,t) = 0, \qquad v(0,t) = 0, \qquad \sigma(L,t) = F(t), \tag{5.1}$$

where

$$\sigma = E(1-\phi)^{\beta} u' + M(1-\phi)^{\gamma}(\theta - \theta_R) \tag{5.2}$$

is the uniaxial stress, E is the scalar elastic modulus (for zero damage), M is the thermomechanical coupling (for zero damage), and $()'$ represents the derivative with respect to the spatial coordinate. Additionally, we assume that the bar is perfectly insulated, i.e.,

$$q(0,t) = q(L,t) = 0, \text{ where } q = K(1-\phi)^{\alpha}\theta'. \tag{5.3}$$

Here K is the scalar thermal conductivity usually associated with one-dimensional isotropic models. For completeness, the equations of motion in one dimension for the fully linearized model are

$$\dot{u} - v = 0, \tag{5.4}$$

$$\rho_\kappa \dot{v} - (E(1-\phi)^{\beta} u' + M(1-\phi)^{\gamma}(\theta - \theta_R))' = b_\kappa, \tag{5.5}$$

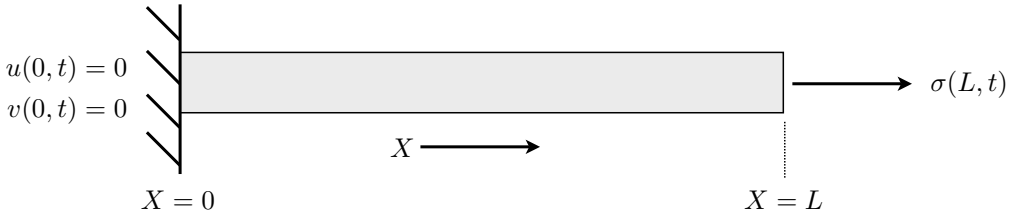

Figure 5.1. The geometry and mechanical boundary conditions of the one dimensional bar used in the numerical experiments presented in this chapter.

$$c(1-\phi)^{\tau}\dot{\theta} + \left[2\theta_R\gamma(1-\phi)^{\gamma-1}Mu' - \tau c(1-\phi)^{\tau-1}(\theta-\theta_R)\right]\dot{\phi} \\ -(K(1-\phi)^{\alpha}\theta')' - \theta_R(1-\phi)^{\gamma}Mv' = r_{\kappa}, \tag{5.6}$$

$$\dot{\phi} - \eta_C\left\langle \frac{\beta}{2}(1-\phi)^{\beta-1}E(u')^2 + \gamma(1-\phi)^{\gamma-1}M(\theta-\theta_R)u' \right. \\ \left. -\frac{\tau c}{2\theta_R}(1-\phi)^{\tau-1}(\theta-\theta_R)^2 - G_{CR}\right\rangle = 0. \tag{5.7}$$

The exact expressions for the critical energy release rate G_{CR} and the crack propagation parameter η_C will be defined when needed, but for the initial parameter study they are assumed to be constant, and have the values $\eta_C = 1 \times 10^{-2}\,\mathrm{m^3/J{\cdot}s}$ and $G_{CR} = 3 \times 10^5\,\mathrm{J/m^3}$. The thermoelastic material properties are those at room temperature as given in Table 5.1. Initially, the bar is assumed to be at rest and at the reference temperature, and as such the initial conditions are

$$u(X,0) = 0 \quad v(X,0) = 0 \quad \theta(X,0) = \theta_R \quad \phi(X,0) = \phi_0, \tag{5.8}$$

where $\theta_R = 300\,\mathrm{K}$ and $\phi_0 = 0.0001$. We define the stress applied to the bar (see Figure 5.1) to be

$$\sigma(L,t) = \begin{cases} \frac{1}{2}s_0\left[1-\cos\left(2\pi t/t_0\right)\right] & t < t_0 \\ 0 & \text{otherwise} \end{cases}, \tag{5.9}$$

where $s_0 = 50\,\mathrm{MPa}$ and $t_0 = 20\,\mu\mathrm{s}$. The loading described by (5.9) corresponds to a tensile force applied at the right end of the bar.

In Chapter 4, convergence was carefully checked for the thermoelastic fields. Now, we check convergence of the damage evolution by running the same simulation on successive refined meshes, and compare the damage temperature fields at a fixed time into the simulation. This measure of convergence is not as strong as the use of exact solutions detailed in Chapter 4, but is often used to gauge the performance of formulations to which exact solutions would be difficult, if not impossible to devise (see, e.g., Simo and Hughes, 1998). As shown in Figure 5.2, the temperature and damage field vary only slightly with the use of 128, 256, or 512 cells (elements). Thus, we can be reasonably satisfied that using 256 cells provides an acceptable solution in the subsequent simulations.

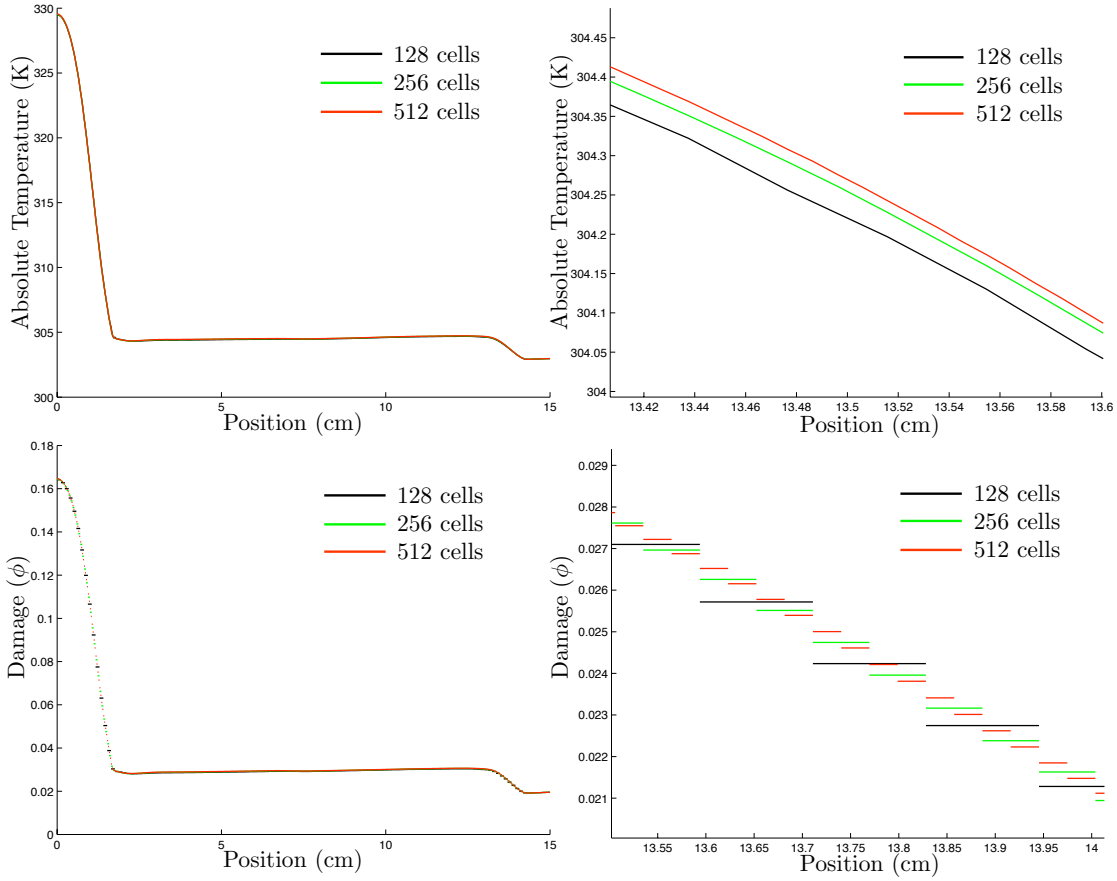

Figure 5.2. The temperature and damage fields at $t = 352.8\,\mu$s. For these simulations, $\alpha = \beta = \gamma = 2$, $\tau = 0.5$, $\eta_c = 1 \times 10^{-2}\,\mathrm{m}^3/\mathrm{J}{\cdot}\mathrm{s}$ and $G_{CR} = 2 \times 10^5\,\mathrm{J}/\mathrm{m}^3$. The images on the left are the temperature (top) and damage (bottom) over the entire bar at the given time, while the images on the right are zoom-in images of the temperature (top) and damage (bottom) of the corresponding plot on the left. It is clear that the solution is differing only slightly on refined meshes.

5.2 Exponent Parameter Study

Recalling the previous discussion in Chapter 3, the constitutive equations for the fully-linear case, in one dimension, have the form

$$K(\phi) = (1-\phi)^{\alpha} K, \qquad E(\phi) = (1-\phi)^{\beta} E, \tag{5.10}$$

$$M(\phi) = (1-\phi)^{\gamma} M, \qquad c(\phi) = (1-\phi)^{\tau} c. \tag{5.11}$$

Consequently, the free energy and the energy release can be written as

$$\psi = \frac{1}{2}(1-\phi)^{\beta}E(u')^2 + (\theta-\theta_R)(1-\phi)^{\gamma}Mu' - \frac{c}{2\theta_R}(1-\phi)^{\tau}(\theta-\theta_R), \tag{5.12}$$

$$G = \frac{\beta E}{2}(1-\phi)^{\beta-1}(u')^2 + \gamma(1-\phi)^{\gamma-1}M(\theta-\theta_R)u' - \frac{\tau c(1-\phi)^{\tau-1}}{2\theta_R}(\theta-\theta_R)^2. \tag{5.13}$$

Examining (5.10)-(5.13), we observe that there are critical values of each of the exponents α, β, γ, and τ at zero and one. Setting any of these exponents equal to zero effectively decouples some part of the physics from the problem. In this manner, we can 'turn off' part of the problem to isolate the effects of another. For example, if $\gamma = 0$, then the thermomechanical coupling will not be dependent on the damage. Additionally, setting any of these values to unity preserves the coupling of the damage into the thermoelastic nature of the problem, but creates an energy release rate that is devoid of dependence on the damage with regards to the term of that exponent. If all of the exponents are equal to one, and if the crack propagation parameter and critical energy release rate are constants, then the damage evolution itself ceases to be a function of the damage.

A natural question to ask at this point is whether the exponents should be positive or negative. The effect is clear, and is shown in Figure 5.3. If we desire a constitutive relation where the constitutive property degrades as damage increases, as in the case of the elastic moduli, then we need a positive value for the exponent. Otherwise, we will have a material property that seems to increase as damage increases. Additionally, if the exponent is negative, as $\phi \to 1$, the quantity $(1-\phi)^a \to \infty$.

One fundamental assumption throughout the history of damage mechanics is that as damage increases at a point, the body becomes less able to withstand stress at that point, and via a decrease in the elastic modulus undergoes a larger strain to maintain equilibrium. Following this concept, we can conclude that the exponent β should be positive. Recalling that the stress is

$$\sigma = E(1-\phi)^{\beta}u' + M(1-\phi)^{\gamma}(\theta-\theta_R), \tag{5.14}$$

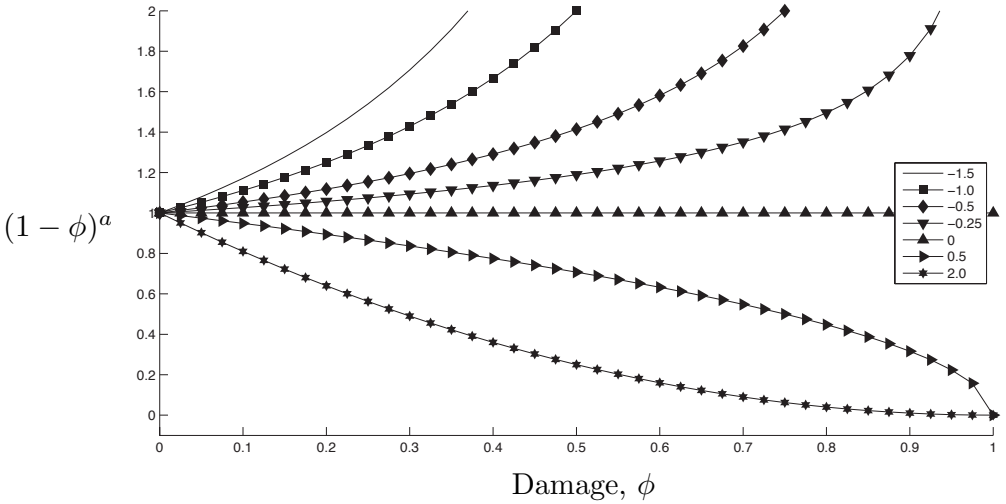

Figure 5.3. The effect of the exponent on the quantity $(1-\phi)^a$, where the values of a are given in the plot legend. Positive values yield a constitutive relation that diminishes the material property as damage increases, while negative values yield the opposite; the material property appears larger over time. The case when the exponent is zero is plotted for reference.

we now investigate the domain of the exponent γ. If we consider that each term in (5.14) should independently maintain its contribution to the total stress as damage evolves, then, as damage increases, we have two options for the second term. Either $\gamma > 0$, and we would expect to see a temperature increase, or, $\gamma < 0$, and we would expect to see a corresponding temperature decrease. As we know from the empirical observations of others (see, e.g., Ravi-Chandar et al., 2000), when microcracking is evolving, we often expect to see an increase in the local temperature due to the dissipation of energy, and as such we take $\gamma > 0$ for the rest of this document. At this point, we have restricted the domain of the exponents β and γ, such that

$$\beta, \gamma \geq 0. \tag{5.15}$$

In summary, the above definition physically corresponds to a material that, given a specified stress σ, will see the strain and temperature increase at a point where damage is evolving. Note that no claim is being made that these exponents should have any precise value for a specific material. We are simply positing that if the assumptions in (5.15) are made, we then have consequently assumed a certain

general physical behavior. There are four distinct cases for these values:

$$\beta, \gamma = 0 \quad \beta, \gamma \in (0,1) \quad \beta, \gamma = 1 \quad \beta, \gamma \in (1, \infty). \tag{5.16}$$

In selecting values for the upcoming parameter studies, we will use these ranges as a starting point. For example, it is clearly important to observe the behavior of the system at the critical points of zero and unity, as well as the range between them and beyond them. How far beyond the value of unity is an interesting question, which is answered as necessary by observation and common sense.

The exponent that affects the thermal conductivity, α, is also assumed to be non-negative

$$\alpha \geq 0. \tag{5.17}$$

Physically, this corresponds to a material that has a reduced capacity to conduct heat as microcracking increases. Ultimately, when a point on the body is fully damaged, that is, there is a macrocrack present, one would expect no heat to be conducted through the point (if the crack is open and not filled with a gas or fluid), so this appears to physically reasonable. With this in mind, it should be remarked that any value of α will satisfy (3.41), and hence not violate the thermodynamic admissibility of the model.

The final exponent to consider is the one related to the specific heat, τ. As a thought experiment, if we consider a strain-free motion, i.e., where the strain is zero but the temperature is not equal to the reference temperature, the energy release rate given in (5.13) becomes

$$G = -\frac{\tau c (1-\phi)^{\tau-1}}{2\theta_R}(\theta - \theta_R)^2. \tag{5.18}$$

Clearly, because $\theta_R > 0$ and $c > 0$, the energy release rate will be negative, and hence no damage evolution will occur if $\tau > 0$, under the circumstances of strain free motion. We then consider the following question: should purely thermal events cause microstructural change, specifically an increase in the damage? Such a situation is not unimaginable, if one heats a block of a material with an extremely low CTE, while exerting no mechanical forces on it, one essentially has created such an experiment. Thus, if $\tau < 0$, then we presume to have a material and a

theory under which microcracking is advanced by purely thermal events, and which appears to suggest that the specific heat of a material grows with microcracking.

Realistically, even in the case of brittle materials with small coefficients of thermal expansion, thermal shock is an important failure mechanism to recognize. If τ is positive, then from the energy release rate in (5.13) we deduce that the damage will only evolve after the thermally induced strain is large enough to counteract the presence of elevated temperatures. Thus, $\tau > 0$ implies that the material becomes more resistant to fracture with an increase in temperature. Additionally, the free energy (5.12) will go to zero as $\phi \to 1$ and the ability of the material to store heat will diminish as the material becomes more damaged. At this point, we turn to the simulations to draw further conclusions.

As a preliminary study, we simply assume that all of the exponents take the values

$$\alpha = \beta = \gamma = \tau = 2. \tag{5.19}$$

The results are shown in Figures 5.4 and 5.5, in space-time format. The simulations cover a relatively brief period of time of just over $500\,\mu$s. Full coupling between the elastic, thermal, and damage phenomena is clearly present. As the displacement wave caused by the briefly applied force approaches the fixed end of the bar (left side in Figures 5.4 and 5.5), one can clearly see that the strain increases to the point where it surpasses the critical energy release rate, and damage starts to evolve. Consequently, the temperature increases rapidly and in a very localized manner. As the wave reflects and moves away from the fixed end, the strains decrease, the damage stops growing, and the localized temperature reaches a steady, but slightly decreasing value. The time scale of these simulations is small with respect to the diffusion of thermal phenomena, thus, it appears in Figure 5.5 that the temperature remains constant after damage evolution at a point, but this is only an artifact of the difference in timescales.

Note that only after a few cycles of the wave reflecting off the fixed end, the damage variable is already at about one-tenth of its maximum value. This indicates that the combined values of η_C and the applied force are rather large compared to those used for modeling high cycle fatigue. Additionally, we see in Figure 5.6 that the damage is never decreasing. Given the nature of the algorithms described in Chapter 4 and physical derivations in Chapter 3, this is appropriate. This particular

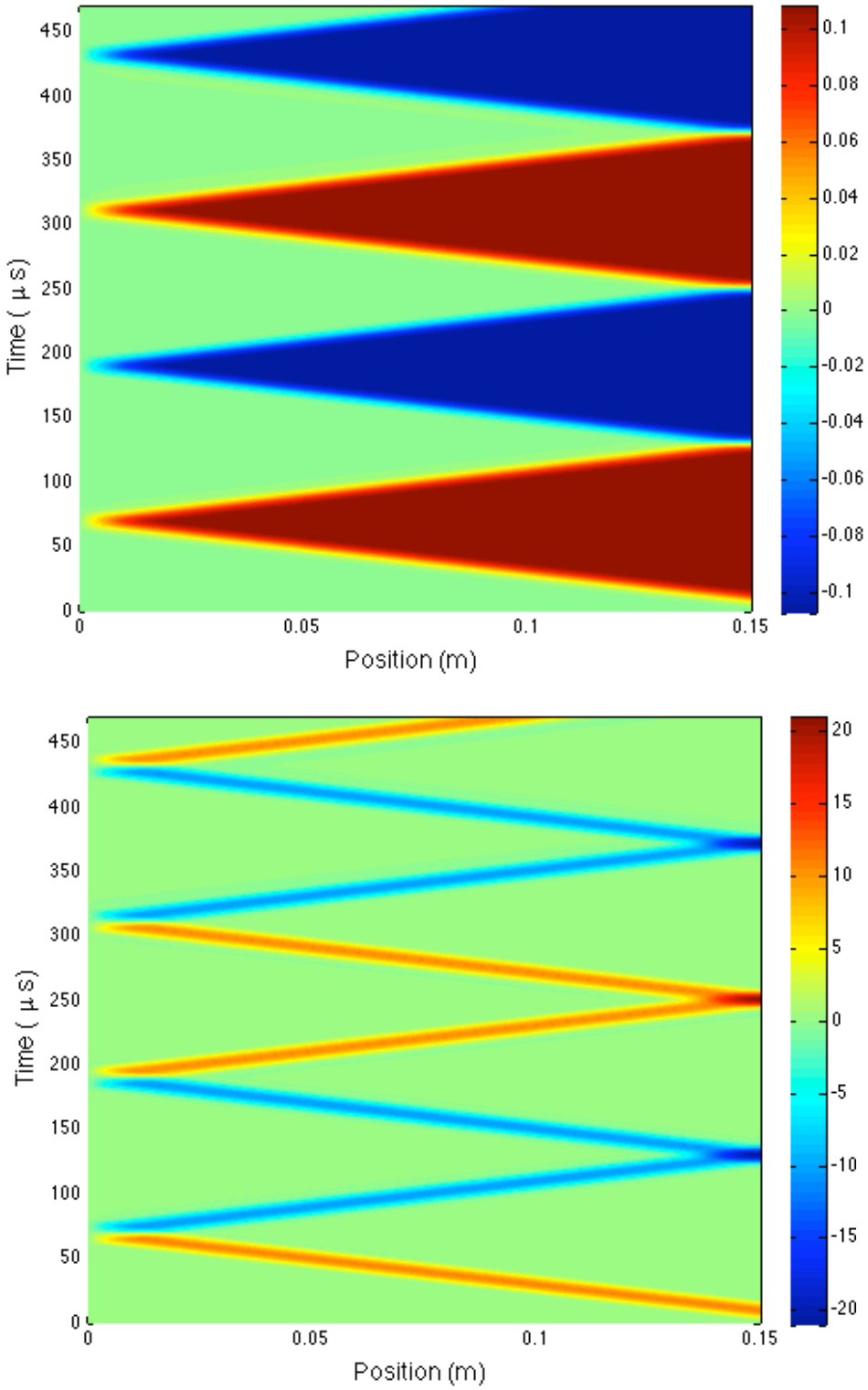

Figure 5.4. The displacement (top), in millimeters, and velocity (bottom), in meters per second, of the 1D bar subjected to the loading given in (5.9). The propagation of a wave front is clearly visible, along with the reflections against the fixed end (left) and free end (right).

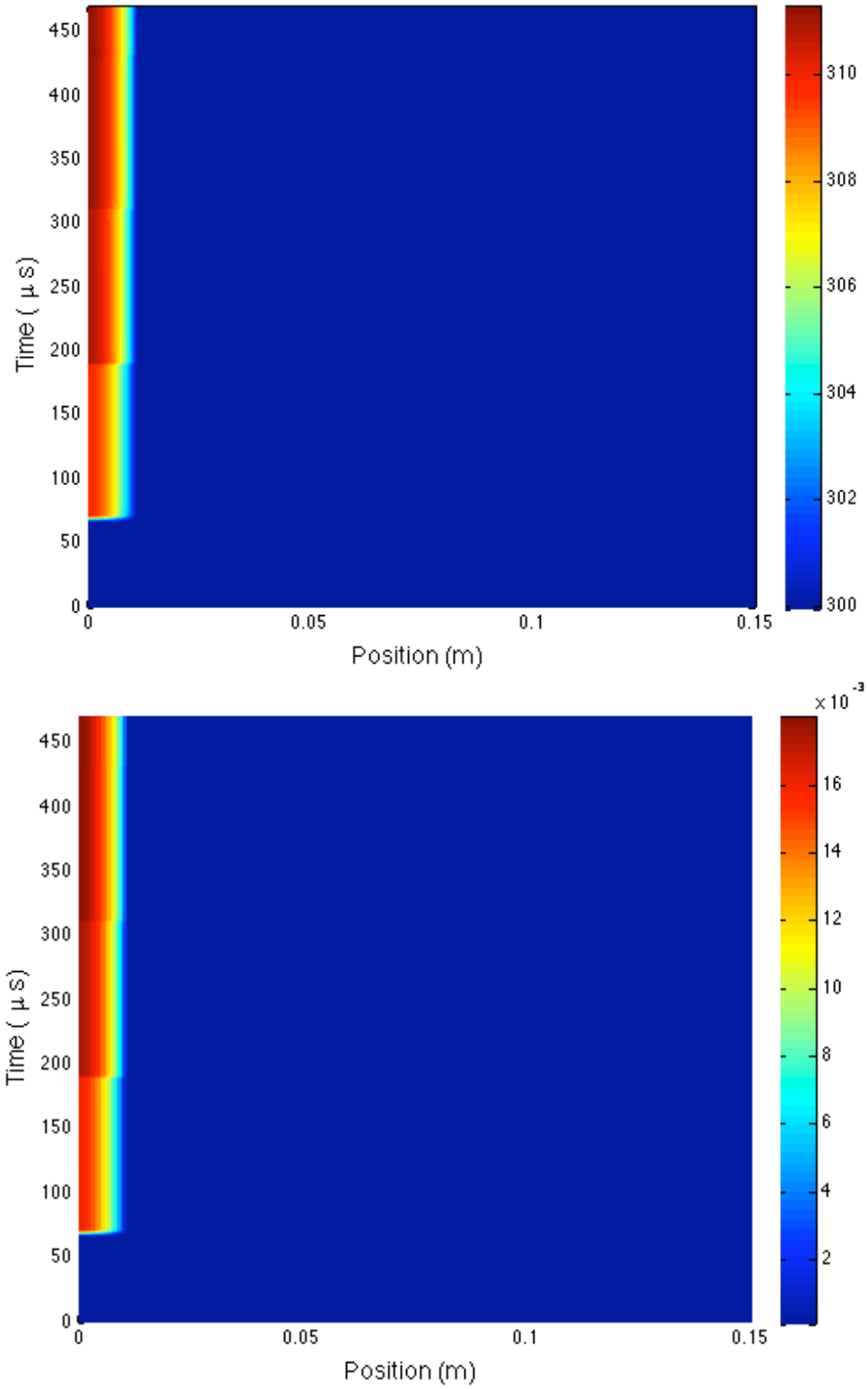

Figure 5.5. The absolute temperature (top) and damage variable (bottom) of the 1D bar subjected to the loading given in (5.9). Notice that the increase in damage is localized to the fixed (left) end of the bar and only evolves when the wave front strikes this end. The corresponding heating generated by an increase in damage is clear, and is significant.

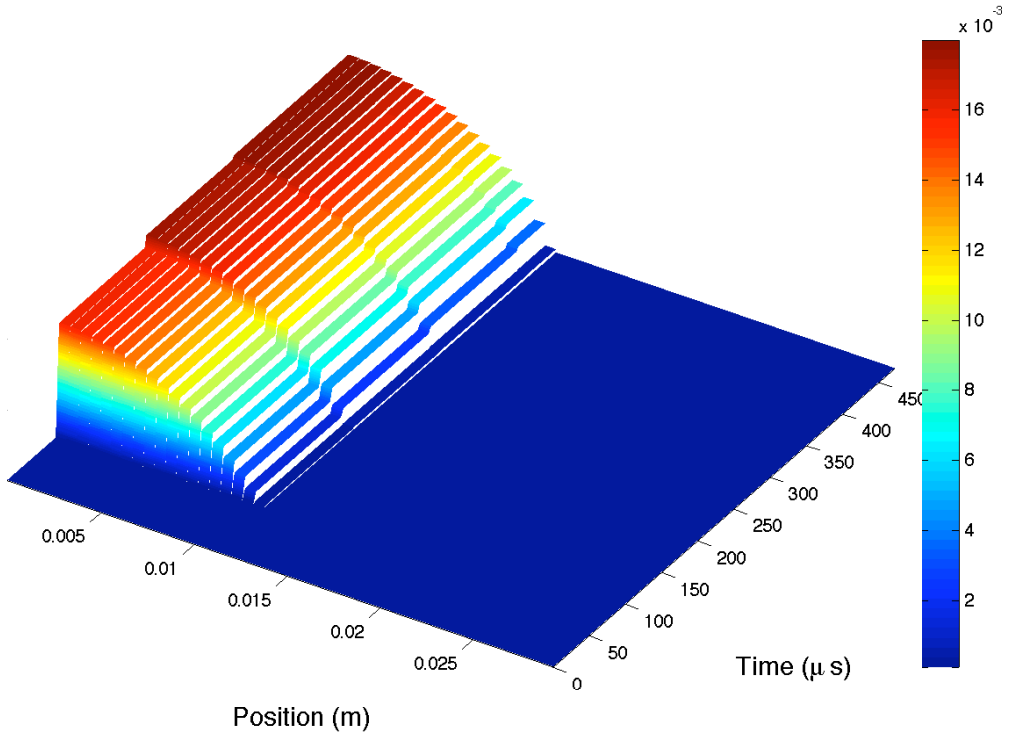

Figure 5.6. Zoom-in of the damage evolution at the fixed end of the bar from Figure 5.5. Note that damage increases rapidly each time the wave strikes the fixed end of the bar. The spatially-discontinuous nature of the damage is obvious in this figure. Each cycle of wave incidence on the fixed end is clearly visible. Also, the largest values for damage are at $X = 0$.

experiment was planned such that all of the interesting phenomena would happen at the fixed end of the bar, where $X = 0$. Using this knowledge, we can compare many simulations by looking at the time evolution of the fields at this location. Because we are primarily concerned with the change in evolution of the damage variable due to temperature, we will use the temperature and damage evolution as the primary metric used to study the effects of varying α, β, γ, and τ.

How to proceed with adjusting the values of the aforementioned exponents is an interesting problem unto itself. With four parameters, there is quite a large parameter space that can be explored; however, we hope to abbreviate the process in order to maintain clarity and to be able to draw useful conclusions. We begin first by examining the purely elastic part of the problem, i.e., we set to zero α, γ, τ, and adjust β. From the equations of motion, it is clear that this will not result in damage evolution induced heating, but will allow us to study the parameter space

of β. After this study, a value of β is selected, and each of the thermal exponents is adjusted independently, i.e., β is held fixed at a non-zero value, two of α, γ, τ are zero, and the third is marched through the domain of previously discussed values. We must have a non-zero value of β for the subsequent investigations because we know that in reality, even in a purely elastic system, β will never be non-positive. In this manner, we can determine which of α, γ, and τ matters most independently. Should any particular values stand out as interesting choices, we can then proceed to further explore the parameter space.

We first seek to see the effect that adjusting β has on this model. The parameter is related to the purely elastic part of the system, and corresponds to the relations most commonly used in the literature. Therefore, we set all other exponents to zero, and vary β through the domains given in (5.16). Figure 5.7 shows the effect that adjusting β has on the evolution of the damage. In this specific problem (which has been chosen with the hope of preserving generality), values of β that are less than one do not give rise to damage evolution.

For a one-dimensional model, a value of $\phi = 1$ in the domain indicates complete failure, and that the simulation is over. In Figure 5.7, we do not see this occur,

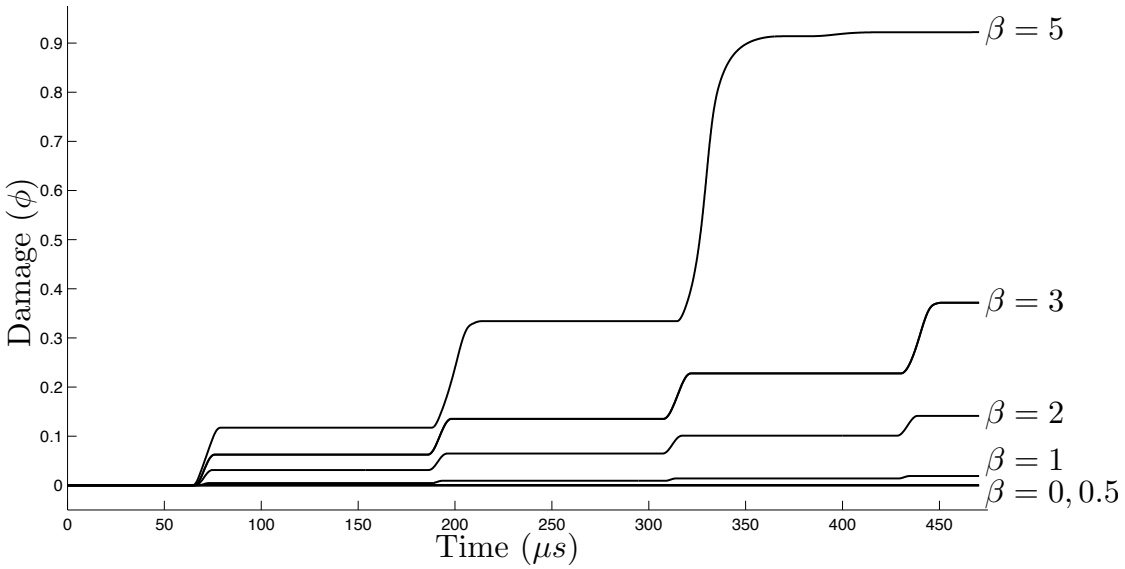

Figure 5.7. The damage evolution at $X = 0$, the fixed end of the bar, when $\alpha = \tau = \gamma = 0$ and β is varied. The value of β has a clear effect on the damage evolution. Larger values of β result in more rapid damage evolution; however, if the value of β become "too large" the model becomes unable to maintain physical relevance.

but when $\beta = 5$ the model approaches but does not quite attain the value of $\phi = 1$. This behavior is due to the damage dependence of G, and is the direct result of the fact that rapid damage increase causes a decrease in the energy release rate, and hence a slowing of the damage evolution. This behavior demonstrates the two-way coupling present in this model.

The values of $\beta = 1, 2, 3$ show the types of results that, in the opinion of the author, are more interesting. Here, the damage variable evolves at different rates for the same loading and material properties, and will eventually reach the maximum value of $\phi = 1$. For the subsequent simulations, we will choose the value of $\beta = 2$, so that, given the material properties in Table 5.1 and loading in (5.9), the simulations will span multiple loading cycles.

With a value of β selected, we now seek the effect of varying α and γ on the temperature and damage evolution. Figures 5.8 and 5.9 show the effects of fixing $\beta = 2$, $\tau = 0$, and varying either α or γ. It is clear that neither of these exponents independently affects the temperature or damage evolution at the fixed end of the bar (this is also true of the rest of the bar) in an extreme manner; however, it is observed that for large values of γ, the thermomechanical coupling is reduced so much that it ceases to affect the motion of the system, leaving the slight temperature increase it created to diffuse into the bar. This is not entirely surprising, as the

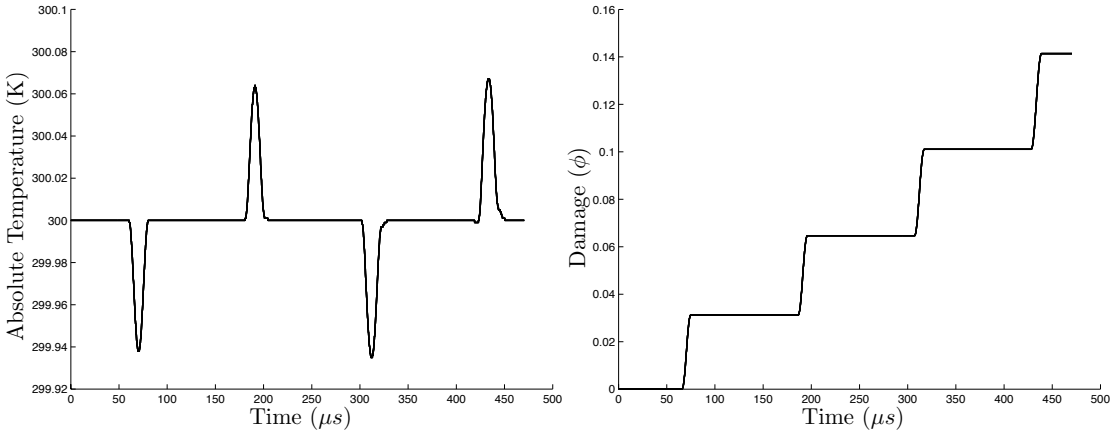

Figure 5.8. The temperature (left) and damage evolution (right) at $X = 0$, the fixed end of the bar, when $\beta = 2$, $\tau = \gamma = 0$, and $\alpha = 0, 0.5, 1, 2, 10, 100$. It is clear that α is not independently responsible for causing temperature variations or changes in the damage evolution. The oscillating temperature pattern is due to thermoelastic heating and cooling.

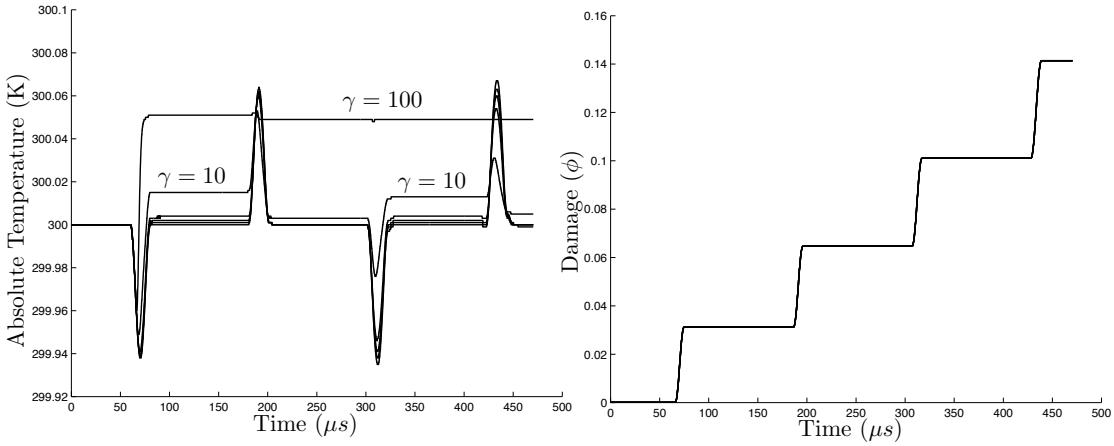

Figure 5.9. The temperature (left) and damage evolution (right) at $X = 0$, the fixed end of the bar, when $\beta = 2$, $\tau = \alpha = 0$, and $\gamma = 0, 0.5, 1, 2, 10, 100$. As with α, it is clear that γ is not independently responsible for causing large temperature variations or changes in the damage evolution.

source terms (resulting from thermoelastic coupling) in the balance of energy that pertain to the exponent γ are distinctly influenced by the thermomechanical coupling, M, which as given in Table 5.1 is very small for brittle graphite. We therefore can only conclude that, *independently*, these exponents have essentially no direct influence on the damage-temperature relationship, although they may have a more pronounced effect when $\tau \neq 0$.

The final exponent to consider is τ, which is related to the specific heat of the system. In Figure 5.10, the temperature and damage evolution at the fixed end of the bar are shown when $\beta = 2$, $\alpha = \gamma = 0$, and τ is varied through a range of values. Compared to α and γ, the effect of adjusting τ on the evolution of both the damage and temperature is substantial. We see that non-zero values of τ lead to temperature increases at the fixed end of the bar. Experimental observations have shown that crack growth results in crack tip heating (see Ravi-Chandar et al., 2000), and as such, it is now reasonable to posit that τ should be non-negative in this model.

The relation between damage growth and heating is observed by comparing the evolution of both quantities in Figure 5.10. When damage growth is occurring, there is a corresponding sudden increase in temperature at the same location. Due to the boundary conditions of perfect insulation, as soon as the damage stops evolving, the temperature begins to decrease as the energy dissipated during damage evolution

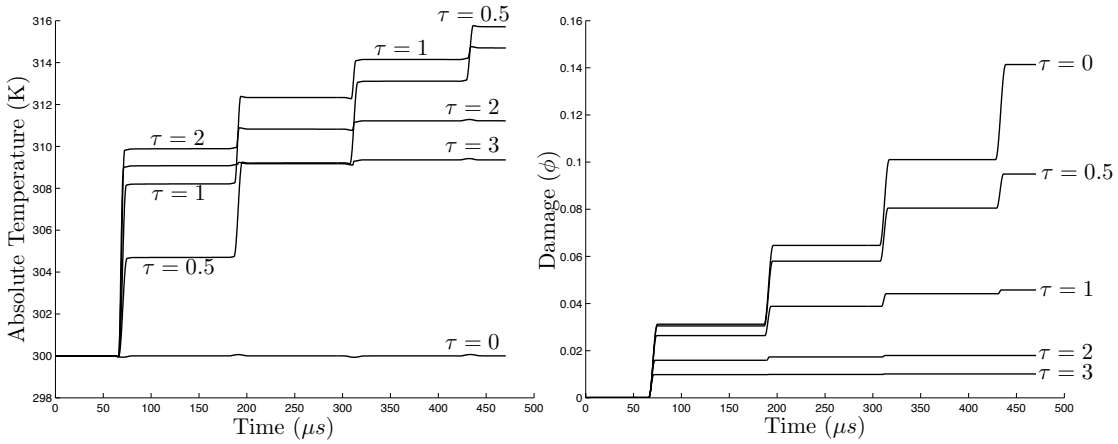

Figure 5.10. The temperature (left) and damage evolution (right) at $X = 0$, the fixed end of the bar, when $\beta = 2$, $\alpha = \gamma = 0$, and $\tau = 0, 0.5, 1, 2, 3$. It is clear that τ is independently responsible for causing damage evolution induced heating. Also, the damage evolution is affected by the value of τ, as it is clear that as τ is increased, more energy is dissipated as heat rather than put towards damage evolution.

begins to diffuse into the rest of the bar; however, this occurs very slowly due to the larger timescale of the thermal diffusion.

Figure 5.10 also demonstrates that while $\tau > 0$ couples temperature increases to damage growth, the damage growth is simultaneously influenced by the temperature. As τ increases, the damage evolution appears to slow. This is due to the fact that within the expression for the energy release rate in (5.13), a larger positive value of τ will actually cause the energy release rate to decrease, and is demonstrating that an increasing amount of energy is being dissipated as heat than is being consumed to evolve microcracking.

The coupling is not this straightforward, however, as it is clear that a larger value of τ may not always correspond to a larger increase in temperature. We can observe that the temperature, in this particular simulation, actually begins to fall again as $\tau > 0.5$. This is due to the fact that the damage growth slows considerably, and thus reduces the source term in the balance of energy. Therefore, the value of τ is critical to capturing the amount and ratio in which energy is dissipated via microstructure evolution or heat generation. The importance of this point cannot be overstated—without an explicit inclusion of the balance of energy, all other continuum damage models in pure elasticity assume that *all* energy is dissipated only by microstructure evolution, but here we are able to account for

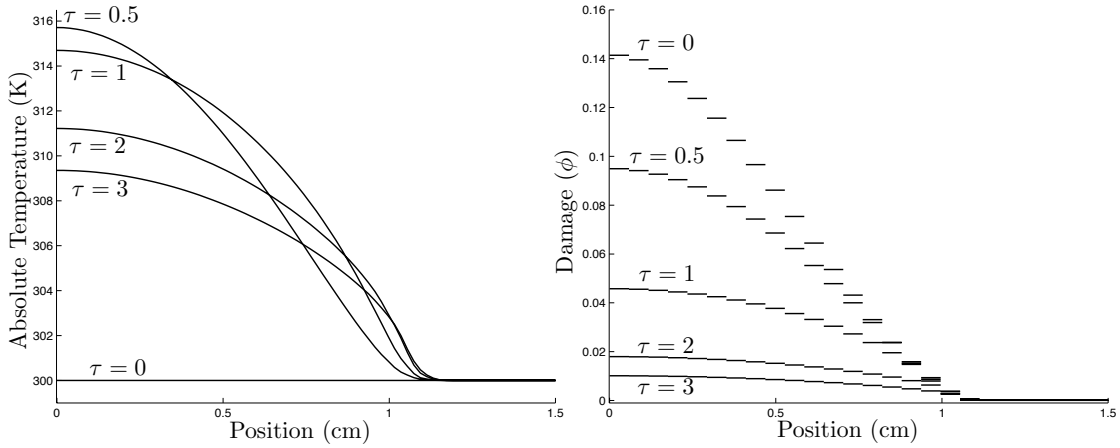

Figure 5.11. The temperature (left) and damage (right) at $t = 470.5\,\mu$s, near the fixed end of the bar, when $\beta = 2$, $\alpha = \gamma = 0$, and $\tau = 0, 0.5, 1, 2, 3$.

both thermal and damage energy dissipation and determine the proportions of each. We conclude from this that the specific heat, and specifically its dependence on the damage variable (microstructure), can play a critical role in thermomechanical CDM models.

The effects of β and τ are clearly important individually, and we now return to investigate further the effects of α and γ on the model. Selecting $\beta = 2$ and $\tau = 0.5$, we again search the spaces of $\alpha, \gamma > 0$ and observe the results. Figure 5.12 shows the effect of varying α in the same range as previously studied. The effect is measurable, although quite small. Increasing α results in slightly lower values of the damage, although the difference is roughly only a fraction of a percent relative to the value when $\alpha = 0$. In order preserve generality in future simulations, we will take a value of $\alpha = 2$ in subsequent calculations, because we do not want to remove the possibility that interesting phenomena may occur in other loading situations.

In Figure 5.13 we see virtually no effect on the temperature or damage evolution when γ is adjusted through a range of positive values. This is not surprising, as the thermomechanical coupling for this particular material is quite small. It is not expected, however, that this will be the case for all materials, and consequently the role of γ may be more important in later studies. In order not to lose generality in the model, we select the value of $\gamma = 2$ for subsequent calculations. It is tempting to simply use these results to consider $\gamma = 0$, but this could lead to a loss of generality when unforeseen effects arise. Additionally, the coefficient of thermal expansion

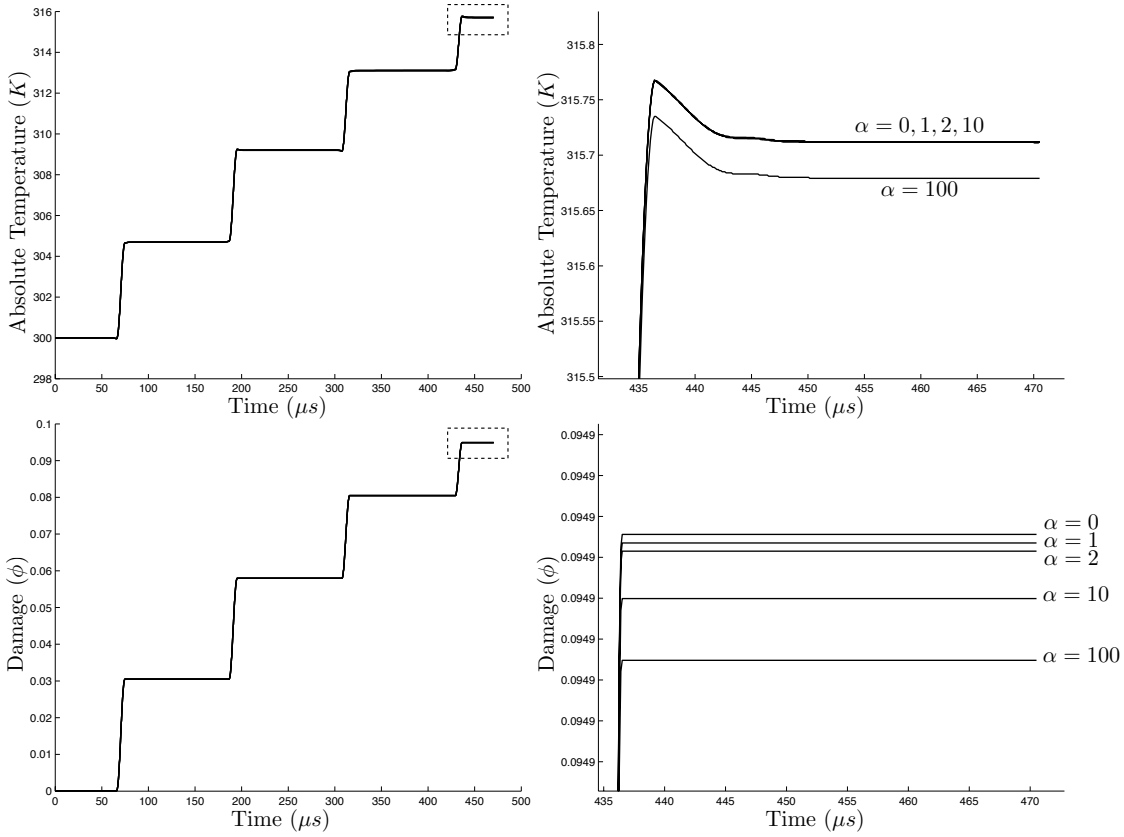

Figure 5.12. Temperature (top) and damage evolution (bottom) at the fixed end of the bar, $X = 0$, when $\beta = 2$, $\tau = 0.5$, $\gamma = 0$, and α is adjusted. The dashed-line boxes on the left indicate the enlarged region on the right. The effect is measurable, although not as pronounced as when τ is varied in Figure 5.10.

is well known to often have significant dependence on temperature, and as such, it may play a more interesting role in later simulations involving the non-linear thermoelastic theory.

In conclusion, the exponents β and τ appear to play the most dominant roles in this model. The effect of the former is well known, but the importance of τ, and more generally the importance of the dependence of the specific heat on the damage variable is an important original finding of this thesis. The coupling of the damage with the specific heat, which is ultimately derived from that part of the free energy of the system which is not dependent on deformation, appears to have a pronounced effect on what fraction of the energy dissipated during the evolution of the microstructure is dissipated as heat. Consequently, the specific heat also affects the rate at which damage grows, and alludes to a model capable of truly

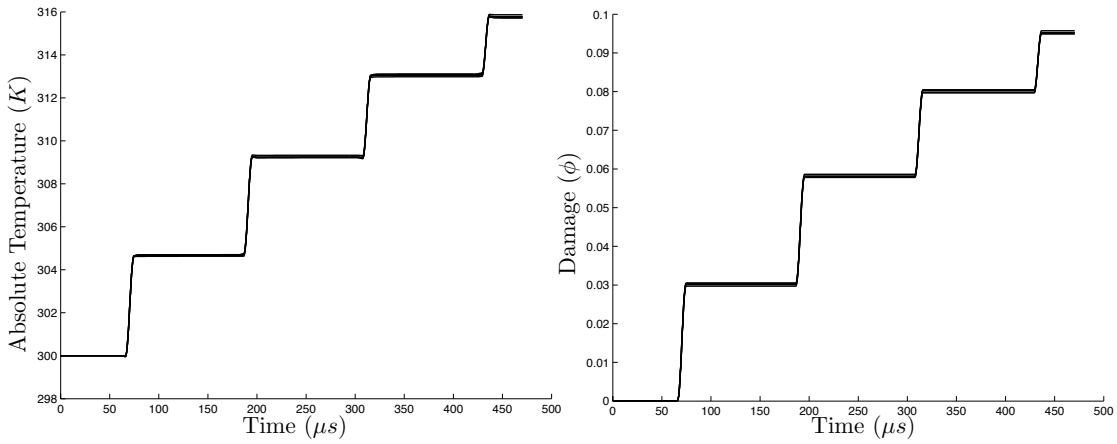

Figure 5.13. Temperature and damage evolution at the fixed end of the bar, $X = 0$, when $\beta = 2$, $\alpha = 0$, $\tau = 0.5$ and γ is adjusted through the value $\gamma = 0, 1, 2, 10, 100$. For both the temperature and damage, no noticeable effect is observed.

capturing the coupling between temperature and damage evolution.

All of the exponents have been postulated to be positive, through either physical reasoning or observation of numerical experiments and qualitative reconciliation with known experimental results. The final set of values for these exponents, to be used in forthcoming simulations, is

$$\alpha = 2, \qquad \beta = 2, \qquad \gamma = 2, \qquad \tau = 0.5. \tag{5.20}$$

It must be remembered that these values are *material properties*, and as such should be determined *empirically* for individual materials. The purpose of this section is to determine through physical reasoning, with the aid of simulations, if any specific ranges for these exponents can be identified and to what extent each exponent may be important. All of the results here are for brittle graphite, and hopefully may aid the plight of an experimentalist working to better characterize such a material.

5.3 Damage Evolution Material Properties

This section briefly explores the effect that the temperature dependence of the crack propagation parameter η_C and critical energy release rate G_{CR} have on the resulting behavior of the model, specifically with regards to the temperature and

damage evolution. As has been discussed throughout this thesis, we are not as concerned with a specific material as we are as the qualitative behavior of phase-field damage models for general application to brittle materials in the context of damage evolution, but more importantly, dynamic thermal phenomena. Thus, this section should be considered a demonstration of the capabilities and flexibility of the proposed model.

There is no *a priori* reason to assume that any specific forms for the temperature dependence of η_C and G_{CR} are universal, or generally representative of the natural world. This is surely a question to be answered by careful analysis of the underlying micromechanical models used to develop the damage variable and corresponding evolution equation, and by experimental testing. Even by restricting the discussion to situations where η_C and G_{CR}, which will be referred to frequently as the damage evolution material properties, increase or decrease monotonically with temperature, one still is faced with four permutations where temperature could be causing either η_C and/or G_{CR} to increase or decrease.

Compounding the issue of temperature dependence is that the model is already sensitive to the values of the damage evolution material properties. Figure 5.14 shows the result of varying the value of G_{CR} slightly, and the resulting change in the damage evolution, given the same loading. Again, this section can be viewed more as a demonstration of how temperature affects the damage evolution in this model, and is not meant to make broad claims about the behavior of brittle materials in general.

While the dependence of η_C and G_{CR} on the damage is also important, this topic has been explored by other authors (see, e.g., the discussions in Krajcinovic, 1996), the work of whom could be incorporated into this model if desired. For example, one possible assumption is that the crack propagation parameter η_C increases with an increase in the damage variable, which may correspond to a physical assumption that microcracks will grow faster in the vicinity of each other due to phenomenon associated with crack-tip interaction. However, assuming that microcracks grow faster when in the vicinity of other microcracks does not mean that it will be equally easy to have microcracking evolving. In fact, phenomena such as crack shielding (see, e.g., Majumdar and Burns, 1981 and Hutchinson, 1987) have been observed to reduce the load at the macrocrack-tip due to decreased stiffness of the

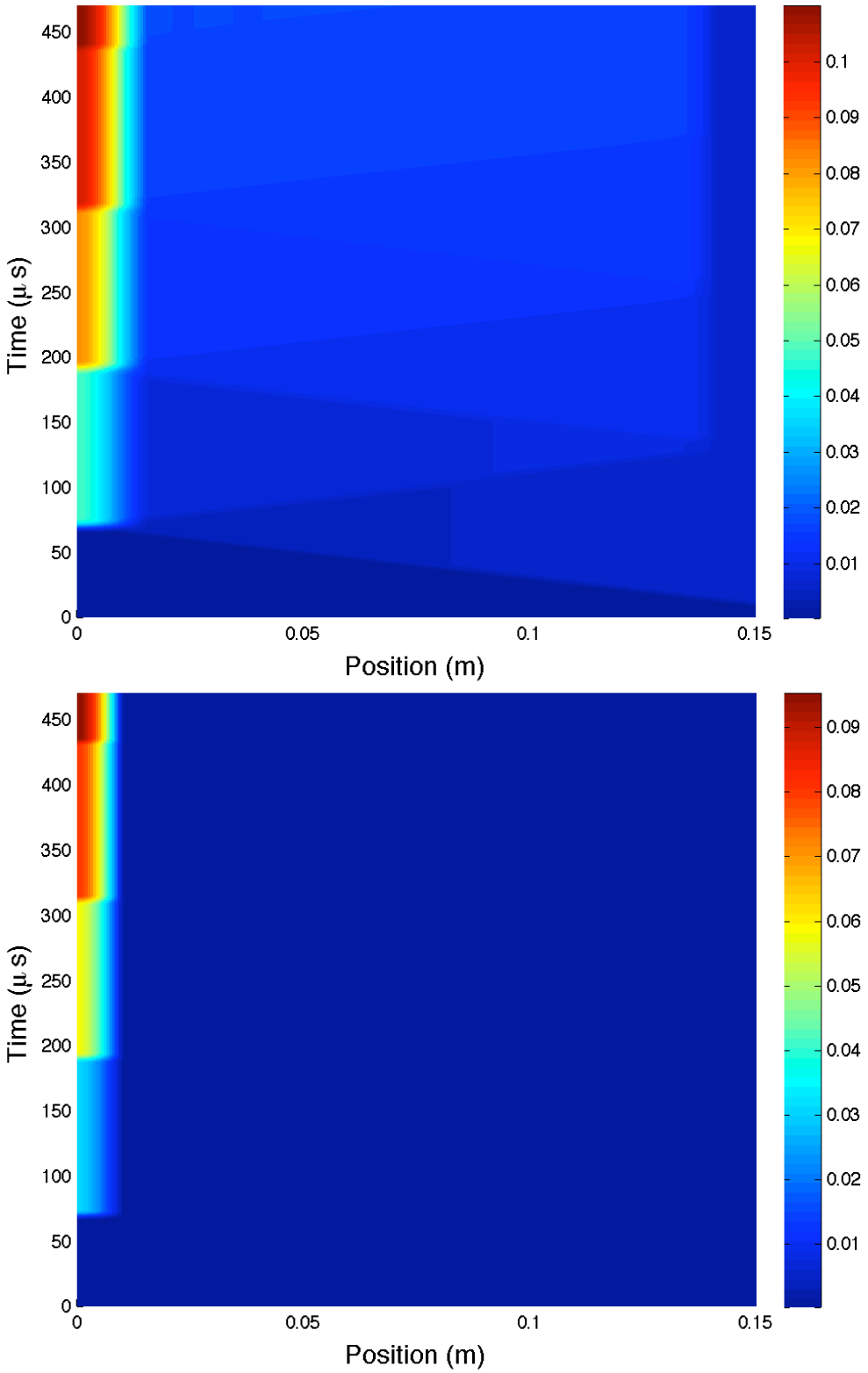

Figure 5.14. The damage field when $G_{CR} = 1 \times 10^5\,\mathrm{J/m^3}$ (top) and when $G_{CR} = 3 \times 10^5\,\mathrm{J/m^3}$ (bottom). Even values of the same order of magnitude can result in quite different evolution of the damage.

surrounding microcracked material. The damage dependence of both η_C and G_{CR} is often important, but for the purpose of clarity when studying the thermal effects, we choose exclude it in this dissertation.

In the same manner as damage dependence, temperature may cause the material to become embrittled or softened. High density graphite is known to increase in stiffness as temperature increases (see Appendix A), which suggests that it becomes more brittle as the temperature increases; however, it is also true that many materials soften, or become more resistant to fracture, as they are heated. In order to explore these possibilities, we posit that a simple temperature dependence for the crack propagation parameter could be written as

$$\eta_C(\theta) = \eta_C^0 \left(\frac{\theta}{\theta_R} \right)^a . \tag{5.21}$$

Note that this formulation assumes no change in η_C at the reference temperature. It is stressed that the form of the crack propagation in (5.21) is merely postulated for study of the qualitative nature of the model. For the critical energy release rate, we assume a similar form, and as such also define its temperature dependence as

$$G_{CR}(\theta) = G_{CR}^0 \left(\frac{\theta}{\theta_R} \right)^b . \tag{5.22}$$

Here a and b are simply scalar parameters to adjust during the study, and we take the constants in (5.21) and (5.22) as $\eta_C^0 = 1 \times 10^{-2}\,\mathrm{m}^3/\mathrm{J}\cdot\mathrm{s}$ and $G_{CR}^0 = 3 \times 10^5\,\mathrm{J/m}^3$. The exponents are the same as determined in the previous section, $\beta = \alpha = \gamma = 2$ and $\tau = 0.5$, for consistency of the presentation.

The effects of varying a and b independently are shown in Figures 5.15 and 5.16. As expected, when the critical energy release rate is constant, and a is varied to have the crack propagation parameter change with temperature, we see a direct influence over the temperature and damage evolution at the fixed end of the bar. In Figure 5.15, we see that if η_C increases with temperature ($a > 0$), then the damage evolution occurs at an accelerated pace, and correspondingly so does the temperature. However, this simulation shows that at some point, the combination of damage and temperature is such that the initial loading does not cause a significant increase in damage after a certain time. Over time, as the temperature falls, the

energy release rate would again rise above the critical level, and we will see damage grow at the fixed end of the bar once again. This is an excellent example of the large parameter space of this model, and the unexpected coupling effects that can be seen. Likewise, in Figure 5.16 we see that if the critical energy release rate is diminished as temperature increases ($b < 0$), the damage and temperature growth is accelerated. Note that in both cases, the trend for the damage and temperature at the fixed end of the bar is the same (either increasing or decreasing), which is markedly different from the case of the specific heat, where the coupling was much more intricate. This is due to the fact that these parameters are only present in the damage evolution, and not the rest of the model.

In conclusion, it is clear that many material responses may be explored by using different combinations of temperature dependent forms of η_C and G_{CR}. The focus of this dissertation is on brittle materials, and as such we will examine a case where the material becomes more brittle as the temperature increases, i.e., $a > 0$ and $b < 0$. As a note, due to the chosen operator splitting scheme, changes to the temperature dependence of η_C and G_{CR} are very easy to implement.

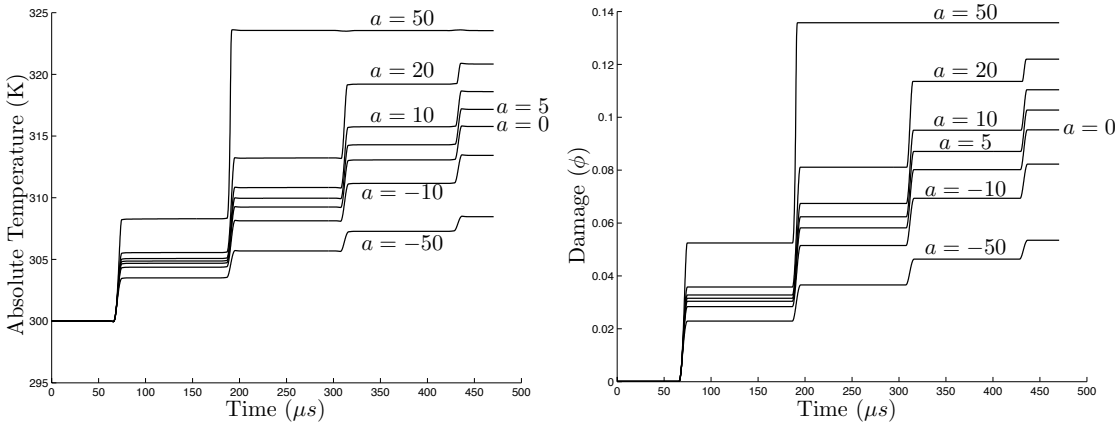

Figure 5.15. Temperature (left) and damage (right) evolution at the fixed end of the bar, $X = 0$, when $b = 0$ and a is adjusted. Unlike the exponent for the specific heat, as η_C increases, we see an increase in both the temperature and damage; likewise for a decrease.

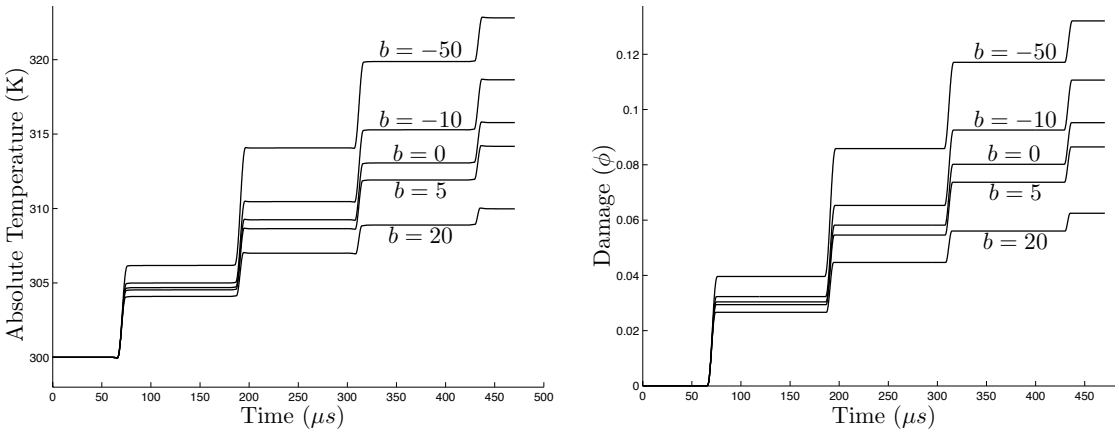

Figure 5.16. Temperature (left) and damage evolution (right) at the fixed end of the bar, $X = 0$, when $a = 0$ and b is adjusted. An inverse relationship is present: as b increases, so does G_{CR}, leading to a decrease in damage evolution and subsequently a decrease in temperature.

5.4 Brittle Fracture

This section demonstrates the capability of the proposed model to simulate brittle fracture. Until this point, the numerical studies have only focused on brittle behavior by using thermoelastic material properties for a common brittle material, namely bulk high-density graphite. Now we will explore the damage evolution material properties, focusing on values that are appropriate for modeling fracture, i.e., the sudden localized failure at a point in the body.

Recalling the discussions in Chapter 2 and Chapter 3 regarding the damage evolution equation, we will investigate brittle failure by increasing the crack propagation parameter to the point that once damage is nucleated, it will grow very quickly, resulting in almost immediate failure of the one-dimensional bar. Additionally, it is also assumed that η_C increases with temperature ($a > 0$) and that G_{CR} decreases with temperature ($b < 0$), corresponding to an embrittlement of the material with an increase in temperature.

For the subsequent simulations, we will break from the previous sections, and select different values for the exponents for the constitutive relations. This is not because the previous values are incorrect, but rather to provide clarity in the example calculations; this is done to minimize the complex coupling that may, as demonstrated previously, prevent damage from growing to its maximum value due

to complex couplings in the formulation. Thus, we choose $\beta = 1$, $\alpha = \gamma = 2$ and $\tau = 0.025$. For the same reason, we also adjust the loading given in (5.9) to be

$$\sigma(L,t) = \begin{cases} \frac{1}{2} s_0 \left[1 - \cos\left(2\pi t/t_0\right)\right] & t < t_0/2 \\ s_0 & \text{otherwise} \end{cases}, \tag{5.23}$$

where the loading is increasing smoothly, then held constant. Hence, rather than a pulse, we now have what corresponds to a dead weight being applied to the left end ($X = L$) of the bar. The applied force and its timescale are the same as given in (5.9), as is the critical energy release rate $G^0_{CR} = 3 \times 10^5\,\mathrm{J/m^3}$. However, we now select a larger value of the crack growth parameter $\eta^0_C = 1 \times 10^1\,\mathrm{m^3/J{\cdot}s}$, as compared to the previous value of $\eta^0_C = 1 \times 10^{-2}\,\mathrm{m^3/J{\cdot}s}$.

The temperature and damage field resulting from this choice of material properties are shown in Figure 5.17. The first observation is that even though the damage grows much faster, it still does not jump directly to $\phi = 1$. This is due to the selection of the timestep; even though the damage grows quickly we can still characterize its growth. Figure 5.18 details the growth of the temperature and damage fields through time. The high rate of the damage growth is clear from

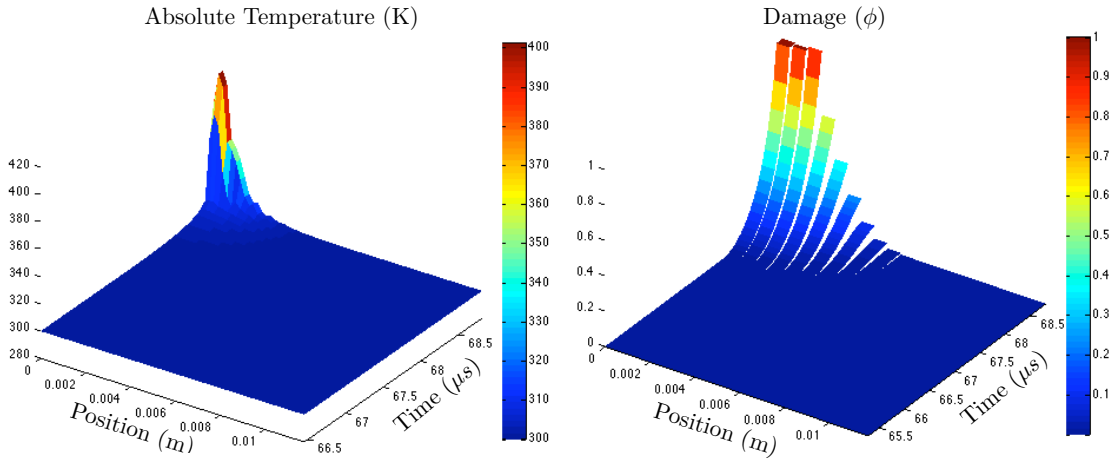

Figure 5.17. The temperature (left) and damage fields (right) when damage evolution occurs very rapidly, i.e., brittle failure is being modeled. In this simulation, the constitutive exponents are selected to provide maximum clarity in the results, and are $\beta = 1$, $\alpha = \gamma = 2$, and $\tau = 0.025$. Additionally, temperature dependence of η_C and G_{CR} are assumed, with $a = 10$ and $b = -10$, corresponding to an embrittlement of the material as temperature increases.

the indicated times; only a tenth of a microsecond is passing between the damage profiles shown.

In both Figure 5.17 and Figure 5.18, we see that the temperature field is also growing quickly, and while not very smooth, is not necessarily demonstrating instability in the solution. However, experience with this model has shown that as the rate of damage growth increases, it becomes more difficult for the numerics to cope with the nature of the equations. This is likely due to the fact that the change in damage is what causes the problem to become non-linear in the first place, and hence the larger the change in $\dot{\phi}$ the more severe the non-linearity in the problem. Compounding this issue is the fact that as damage quickly approaches $\phi = 1$, the nature of the equations is locally altered.

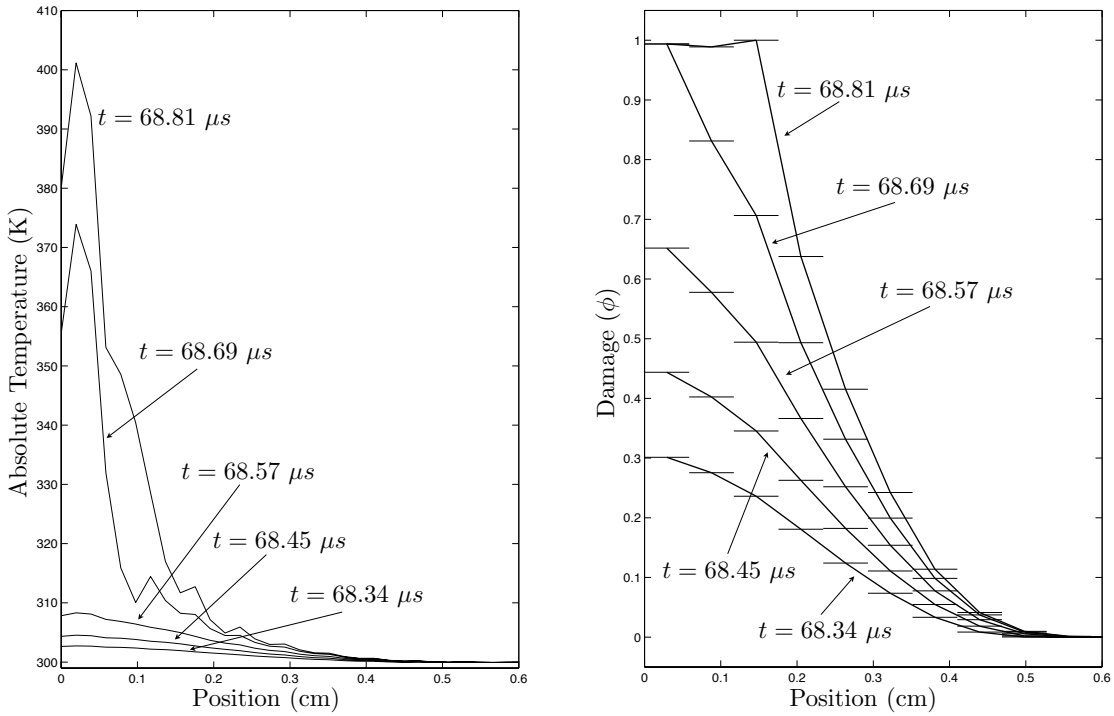

Figure 5.18. The temperature (left) and damage (right) fields when damage evolution occurs very rapidly, i.e., brittle failure is being modeled at timesteps leading up to failure. Note the rapid rise in damage and temperature, and how the temperature struggles to cope with the localized nature of the damage field. In this simulation, the constitutive exponents are selected to provide maximum clarity in the results, and are $\beta = 1$, $\alpha = \gamma = 2$, and $\tau = 0.025$. Additionally, temperature dependence of η_C and G_{CR} are assumed, with $a = 10$ and $b = -10$, corresponding to an embrittlement of the material as temperature increases.

The careful interpretation of these results is critical to ascertaining the usefulness of this model. From the outset of this dissertation, it has been stated that one of our goals is to explore whether the modeling of brittle fracture is even viable in the context of continuum damage mechanics, especially when dynamic and thermal effects are explored. Clearly, Figure 5.18 demonstrates that both the physical model and numerical methods proposed are capable of resolving and coupling the rapid and localized failure and temperature increases associated with fracture; however, since we are presenting this technique without rigorous validation we are not in a position to make more specific claims about the data generated from the model. For example, it may be very interesting to know if the damage and temperature fields generated are qualitatively, if not quantitatively, representative of what is observed empirically. Additionally, whether the rate of growth of these fields is accurate is also an interesting question.

The number of assumptions necessary to get to this point prohibits a more in-depth study of specific scenarios; however, the act of arriving at this point has revealed in detail the key elements necessary to be able to make more specific claims. Clearly, the dependence of the constitutive quantities on damage, especially the thermal ones, needs to be quantified. We have shown in this chapter that, of the thermal material properties, a primary focus should be the damage dependence of the specific heat. Additionally, knowledge about the material's response to heat, i.e., whether it undergoes softening, embrittlement, or some combination of the two is important to understanding the final motion of the body. With these topics in mind, we hope to have narrowed the questions that need answered by future research.

Chapter 6

Adaptive Mesh Refinement

This chapter details the development, implementation, and performance of a proposed adaptive finite element method to solve the problems derived in Chapter 3. Motivation for employing adaptive methods is presented first, followed by a brief discussion of the nature and general structure of such algorithms. The development of two original refinement indicators and the corresponding algorithms is detailed. Finally, a demonstration of the current state of the algorithm's performance is given.

Like many numerical methods, the finite element method relies on the partitioning of a domain into a finite number of smaller, disjoint subdomains. An approximate solution is then calculated using this partition, and some measure of the error in the approximate solution is calculated. Decreasing the size of the subdomains, or elements, in the partition is referred to as refinement, while an increase in the size of the elements is called coarsening. Typically, one expects that as the partition, or mesh, is uniformly refined, the error present in the approximate solution should decrease correspondingly. In this thesis, we have already employed this technique in Chapter 4, where convergence of the numerical formulations was demonstrated. Well known relations between the size of the elements and the error in the approximate solution have been developed and fully vetted by the mathematical community (see, for example, Brenner and Scott, 1994).

While uniform refinement produces a reduction in error, and hence a more accurate solution, it simultaneously results in a substantial increase in computational cost. To this end, adaptive mesh refinement methods have been created to increase

the refinement of the mesh locally instead of globally, such that the error in the approximate solution can be reduced with a minimal increase in computational cost. In this thesis, we posit that the level of mesh refinement necessary to resolve the damage, and hence the morphology of the microstructure, is such that adaptive mesh refinement will be crucial to containing the size of the calculations, in terms of the total number of unknowns for which we are solving. We also have stated that we desire an algorithm which has no *a priori* assumption of where damage will occur within the domain, and hence, since we choose to forego uniform refinement techniques, must develop an algorithm that is able to autonomously determine where it is necessary to refine the mesh.

Adaptive methods in numerical analysis are those techniques and algorithms which, through a series of calculations, automatically refine the space/time discretization underlying an approximate solution in a non-uniform manner. These techniques grew out of the need to minimize the computational expense normally associated with high-precision calculations. Whenever a domain discretization method is used to find an approximate solution of some system, one must choose a triangulation, that is, a decomposition of the domain into a finite number of disjoint subdomains. If, after the calculation is performed, the approximate solution obtained is not accurate enough by some method of error measurement, then one may manually change the discretization according to either experience, intuition, or at best an educated guess, with the hope of finding a more accurate approximate solution. Clearly, this process could iterate indefinitely if one is either unskilled, or unable to determine the root cause leading to the unacceptability of the approximate solution. Therefore, algorithms were created which automatically determine how the triangulation should be adjusted, perform such an adjustment, and recalculate the solution.

In this thesis, a primary emphasis has been the application of the finite element method to the problem of thermoelasticity with damage. Therefore, this chapter will focus on the application of an adaptive scheme in conjunction with the particular finite element method already presented. With this in mind, we begin by pointing out that there are three general classes of adaptive finite element methods*: *h*-

*Recently, other methods have been proposed; we choose here to list only the methods commonly in use by the broader community.

adaptive schemes, where the mesh size is adjusted locally, resulting in an expanded set of basis functions (although still all of the same type); p-adaptive schemes, where the solution spaces are changed only by modifying the nature and number of the basis functions; and hp-schemes, which combine both approaches (see, e.g., Pannwitz et al., 2003 and Bangerth et al., 2006). As already detailed in Chapter 4, the selection of approximate solution spaces for the problem of thermoelasticity with damage has been carefully studied, and as such it is not anticipated that p-adaptive schemes are appropriate for the problem at hand. Therefore, we focus on the use of h-adaptive schemes, which are also known more simply as adaptive mesh refinement.

Adaptive mesh refinement (AMR) is critical to addressing the localization of the damage solution while maintaining reasonable problem sizes, in terms of the total number of unknowns. While it will be shown to be useful as a tool, it is not a well defined procedure or miracle cure for problems of this nature. The use of AMR does not remove the localization of, or intrinsic mesh dependent nature of the damage solution. Rather, it provides a framework in which the localization of the damage variable can be contained to a physically reasonable part of the domain. We must recall that the damage variable represents the extent to which microcracking is present in the body, on a pointwise basis. As damage evolves, and reaches its maximal level at a point ($\phi = 1$), we say the body is totally failed at that point. In essence, this physically corresponds to the coalescence of the microcracks into macrocrack, and hence the creation of a new surface in the body; however, in this dissertation, cracks and the subsequent creation of new surfaces are not modeled explicitly.

In one-dimensional calculations, the simulation ends whenever a single point in the domain has a damage value of $\phi = 1$. However, in two and three dimensional calculations this is no longer the case. The issue of what it means to have material in a domain with $\phi = 1$ is discussed in Mazars (1996), among others, where it is stated that such zones of fully-damaged material represent a macrocrack. One must remember that we are simply creating a *model* for fracture, which is inherently discontinuous, within a fully continuum framework. In this chapter, we explore the possibility of using discontinuous finite element methods and AMR to help determine if such an approach is feasible.

6.1 h-adaptive Algorithm

Adaptive finite element methods are well developed, and have been studied extensively since the work of Babuška (1975), among others, resulting in a plethora of techniques (see De et al., 1983). Intrinsically coupled to adaptive mesh refinement is the study of error estimation. In this thesis, the widely used concept of *a posteriori* error estimation and mesh refinement is employed (see, e.g., Babuška and Rheinboldt, 1978 and Kelly et al., 1983). More recent advances in the field, such as duality-based error estimation, can be found in Pannwitz et al. (2003), and throughout the literature. AMR algorithms are not unique, and are highly dependent on the mathematical and physical nature of the problem to be solved; however, a general procedure is followed in most schemes.

The basic process of *a posteriori* driven adaptive mesh refinement is detailed in Figure 6.1. The process begins with the selection of an initial triangulation, or mesh, for a given domain. An approximate solution over this discretization is then found using the finite element method. Subsequently, the global error present in the approximate solution is calculated according to some measure (for examples of such measures, see Section 4.3.1). If the magnitude of this error is not acceptable, then error estimates per cell, denoted by e_K (where K is a cell in the triangulation $\mathcal{T}_h$), are calculated for each cell in the triangulation. The choice of e_K is one of the most important elements in the implementation of an AMR algorithm, and is highly influenced by the choice of solution spaces, the nature of the equations being solved, and the physical phenomena for which one wishes to increase the accuracy of the solution. Following the calculation of the error estimates, a set of refinement indicators is generated, which in turn determine where the mesh is going to be refined. This is another crucial decision in the development of an AMR algorithm, and is often something that must be tuned for the problem at hand. The refinement indicators are often a function of the error estimates, as it is logical to locally refine the mesh where the error in the solution is the highest; however, it is not necessary that this be the case. For example, in this dissertation, we focus on refining in the regions of the domain where damage is evolving, which may differ from areas of the domain where the error in the thermoelastic fields is highest. At all times, a distinction between the error estimates and refinement indicators must

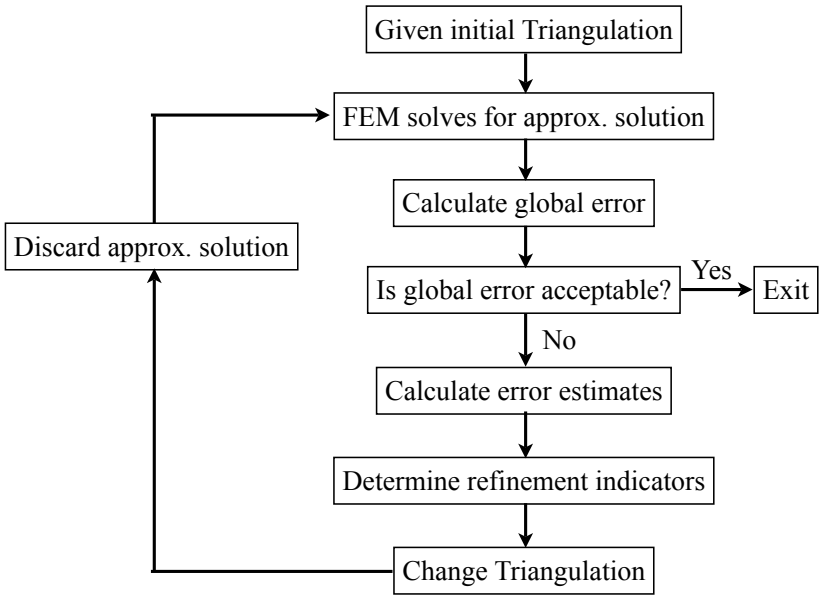

Figure 6.1. Flowchart of a general *a posteriori* driven AMR scheme. Key parts to the process are the choice of error estimates, definition of refinement indicators, and how to change the triangulation.

be made. Finally, the previously calculated approximate solution is discarded, and the process repeated until an acceptable level of error is reached.

In this thesis, the calculation of error estimates is bypassed in favor of using physically motivated refinement indicators. Two methods for calculating the refinement indicators are proposed. The first uses only the damage variable, and is motivated by our interest in phenomena in the vicinity of where damage is growing and where damage has changed from its initial state. The second relies on the energy release rate, and is motivated by the fact that this quantity is a precursor to the evolution of the damage variable, and may serve to preemptively refine the mesh where necessary. In both cases, only refinement of the mesh is considered, as opposed to the usual combined approach of coarsening and refinement. This is because we want to study the morphology of the microstructure as it evolves, and hence will be only refining the mesh in order to resolve this in more detail.

Finally, it is important to note that the simulations in this chapter are demonstrative in nature. We wish to explore the effect that different refinement indicators have on the resulting solution, and specifically do not make any claims about validating the results. Such work is important, and necessary for the long term

deployment of the model proposed here, but for reasons explained in Chapter 7, is left for future studies.

6.1.1 Damage Derived Scheme

Let r_K denote the refinement indicator for a cell $K \in \mathcal{T}_K$, where $\mathcal{T}_K$ is a triangulation of the domain. Simple damage based refinement indicators are computed according to the following formula, where $0 \leq \epsilon_D \leq 1$ is a parameter selecting what ratio of total damage to rate of damage growth should be used, and ϕ^0 is the damage level in the initial condition,

$$r_K = \epsilon_D \left(\phi_K^{n+1} - \phi_K^0\right) + (1 - \epsilon_D) \frac{\phi_K^{n+1} - \phi_K^n}{\Delta t} \quad K \in \mathcal{T}_h. \tag{6.1}$$

Note that the damage variable has been subscripted by cell. This presents no problem when elements such as piecewise constant polynomials ($\mathcal{P}^0(K)$) are used to represent the damage variable, but if higher order elements are used a method must be developed to clarify what is meant by ϕ_K. As detailed in Babuška and Rheinboldt (1978), Kelly et al. (1983), and Pannwitz et al. (2003), a multitude of formulas have been proposed for calculating error estimates and refinement indicators, most of which are based on some sort of integration over the cell or its faces.

Due to the pathological mesh dependence of this model, adaptive mesh refinement must be used with care. For example, simply continuing to refine the mesh at a location where damage is evolving may not result in a convergent sequence of solutions. As discussed in Chapter 2 and Mariano (2000a), the volume of the damaged cells will simply decrease until they are not physically reasonable, and the dissipated energy will decrease to zero. Clearly, this is a primary motivator for one to explore non-local theories, but we suggest that the issue can be addressed reasonably well with a rather simple solution. As described in Lemaitre (1996), a minimum mesh size can be implemented. Many physical rationales can be used to justify such a minimum mesh size; however, due to the more general nature of this dissertation, we simply pick a reasonable h_{min}.

The overall algorithm is detailed below, and a flow chart is depicted in Figure 6.2.

1. Solve for new values of unknowns at the $n+1$ timestep. This is performed according to the appropriate algorithm detailed in either Figure 4.2 or Figure 4.3, depending on whether the fully-linear or non-linear theory is being used, respectively.

2. If damage has changed from the n to the $n+1$ timestep, continue; if not, go to last step.

3. Compute the refinement indicators for each cell according to (6.1). Set to zero all refinement indicators for cells with $h \leq h_{min}$.

4. If at least one refinement indicator is greater than zero, continue; if not, go to the last step.

5. Refine all cells with non-zero refinement indicators. Resize/rebuild matrices and vectors. Discard new solution at the $n+1$ timestep and interpolate previous solution from timestep n to new mesh.

6. Go to Step 1.

7. Write data files and proceed to next time step.

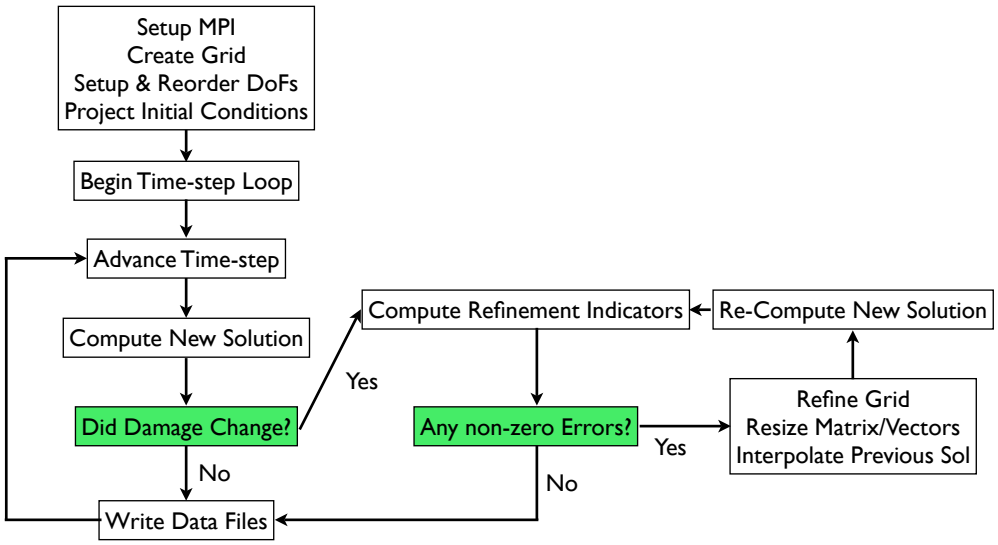

Figure 6.2. Flowchart of the algorithm for AMR based on the refinement indicators computed from the damage. Note that the mesh is refined multiple times per timestep, and every timestep at which damage is evolving, leading to a higher calculation load.

This algorithm contains a loop in which the mesh is refined until all of the cells with non-zero refinement indicators are refined to their smallest size permissible by h_{min}. Damage evolution therefore occurs only at the finest mesh level. Such a scheme ensures that damage is localized to the smallest cell size permitted, and hence the fraction of the domain which is fully damaged is kept to a minimum; however, we note that this is a very demanding refinement scheme, as the mesh will be changed at every timestep during which damage is evolving and with multiple refinement cycles per timestep. Other schemes may require less effort, such as refining only once per timestep, or even only every number of time steps. Such an approach is unsuitable for our needs, as the scale at which the damage evolves has important physical consequences, as discussed in Section 6.2. Additional examples are given in subsequent sections of this chapter.

6.1.2 Energy Release Rate Derived Scheme

As an alternative to the simple damage based refinement indicators given in the previous section, we now describe an algorithm for AMR based on the energy release rate with respect to the damage variable. This quantity is a precursor to damage, and it is supposed that by preemptively refining the mesh, one may be able to better address the localization and mesh dependence of the damage solution. The refinement indicators are calculated from the energy release rate according to

$$r_K = \int_K \langle G - \epsilon_G G_{CR} \rangle \; dK \quad K \in \mathcal{T}_h. \tag{6.2}$$

Here ϵ_G is again a parameter for adjusting the values of r_K. If $\epsilon_G = 1$, then the error indicators are the same as those defined in Section 6.1.1. However, if $\epsilon_G < 1$, we now will have non-zero error indicators, and hence mesh refinement, in parts of the domain that do not have evolving damage. Correspondingly, if $\epsilon_G > 1$, we can force the algorithm to prevent refinement during damage evolution in parts of the domain where $G - \epsilon_G G_{CR} \leq 0$. Thus, via ϵ_G, we can study whether pre-emptively refining the mesh has an impact on the damage evolution.

The overall algorithm is detailed below, and a flow chart is depicted in Figure 6.3.

1. Solve for new values of unknowns at the $n+1$ timestep. This is again performed according to the appropriate algorithm detailed in either Figure 4.2 or Figure 4.3, depending on whether the fully-linear or non-linear theory is being used, respectively.

2. Compute refinement indicators for each cell according to (6.2). Set to zero all refinement indicators for cells with $h \leq h_{min}$.

3. If at least one refinement indicator is greater than zero, then continue; if not, go to the last step.

4. Refine all cells with non-zero refinement indiactors. Resize/rebuild matrices and vectors. Discard new solution at the $n+1$ timestep and interpolate previous solution from timestep n to new mesh.

5. Go to Step 1.

6. Write data files and proceed to next time step.

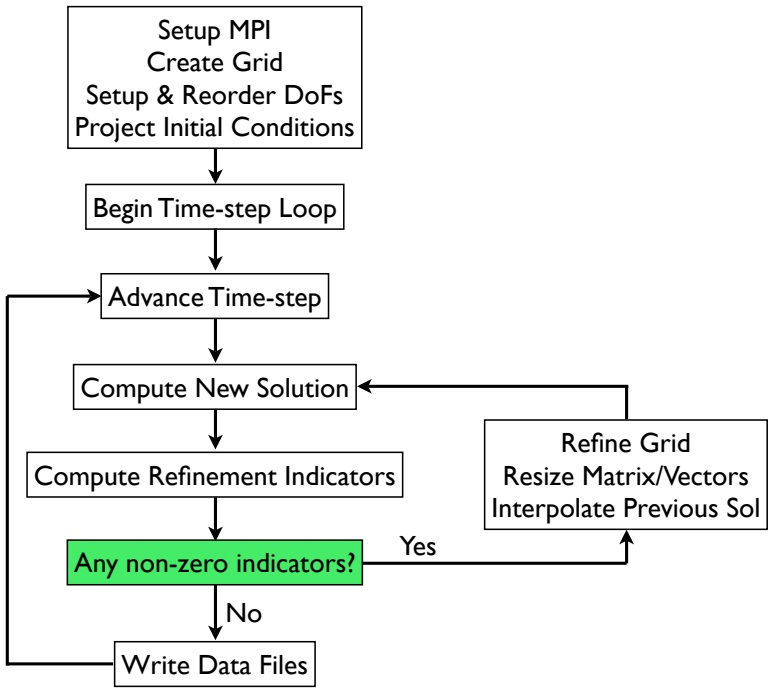

Figure 6.3. Flowchart of the algorithm for AMR based on the refinement indicators computed from the energy release rate (G).

6.2 2D Compact Test Specimen

In this section, an idealized two-dimensional model of a compact test specimen is employed to demonstrate the behavior of the proposed AMR schemes as applied to the model for thermoelasticity with damage. This geometry is well known in the field of fracture mechanics, and thus will allow us to qualitatively analyze the results. All simulations in this section use the theory which is fully-linear when the microstate is fixed, simply to remove further complexity from the simulations and provide clarity in the results. The geometry and boundary condition setup of the compact test specimen (CTS) are given in Figure 6.4. Let $\partial\mathcal{B}$ denote the entire boundary of domain, where the boundary conditions are

$$\mathbf{s}_p(X,t) = \begin{cases} \frac{1}{2}\mathbf{s}_0\left[1-\cos\left(2\pi t/t_0\right)\right] & t < t_0/2 \\ \mathbf{s}_0 & \text{otherwise} \end{cases} \qquad X \in \Gamma_N \tag{6.3}$$

$$\mathbf{s}_p(X,t) = \mathbf{0} \qquad X \in \partial\mathcal{B}\backslash\Gamma_N, \tag{6.4}$$

$$q_p(X,t) = 0 \qquad X \in \partial\mathcal{B}. \tag{6.5}$$

Here $\mathbf{s}_0 = [0, s_y]$, where $s_y = 5\times10^7\,\text{Pa}$, and $\tau_0 = 20\,\mu\text{s}$. These boundary conditions correspond to the body being perfectly insulated boundary and subjected to an

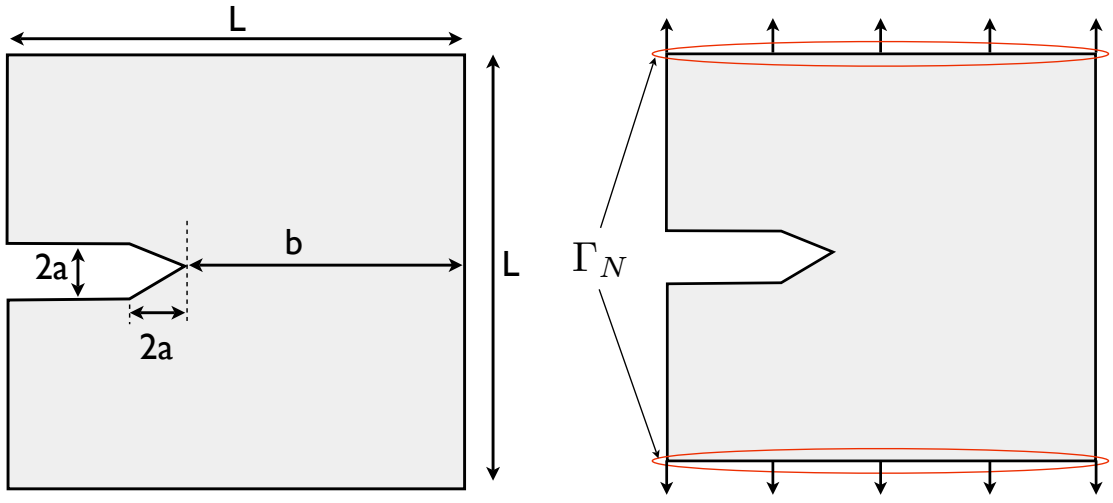

Figure 6.4. The geometry of an idealized 2D compact test specimen and identification of faces on which traction boundary values are applied (denoted by Γ_N). L is taken to be 5 cm, b is 2.5 cm, and a is 0.25 cm. No initial crack is presumed.

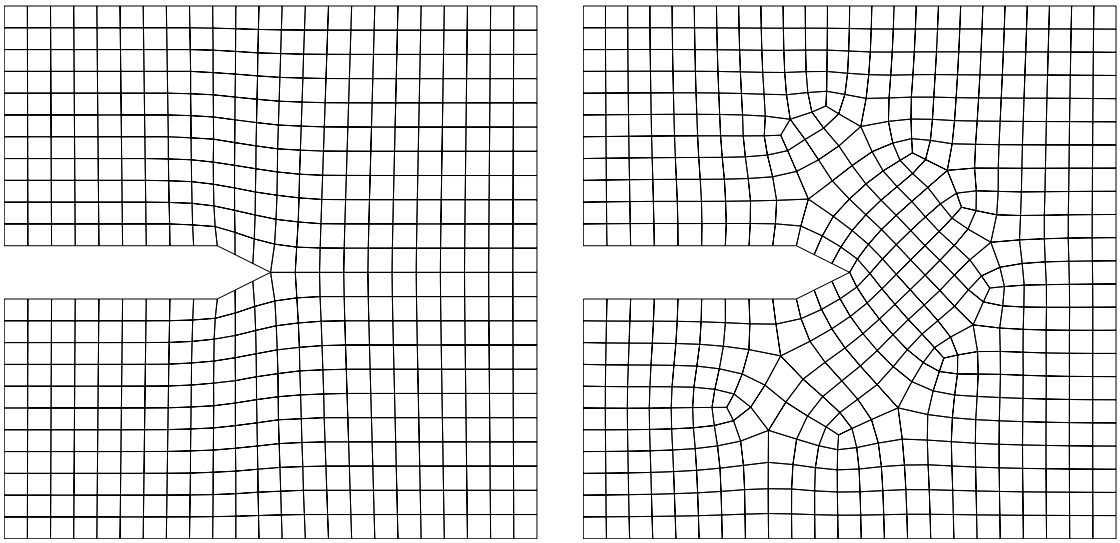

Figure 6.5. Initial meshes for the subsequent simulations. Both meshes were created in Cubit,[‡] with the 'submap' (left) and 'pave' (right) meshing algorithms. These meshes are significantly different, and will serve as a method for comparison of the two AMR schemes, and measure of each scheme in its ability to address the local nature of the solution.

applied force in the vertical direction. Again, the loading happens very quickly, and is held constant after it reaches its maximum value. The meshes we will use to discretize these domains are given in Figure 6.5, and were chosen because one (left) has symmetry about the horizontal axis of symmetry of the domain, while the other does not. These two meshes will provide a measure for comparing the qualitative morphology of the damage field. In this instance, comparing global error norms is not appropriate, as we have not removed the underlying localization of the damage field or its mesh dependent nature. Note that we will refer to these meshes by the algorithms used to create them, as indicated in the caption of Figure 6.5.

As an initial demonstration of the localization problem in higher dimension simulations, we run three simulations with manually refined versions of the submap mesh, the results of which are shown in Figure 6.6. In these simulations, it is clear that the damage localizes to individual cells along the axis of symmetry in the problem. As an artifact of the visualization process, each cell is subdivided, and hence appears as four cells in Figure 6.6; however, it is clear that the damage solution is localizing to individual cells along the horizontal line of symmetry in

[‡]See `http://cubit.sandia.gov` for credit and technical reference.

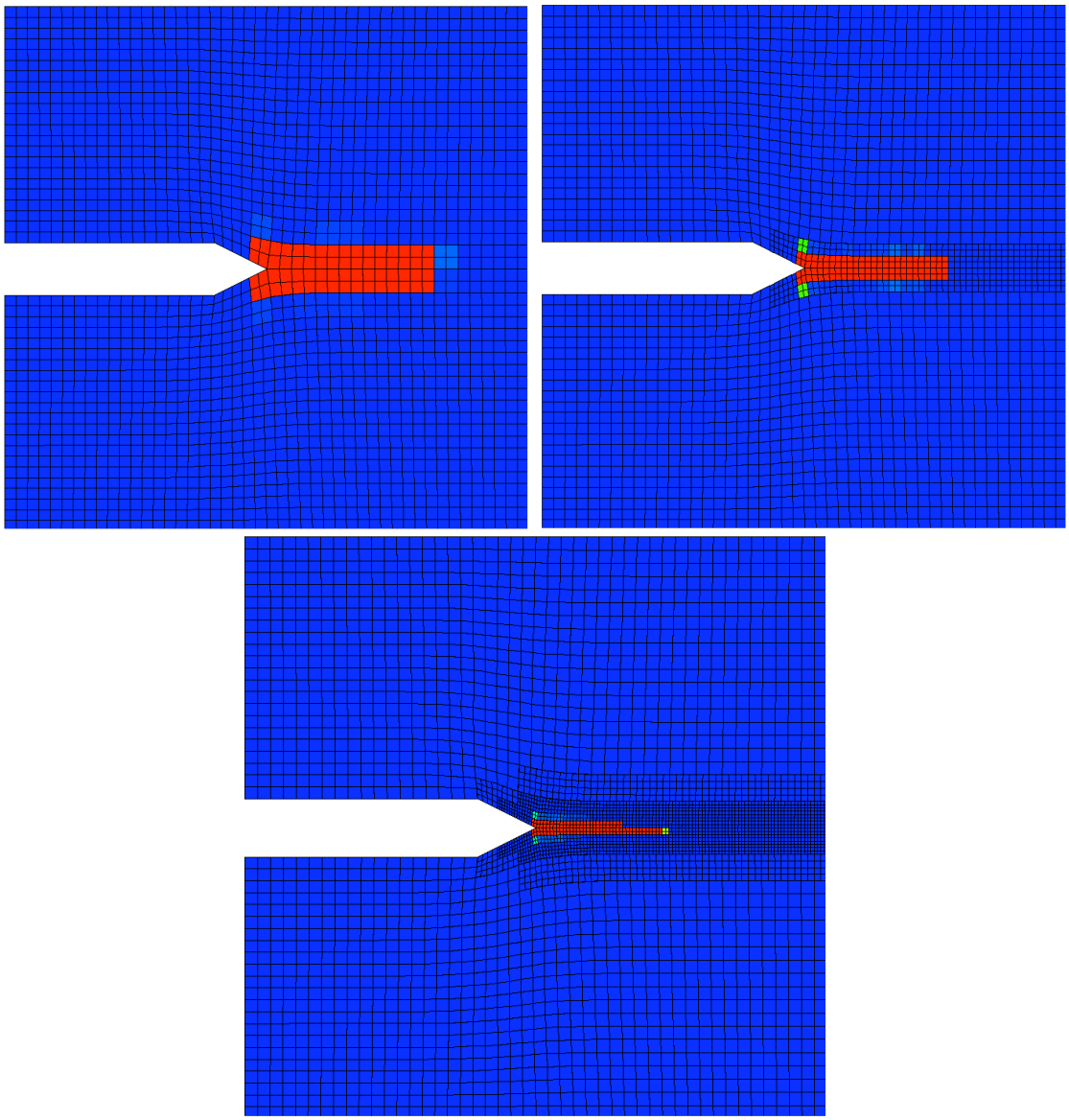

Figure 6.6. The damage field on three grids; one without refinement, and two with manually refinement in the areas of interest. As an artifact of the visualization process, each cell is subdivided once in each direction, and hence appears as four cells in the above images; however, it is clear that the damage solution is localizing to individual cells along the horizontal line of symmetry in the domain. The material properties for these simulations are the same as those for brittle fracture in Section 5.4, i.e., $\beta = 1$, $\alpha = \gamma = 2$, $\tau = 0.025$, $a = 10$, $b = -10$, $\eta_C^0 = 1 \times 10^1\,\mathrm{m}^3/\mathrm{J}\cdot\mathrm{s}$, except that now $G_{CR}^0 = 3 \times 10^6\,\mathrm{J}/\mathrm{m}^3$.

the domain. The material properties for these simulations are the same as those for brittle fracture in Section 5.4, i.e., $\beta=1$, $\alpha=\gamma=2$, $\tau=0.025$, $a=10$, $b=-10$, $\eta_C^0 = 1 \times 10^1\,\mathrm{m}^3/\mathrm{J}\cdot\mathrm{s}$, with the exception that now $G_{CR}^0 = 3 \times 10^6\,\mathrm{J/m}^3$. Again we have employed $\mathcal{P}^0$ elements for the damage solution space, but compared to the results in Chapter 5, we see that the localization is more severe in higher dimensional problems.

As a first attempt at producing repeatable results under which physical studies can be performed, we implement a minimum mesh size. If we choose $h_{\min}$ such that the mesh will generally be refined twice in the area where damage is evolving, employ the damage-based refinement algorithm in Section 6.1.1, and change the critical energy release rate to $G_{CR}^0 = 6 \times 10^6\,\mathrm{J/m}^3$, then we arrive at the damage fields displayed in Figure 6.7. Such calculations are not necessarily encouraging, as it is clear that the solution can display an extreme dependence on the mesh, and even produce damage fields that seem somewhat physically unreasonable. Here we have also changed G_{CR}^0, simply by a factor of two, for the purpose of

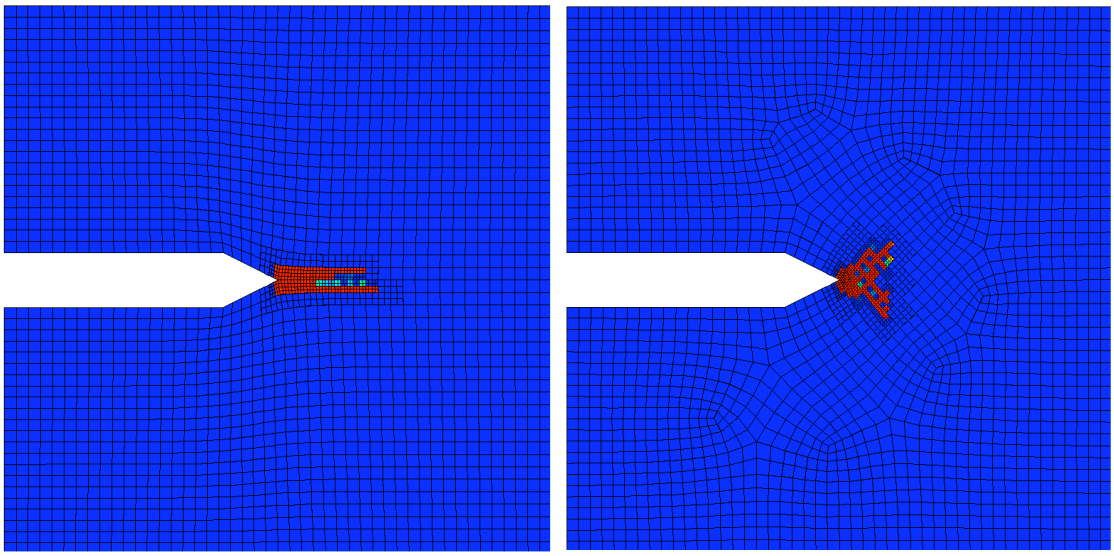

Figure 6.7. The damage field on the meshes generated via the submap (left) and pave (right) algorithm, for the same material properties and loading, using the damage-based refinement scheme with $\epsilon_D = 0$. The mesh dependence of the solution is clear, as well as the fact that the solution generally looks unrealistic. As an artifact of the visualization process, each cell is subdivided, and hence appears as four cells in the above images. The material properties for these simulations are $\beta=1$, $\alpha=\gamma=2$, $\tau=0.025$, $a=10$, $b=-10$, $\eta_C^0=1 \times 10^1\,\mathrm{m}^3/\mathrm{J}\cdot\mathrm{s}$ and $G_{CR}^0=6 \times 10^6\,\mathrm{J/m}^3$.

comparing the damage on the submap-generated mesh (left) in Figure 6.7 and the corresponding image with the highest level of refinement (bottom) in Figure 6.6. We can immediately see the difference in the damage field from a relatively small change in a single material parameter, and subsequently begin to understand that the algorithm is not as robust as desired. At this time, with the current selection of solution spaces and algorithms, the sensitivity to η_C^0, G_{CR}^0, and $h_{\min}$ is quite high, and as such, we need to proceed with caution when making statements or conclusions about future simulations.

We now compare the performance of the damage-based and energy release rate based refinement algorithms presented in Sections 6.1.1 and 6.1.2, respectively. In Figure 6.8, we see the difference in the damage fields generated using the damage based refinement algorithm (Figure 6.8(a)), and the energy release rate based algorithm (Figures 6.8(b)-6.8(d)). As expected, when comparing Figures 6.8(b) and 6.8(d), we see a difference in the number of refined cells, as well as an obvious difference in the damage profile. Although the damage profiles in Figure 6.8 are generally the same, when $\epsilon_G = 0.1$ there are many refined cells with no damage growth, while when $\epsilon_G = 1.5$, we see a smaller number of refined cells and even cells that had evolving damage when their diameter was greater than $h_{\min}$. Of the presented images in Figure 6.8, it does appear that having a value of $\epsilon_G > 1$ yields results that are more qualitatively like those expected from an isotropic compact test specimen under symmetric loading, and thus the remainder of the simulations will use $\epsilon_G = 0.5$.

The solutions in Figure 6.8 demonstrate that a considerable sensitivity exists towards the chosen refinement scheme. This serves to only further aggravate our situation: we are already faced with six parameters about which little or nothing is known, namely, α, β, γ, τ, $\eta_C(\theta)$, and $G_{CR}(\theta)$. We now have the additional concerns about meshing, such as the nature of $h_{\min}$, which refinement indicators to use, how often to refine and so forth. Therefore, at this time it is not appropriate to begin making statements about the specific predictions of the model, and we are forced to accept that we can only make demonstrative claims at this time. Thus, we look for a situation where the proposed adaptive meshing schemes can be demonstrated to be effective, and if such a result is found, we can have some confidence that this approach warrants further study, even if not for a general class

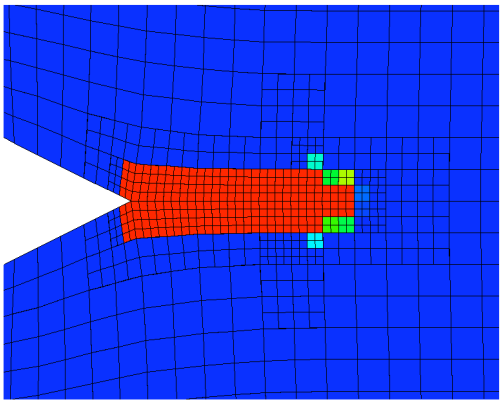

(a) Damage refinement, $\epsilon_D = 0$.

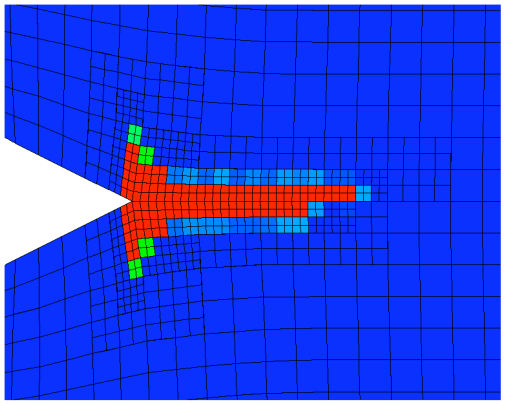

(b) Energy release rate refinement, $\epsilon_G = 0.1$.

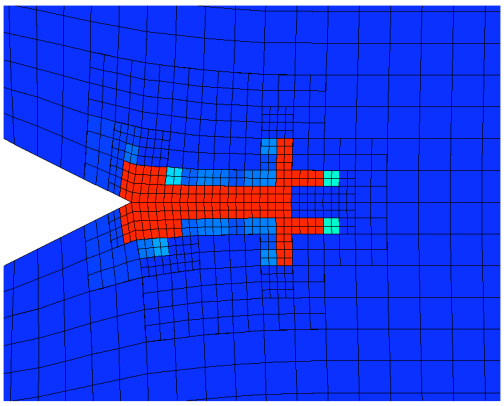

(c) Energy release rate refinement, $\epsilon_G = 1.0$.

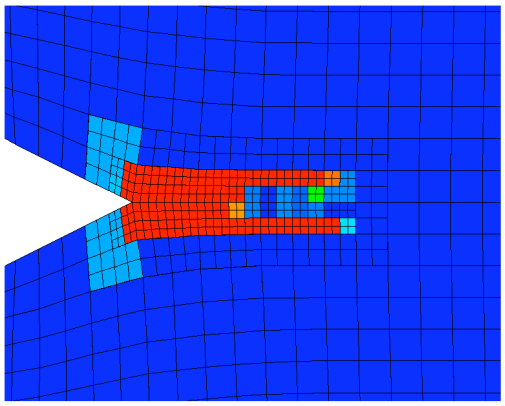

(d) Energy release rate refinement, $\epsilon_G = 1.5$.

Figure 6.8. Zoom-in images of the damage field on the submap mesh for different cases of the refinement indicators, as indicated below each image. Clearly, the solution behaves differently for different schemes, but does appear to be the same in general. Comparing 6.8(b) with 6.8(d), we can clearly see a difference in the number of cells refined. The material properties for these simulations are $\beta = 1$, $\alpha = \gamma = 2$, $\tau = 0.025$, $a = 10$, $b = -10$, $\eta_C^0 = 1\,\mathrm{m}^3/\mathrm{J}\cdot\mathrm{s}$ and $G_{CR}^0 = 9 \times 10^6\,\mathrm{J}/\mathrm{m}^3$.

of problems.

Damage fields are given in Figure 6.9 that, in general, show a solution which appears to be less dependent on the mesh than previous results. Here, the minimum mesh size has been reduced from previous simulations in this chapter, resulting in more refinement. Additionally, the material properties $\eta_C(\theta)$ and $G_{CR}(\theta)$ have been altered as well, such that they are now constant and have the values $\eta_C^0 = 1 \times 10^{-1}\,\mathrm{m}^3/\mathrm{J}\cdot\mathrm{s}$ and $G_{CR}^0 = 8 \times 10^6\,\mathrm{J}/\mathrm{m}^3$. Note that this represents a significant decrease in the value of the crack propagation parameter from the results relating

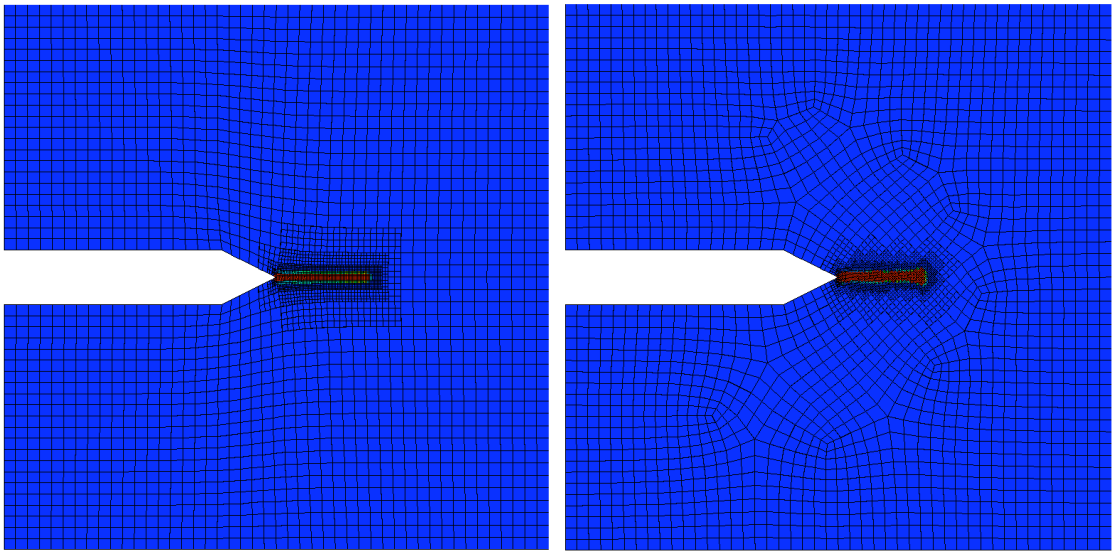

Figure 6.9. The damage field on the meshes generated via the submap (left) and pave (right) algorithm, for the same material properties and loading, using the energy-based refinement scheme with $\epsilon_G = 0.5$. In general, the damage solutions have the same pattern, however, it is not appropriate to call them the same. As an artifact of the visualization process, each cell is subdivided, and hence appears as four cells in the above images. The material properties for these simulations are $\beta = 1$, $\alpha = \gamma = 2$, $\tau = 0.025$, $a = b = 0$, $\eta_C^0 = 1 \times 10^{-1}\ \mathrm{m}^3/\mathrm{J}\cdot\mathrm{s}$ and $G_{CR}^0 = 8 \times 10^6\ \mathrm{J}/\mathrm{m}^3$.

to brittle fracture presented in Section 5; however, it is unclear that a direct substitution of the values used in the one-dimensional model should be subsequently employed in the higher dimensional models. At any rate, the damage field solutions shown in Figure 6.9 are typical of those that are expected from this approach; however, as has been discussed, the algorithm (including refinement techniques and solution space choices) appears to be not as robust as hoped for in generating such solutions.

Zoom-in images of the damage and temperature field for the simulations given in Figure 6.9 are shown in Figure 6.10. Again, we can see that the damage and temperature solutions are in general agreement on the different meshes, but we certainly cannot make the claim that they are quantitatively the same. In Figures 6.10(c)-6.10(d), we again see localized heating in the damage process zone, but due to the piecewise constant nature of the damage evolution, we now see that the largest amount of heating occurs in the interior of the cell. Due to the difference in timescales between the dynamic fracture and thermal phenomena, we

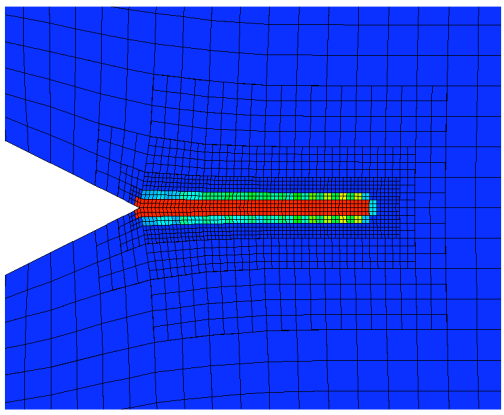

(a) Damage field, submap mesh.

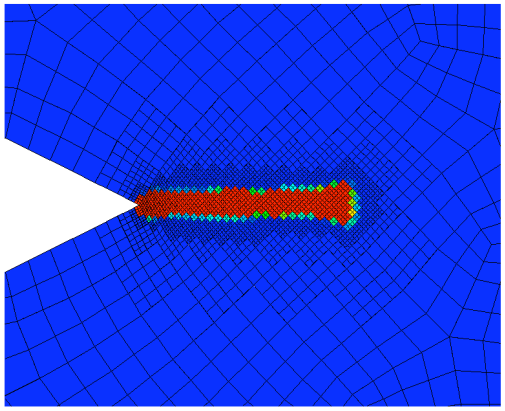

(b) Damage field, pave mesh..

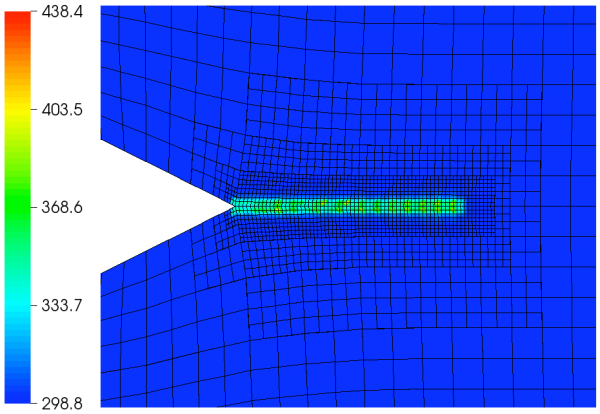

(c) Temperature, submap mesh.

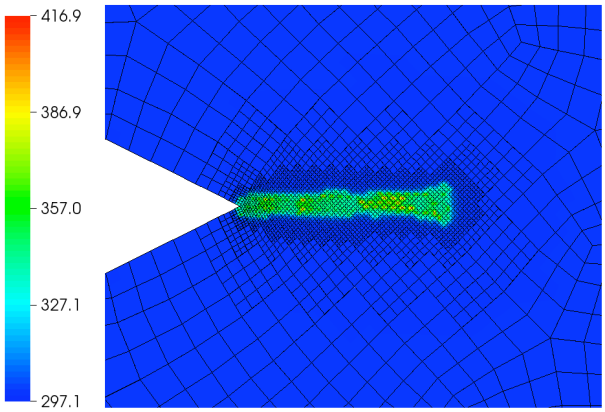

(d) Temperature, pave mesh.

Figure 6.10. Zoom-in images of the damage and temperature fields on the submap and pave mesh. Again, in general the solutions are qualitatively similar; however, they are certainly not the same. Damage induced heating is clear visible in the temperature plots. The material properties for these simulations are $\beta = 1$, $\alpha = \gamma = 2$, $\tau = 0.025$, $a = b = 0$, $\eta_C^0 = 1 \times 10^{-1}\,\mathrm{m}^3/\mathrm{J}\cdot\mathrm{s}$ and $G_{CR}^0 = 8 \times 10^6\,\mathrm{J}/\mathrm{m}^3$.

do not see any diffusion of the temperature into the surrounding material.

Although it seems that reducing $h_{\min}$ has seemed to provide us with more successful results, it is not always necessarily the case. We demonstrate this in Figure 6.11, where the morphology of the damage field is clearly not the same for the submap and pave meshed. The only difference between the images in Figure 6.9 and Figure 6.11, is that in the latter the value of the critical energy release rate has been increased approximately 25 % to $G^0_{CR} = 1 \times 10^7\,\mathrm{J/m^3}$.

In summary, we have been successful in creating an original adaptive meshing scheme that certainly focuses on, and accordingly refines the mesh, in the areas where damage is evolving. Therefore, it seems that we are able to address the issue of localization of damage to single cells rather well; however it is clear that the ability of this scheme to robustly address the mesh-dependent nature of these damage models is not fully developed. Possible explanations for this are either yet unquantified relations between the values of G_{CR}, η_C, and $h_{\min}$, or the fact that a higher order solution space for the damage variable may be appropriate in higher dimensional simulations. At any rate, the work presented in this chapter does encourage us that these issues are worth investigating, and represents an original step forward in the state of the art for dynamic damage model simulations.

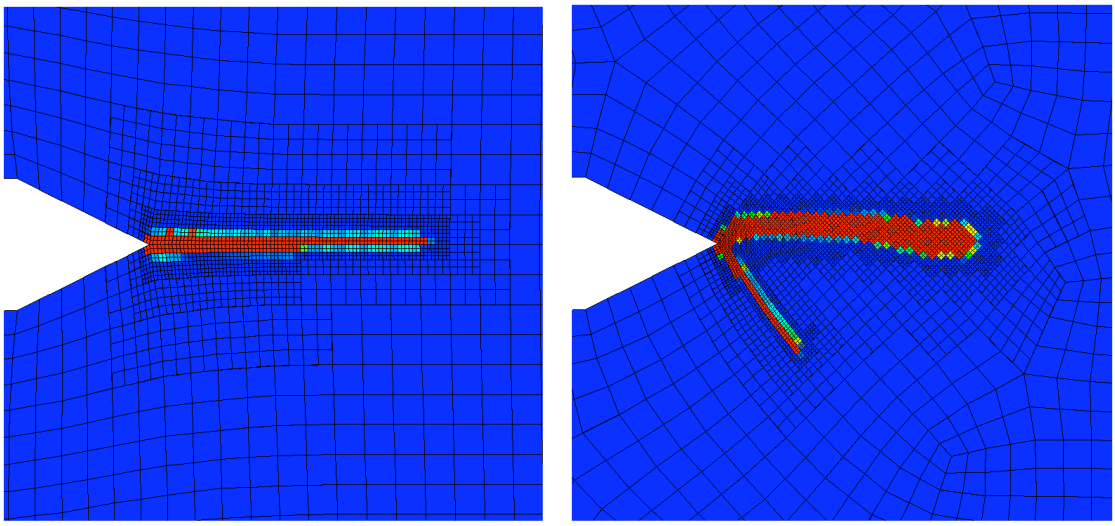

Figure 6.11. The damage field on the meshes generated via the submap (left) and pave (right) algorithm, with everything the same as in the calculations shown in Figure 6.9, except that the value of the critical energy release rate has been increased approximately 25 % to $G^0_{CR} = 1 \times 10^7\,\mathrm{J/m^3}$.

Chapter 7

Conclusions and Future Work

In this chapter, a summary of the tasks completed and conclusions drawn is given, followed by an outline of possible directions for extension. Throughout the discussion, achievements and opportunities are highlighted from physical, numerical, and philosophical points of view.

7.1 Summary of Work

In this thesis, a fully coupled theory of thermoelasticity with damage is derived in the framework of continuum damage mechanics. Throughout the derivation of both the theory that is linear when the microstructure is fixed, and the theory in which the thermoelastic response is intrinsically non-linear when the microstructure is fixed, an emphasis has been made on preserving the important coupling between the constitutive equations and the damage variable. A primary contribution is the idea that, even in linear thermoelasticity with damage, all of the material properties can, and arguably should, be dependent on the damage. Adding to this is the explicit inclusion of a damage evolution induced source term in the balance of energy. To the best of the author's knowledge, this is the first presentation of such a model, in the context of continuum damage mechanics applied to brittle materials.

Two-way coupling between the thermoelastic quantities and microstructure is demonstrated in Chapter 5, and is considered a key result. Here it is shown that heating due to the evolution of the microstructure and the associated dissipation of

energy is present, and has an impact on the evolution of the microstructure as well. It was found, in the context of the proposed physical model, that the dependence of the specific heat on the damage plays a critical role in the thermal-damage coupling. In fact, the role of the specific heat-damage relationship is much more pronounced than that of either the thermal conductivity or thermomechanical coupling with damage. Employing the model proposed in this dissertation allows one to see the impact that dynamic thermal events have on damage evolution; this is an original and important contribution.

The numerical methods proposed herein, where the damage variable is treated as an additional field within the framework of discontinuous finite element methods, is an original contribution to the field of numerical continuum damage modeling. An original application of standard numerical techniques is proposed in this dissertation. The proper solution space for the damage variable was studied, and we eventually settled on piecewise-constant discontinuous finite elements. What could be a stability condition, in terms of combinations of solution spaces in the theory of mixed finite element methods, was empirically identified, and is considered a key result from which future discussions can be launched. Additionally, the use of higher order solution spaces was investigated, and although their performance over all was satisfactory, the resulting non-physical decrease in damage that may occur is highly undesirable. An operator-splitting scheme was introduced to integrate the equations of motion in time. This approach is efficient, and less error-prone then the traditional constrained optimization scheme necessary to properly address the constraints on the damage evolution. Numerical implementations for both the linear and non-linear theories were derived, and good convergence results were achieved for each.

Adaptive mesh refinement (h-refinement) was studied as a potential method for addressing the issues of localization and mesh dependency inherently found in damage models where the damage evolution equation is an ordinary differential equation. To this end, two original refinement indicators were proposed, and implemented into the computer code. The nature of the work addressed in this dissertation called for the construction of a custom adaptive meshing scheme for a dynamic problem. The complexity of such a task is well known in the community of numerical analysis, and as such new schemes and ideas are always considered

important contributions.

In summary, a complete investigation of the necessary theory and numerical techniques for modeling dynamic microstructure evolution within thermoelasticity has been discussed in this thesis. This works fills an often overlooked segment of the literature and knowledge regarding numerical continuum damage modeling. In essence, this thesis provides an examination of the tools available for simulating dynamic microstructure evolution, if one is provided with a detailed damage model of a given material. Whatever this thesis may lack in specificity, in regards to a microstructure-damage model for a specific brittle material, it makes up for in applicability to a general class of models through the thorough consideration of full physical coupling and general numerical methods.

7.2 Findings and Conclusions

This dissertation again confirms that the localization and mesh-dependence of the damage variable fields in continuum damage models is an intrinsic quality of such models, and not an artifact of either poor simulations or insufficient numerical techniques. Throughout this dissertation, great care has been taken to include all possible physical couplings in the equations of motion and to employ modern, well founded numerical techniques. The implementation of these techniques was carefully verified, and yet still we are left with the situation that this class of damage models still exhibits a pathological dependence on the chosen discretization of the domain and extreme sensitivity to loading, initial conditions, and material properties. In addition, even the use of adaptive meshing techniques that are specifically targeted at the damage field did not produce an algorithm which was able to robustly yield repeatable results (i.e., the damage morphology) on different meshes.

From this we can conclude that individual, deterministic simulations are not sufficient for the study of a specific application of this model, and the broader class of local damage models, as the solutions to these problems have shown to be radically non-unique. Rather, statistical studies of aggregate data from many simulations will need to be used to have confidence in a given prediction. This point cannot be over emphasized—even with all of the care taken in this dissertation we

must still resort to statistical studies to have confidence in our predictions. Even then, we must always be mindful of the limits we place on the parameter spaces and the implications that result.

The specific heat's dependence on the damage variable was revealed to be the critical relationship in regards to brittle damage induced heating. From this, we have the most interesting physical prediction of the dissertation: brittle materials in which adiabatic crack propagation is observed will have a specific heat which is not affected by the state of the microstructure. Likewise, materials that posses a specific heat that is dependent on the microstructure will see crack-tip heating purely due to brittle fracture. This is a bold physical statement, and must be viewed in the proper context of brittle failure induced heating (not to be confused with heating due to permanent deformation or phase changes).

A final conclusion of this work is that internal state variables can be treated as actual fields in the formulation, rather than simply as a list of parameters of the material at each quadrature point of the simulation. This is what allowed us to easily implement adaptive mesh refinement, and easily study to the selection of a solution space for the damage field. In this manner, we have demonstrated that, while more questions need to be answered, it is beneficial to regard the damage as a field in some situations.

7.3 Possible Directions for Extension

There are two primary ways in which the work in this dissertation could be extended, corresponding roughly to the point of view of either an engineer or a scientist. From an engineering point of view, there exist a number of refinements of this work that could be done with regards to a specific application. The mathematician may see a number of new questions which may be answered by further analysis; and from the scientist's point of view, there are a number of predictions that have been made in this work that could be cause for the creation of a research program and subsequent validation. Each of these scenarios is explored below.

7.3.1 Future Engineering Work

As stated previously in both the opening introduction and during the derivation of the physical model, many simplifications were made for either ease of implementation or for clarification in studying the behavior of phase-field damage models within thermoelasticity. These assumptions can be relaxed to provide directions for future study. For example, the phase-field damage variable was restricted to be a scalar field and the model did not allow for the independent evolution of some of the properties of the material, such as the individual elastic moduli. Clearly this is only adequate for a limited class of materials. The removal of this limitation of the model should be a priority, as it will be critical in the study of composite materials during dynamic thermal events. Additionally, other well studied phenomena could be included in the model, such as information about the phase of the material and/or plasticity effects. The interplay between the damage variables and these phenomena, in the context of dynamic thermal effects, is sure to be interesting.

Reducing simulation time is incredibly important in the engineering community, and to this extent parallelization has been employed in this work for two and three dimensional models. The main benefits of implementing distributed computing techniques has been speed-up in the assembly of matrices, a decrease in memory consumption per machine by storing the matrices and some vectors across all the cluster nodes, and the use of distributed iterative linear solvers. While these have all resulted in the ability to run larger simulations, there are still problems that prevent the current computer codes from running on larger clusters. The primary issue is that the `deal.ii` finite element library does not support distributed triangulations,* and hence stores a copy of the entire triangulation per processes that is launched. The nature of modern computing environments is such that each cluster node is typically equipped with multiple cores and/or processors. Thus, in a purely distributed code, which is what was implemented in this thesis, one process per available core must be launched on each cluster node, resulting in multiple copies of the triangulation being stored on each node. Clearly, this is undesirable, but can be remedied by implementing hybrid parallel programming techniques. This would result in a code that is distributed, but stores only one copy of the

*This has both advantages and disadvantages.

triangulation per machine on which it is launched while taking advantage of the shared memory parallelization present within each cluster node. Again, developing a framework for these problems would be highly beneficial to the computational community, as this is an ongoing and active area of work.

Finally, perhaps the most practically useful extension of the work contained in this dissertation would be the determination of the precise dependence of the thermoelastic constitutive quantities on the damage field. One can imagine at least three basic routes towards this end. First, analysis and physical reasoning could be used to derive analytical or approximate relationships that are more accurate than the simple ones given in this work. Perhaps more advanced homogenization techniques could be explored towards this end. Second, experimental work could be performed to determine such relationships; however, it is unknown by the author if the complex nature of these measurements is even viable. Finally, a third route could be modeling representative volume elements at the microscale. Necessary to this approach is the detailed knowledge about the microstructure, and the ability to model heterogenous materials and correlate discrete failure mechanisms with the continuum damage field. Such approaches have been proposed and implemented in the literature, and it seems this may be a promising technique for determining the relationship between various material properties and the damage field. Whether the approach be one of those just mentioned or something completely different, it is clear from the work of this dissertation that the dependence of the specific heat on the damage field is important, and is consequently due attention for this work to be applicable to real world scenarios.

7.3.2 Future Scientific Studies

From the point of view of the numerical mathematician, various directions for extension are available. An analytical study of the stability condition, relating to the choice of solution spaces, would be an interesting and original contribution. Further exploring this idea has broader implications for other models that use internal variables, such as those derived via plasticity theories. Determining a method of quantifying convergence, for the case of evolving damage would also be very beneficial; however, at this time it is unclear to the author how to proceed

with such a task. As stated previously, the development of a flexible and efficient non-linear solution scheme for this class of problems would be an enormous benefit to the numerical damage modeling community.

As discussed above, it is clear that single, deterministic simulations will not suffice for making predictions on which design decisions can be based. Therefore, it would be interesting to see what the effects of running many simulations, for the same domain and loading, which randomly varied meshes would produce. One could randomly choose the number of elements, average size of the elements, or even orientation of the elements. The resulting damage morphology from each simulation could be merged with the others, and an ensemble image could be generated which would show what areas are more likely to develop damage than others. This type of result, as opposed to an individual deterministic simulation, could be compared to aggregate experimental data. Hence, this is a possible first step towards the validation of such models.

Returning to the previous section, it would be very interesting to investigate if the predicted relationship between the specific heat/damage and crack-tip heating is true. This would involve a substantial experimental effort, in terms of seeking materials which are brittle and show varying types of crack propagation (i.e., intense heating at the crack tip, some heating, or no heating). Each of these materials would of course have to be fractured, and the real-time dynamic displacement and temperature fields measured. Clearly, this is quite a task. Finally, a concerted effort to quantify the specific heat's dependence on the damage field, for each material, would need to be performed. It is anticipated that this would require theoretical, modeling, and experimental work. Validating this prediction would require more than a single researcher, and in fact would most likely need a devoted program of science.

Appendix A

Thermoelastic Material Properties

The motivation to study the failure of brittle materials at high temperatures in this dissertation is provided partially by the author's involvement in a large Multidisciplinary University Research Initiative (MURI) grant funded by the United States Office of Naval Research (ONR). The topic of this MURI project is Rocket Nozzle Erosion Mitigation (MURI-RNEM), which, as explained in Chapter 1 is critical to the future design of many rocket systems. Sample nozzles have been provided to various groups within the MURI-RNEM project, and these nozzles have been constructed of bulk high density graphite. Thus, I have chosen to use values representative of bulk graphite throughout this thesis.

While graphite is known to exhibit some anisotropic behavior, all of the material data provided to us by the participants in the MURI-RNEM project, as well as other generally available data, has led us to retain an isotropic view of the bulk graphite. The author is aware of the possible shortcomings of this approach, but for the purposes of this dissertation, assuming isotropy is sufficient. Throughout the implementation of the models proposed in this dissertation, care has been taken to allow for anisotropic and heterogenous materials, for the sake of generality that may be required in the future.

Perhaps the most important effect ignored by assuming isotropy, in the context of the graphite rocket nozzles provided to the experimental groups in the MURI-RNEM project, is the aligning of graphite atoms into sheets during the manufacture of the rocket nozzles. This manifests itself in anisotropic material properties, most notably the thermal conductivity, which is higher in plane than out of plane.

Additionally, at approximately 2900 K the graphite undergoes a phase change, resulting in residual stresses and inelastic permanent deformation.

The sources for the material property data include manufacturer supplied information, information available in the open literature, and the work of other groups within the MURI-RNEM project. The high density graphite considered here is the G90-grade material manufactured by Pyrotek*. A table of material properties is available for download on their website, and includes information about the bulk modulus, coefficients of thermal expansion, thermal conductivity, and density at room temperature and at 2315 °C. It does not, however, include information about the specific heat capacity or Poisson's ratio. Thus, for these quantities available data from the open literature were used. Work of other groups in the MURI project has focused on the temperature dependence of the of material properties, and for applied calculations relating to the actual response of the graphite rocket nozzles these data should be used.

Absent from any of these sources is information about the relationship between the material properties and the microstructure of the G90-grade graphite. For this reason, we have had to assume the constitutive response functions in Chapter 3, and explore their effects in the numerical experiments presented in Chapter 5. Finally, as input to the computer codes, we desire all of the values in standard SI units, in the mks system.

Mass Density

The mass density ρ_κ of G-grade high density graphite is given by the manufacturer as 1.87 g/cc at room temperature and 1.86 g/cc at 2315 °C. This is a difference of only about 0.537%, and for our purposes we will assume that the density is constant with respect to temperature. Thus, we have

$$\rho_\kappa = 1.87\,\mathrm{g/cc} = 1870\,\mathrm{kg/m^3}. \tag{A.1}$$

*Pyrotek Inc., 9503 E. Montgomery Ave., Spokane Valley, WA 99206. See `http://www.pyrotek.info/metaullics/` for more information.

Elastic Moduli

The elastic moduli for G-grade high density graphite are determined in part from information provided by the manufacturer and in part from generally available information. The manufacturer provides the modulus of elasticity as "14 K 10^{-5} psi" at room temperature and "27 K 10^{-5} psi" at 2315 °C. We interpret this as the bulk modulus k_{bulk} in pounds-per-square-inch multiplied by 10^{-5}. Thus, we have the bulk modulus as

$$k_{\text{bulk}} = 14\,\text{K}\ 10^{-5}\ \text{psi} = 9.65 \times 10^{9}\,\text{Pa} \quad \text{at } 300\,\text{K}, \tag{A.2}$$

$$k_{\text{bulk}} = 27\,\text{K}\ 10^{-5}\ \text{psi} = 1.86 \times 10^{10}\,\text{Pa} \quad \text{at } 2588.15\,\text{K}. \tag{A.3}$$

While this information is useful, it does not provide all of the necessary information about the elastic response of the material. For example, in order to calculate the Lamé parameters we require one of either the elastic modulus or Poisson's ratio. If we assume a representative value for poisson's ratio of $\nu = 0.3$, then the Lamé parameters can be calculated via the relations given in Sadd (2005), at room temperature

$$\lambda = \frac{3k_{\text{bulk}}\nu}{1+\nu} = 6.68 \times 10^{9}\,\text{Pa}, \tag{A.4}$$

$$\mu = \frac{3k_{\text{bulk}}(1-2\nu)}{2(1+\nu)} = 4.45 \times 10^{9}\,\text{Pa}, \tag{A.5}$$

and at 2588.15 K

$$\lambda = \frac{3k_{\text{bulk}}\nu}{1+\nu} = 1.29 \times 10^{10}\,\text{Pa}, \tag{A.6}$$

$$\mu = \frac{3k_{\text{bulk}}(1-2\nu)}{2(1+\nu)} = 8.59 \times 10^{9}\,\text{Pa}. \tag{A.7}$$

For one-dimension calculations, Young's modulus is used, and is calculated as

$$E = 3k_{\text{bulk}}(1-2\nu) = 1.16 \times 10^{10}\,\text{Pa} \quad \text{at } 300\,\text{K}, \tag{A.8}$$

$$E = 3k_{\text{bulk}}(1-2\nu) = 2.23 \times 10^{10}\,\text{Pa} \quad \text{at } 2588.15\,\text{K}. \tag{A.9}$$

For one-dimensional codes, the elastic modulus is entered directly into the code's parameter file. However, for higher dimension codes we enter the elastic moduli in Voight notation (see, e.g., Malvern, 1969). For example, in two-dimensions this becomes (for an isotropic material)

$$\mathsf{C} = \begin{bmatrix} \lambda + 2\mu & \lambda & 0 \\ \lambda & \lambda + 2\mu & 0 \\ 0 & 0 & \mu \end{bmatrix}. \tag{A.10}$$

Thermal Conductivity

The thermal conductivity of the high density G-grade graphite is given by the manufacturer, at both room and elevated temperatures. We convert these values directly into the desired units.

$$k_{\text{th}} = 101\,\text{BTU/(hr·ft·°F)} = 1.74 \times 10^2\,\text{W/(m·K)} \quad \text{at } 300\,\text{K}, \tag{A.11}$$

$$k_{\text{th}} = 89\,\text{BTU/(hr·ft·°F)} = 1.53 \times 10^2\,\text{W/(m·K)} \quad \text{at } 2588.15\,\text{K}. \tag{A.12}$$

For an isotropic material in our formulation, the thermal conductivity tensor takes the form $\mathbf{K} = k_{\text{th}}\mathbf{I}$, and hence the above values can be directly entered into the code's parameter file.

Specific Heat

The specific heat of high density graphite is not given by the manufacturer of the G-grade material, but approximate ranges are available as general information on various material property databases. Based on the ranges and values found via a quick check of these databases, we select the representative value of $c_v = 700\,\text{J/(kg·K)}$ at room temperature. Based on the discussions with other MURI-RNEM groups, it appears the specific heat of high density graphite increases with temperature, and we select the representative value of $c_v = 800\,\text{J/(kg·K)}$ at 2588.15 K. We can then calculate the specific heat capacity per unit volume as

$$c = \rho_\kappa c_v = 1.31 \times 10^6\,\text{J/(K·m}^3\text{)} \quad \text{at } 300\,\text{K}, \tag{A.13}$$

$$c = \rho_\kappa c_v = 1.49 \times 10^6\,\text{J/(K·m}^3\text{)} \quad \text{at } 2588.15\,\text{K}. \tag{A.14}$$

These values are entered directly into the code's parameter file.

Thermomechanical Coupling

The coefficient of thermal expansion α_{CTE} for high density G-grade graphite is given by the manufacturer. The values are $6 \times 10^{-7}\,1/^{\circ}\mathrm{F}$ at room temperature and $18 \times 10^{-7}\,1/^{\circ}\mathrm{F}$ at 2588.15 K. Converting these values to SI units, we obtain

$$\alpha_{\mathrm{CTE}} = 6 \times 10^{-7}\,1/^{\circ}\mathrm{F} = 1.08 \times 10^{-6}\,1/\mathrm{K} \quad \text{at } 300\,\mathrm{K}, \tag{A.15}$$

$$\alpha_{\mathrm{CTE}} = 1.8 \times 10^{-6}\,1/^{\circ}\mathrm{F} = 3.24 \times 10^{-6}\,1/\mathrm{K} \quad \text{at } 2588.15\,\mathrm{K}. \tag{A.16}$$

For the formulation presented in Chapter 3, we need the thermomechanical coupling tensor, rather than the coefficients of thermal expansion. Additionally, in the formulation in this thesis, for an isotropic material that expands when heated (heats when compressed), the thermomechanical coupling tensor takes the form

$$\mathbf{M} = -\beta_{\mathrm{TM}}\mathbf{I}, \tag{A.17}$$

where $\beta_{\mathrm{TM}} > 0$ is related to the coefficients of thermal expansion by (see, for example, Bowen, 1989)

$$\beta_{\mathrm{TM}} = \alpha_{\mathrm{CTE}}\left(3\lambda + 2\mu\right). \tag{A.18}$$

Thus, we can calculate the thermomechanical coupling at both room and elevated temperatures to be

$$\beta_{\mathrm{TM}} = 3.13 \times 10^{4}\,\mathrm{N}/(\mathrm{m}^2{\cdot}\mathrm{K}) \quad \text{at } 300\,\mathrm{K}, \tag{A.19}$$

$$\beta_{\mathrm{TM}} = 1.81 \times 10^{5}\,\mathrm{N}/(\mathrm{m}^2{\cdot}\mathrm{K}) \quad \text{at } 2588.15\,\mathrm{K}. \tag{A.20}$$

These values are entered directly into the code's parameter file.

Appendix B

Non-Linear Numerical Details

In this appendix the details of the residual defined in (4.71), and the jacobian defined in (4.73) are presented. Recalling the matrix equation in (4.65),

$$\begin{bmatrix} M & 0 & 0 \\ 0 & M^{\rho} & 0 \\ 0 & 0 & M^{c} \end{bmatrix} \begin{bmatrix} \dot{U}^j \\ \dot{V}^j \\ \dot{\Theta}^j \end{bmatrix} = \begin{bmatrix} F_i^{\mathbf{u}} \\ F_i^{\mathbf{v}} \\ F_i^{\theta} \end{bmatrix}, \tag{B.1}$$

where we define each block component as

$$M_{ij} = (\varphi^i, \varphi^j), \qquad M^{\rho}_{ij} = (\rho_\kappa \varphi^i, \varphi^j), \qquad M^{\phi}_{ij} = (\varsigma^j, \varsigma^i), \tag{B.2}$$

$$M^{c}_{ij} = ([(1-\phi_h)^{\tau}(c_0 + c_1\theta_h) - 2\theta_h(1-\phi_h)^{\gamma}\mathbf{M}_1 \cdot \nabla \mathbf{u}_h]\varpi^j, \varpi^i), \tag{B.3}$$

$$F_i^{\mathbf{u}} = (\mathbf{v}_h, \varphi^i), \tag{B.4}$$

$$\begin{aligned} F_i^{\mathbf{v}} = &- \left((\mathbf{I} + \nabla \mathbf{u}_h)(1-\phi_h)^{\gamma}(\mathbf{M}_0 + \mathbf{M}_1\theta_h)(\theta_h - \theta_R), \nabla\varphi^i\right) \\ &- \left((1-\phi_h)^{\beta}(\mathsf{C}_0 + \mathsf{C}_1\theta_h)[\nabla \mathbf{u}_h], \nabla\varphi^i\right) + (\mathbf{b}_\kappa, \varphi^i) + (\mathbf{s}_p, \varphi^i)_A, \end{aligned} \tag{B.5}$$

$$\begin{aligned} F_i^{\theta} = &- \left((1-\phi_h)^{\alpha}(\mathbf{K}_0 + \mathbf{K}_1\theta_h)[\nabla\theta], \nabla\varpi^i\right) \\ &+ (\theta_h(1-\phi_h)^{\gamma}(\mathbf{M}_0 + \mathbf{M}_1(2\theta_h - \theta_R)) \cdot \nabla \mathbf{v}, \varpi^i) \\ &- \left(\gamma(1-\phi_h)^{\gamma-1}(\theta_R\mathbf{M}_0 + \mathbf{M}_1\theta_h^2) \cdot \dot{\phi}_h \nabla \mathbf{u}_h, \varpi^i\right) \\ &+ \left(\tau(1-\phi_h)^{\tau-1}(c_0(\theta_h - \theta_R) + c_1(\theta_h^2 - \theta_R^2)/2)\dot{\phi}_h, \varpi^i\right) \\ &+ (r_\kappa, \varpi^i) + (q_p, \varpi^i), \end{aligned} \tag{B.6}$$

$$F_i^{\phi} = \left(\eta_C \left\langle -\tau(1-\phi_h)^{\tau-1}\left[c_0\left(\theta_h \log\frac{\theta_h}{\theta_R} - (\theta_h - \theta_R)\right) + c_1(\theta_h - \theta_R)^2/2\right]\right.\right.$$

$$+\gamma(1-\phi_h)^{\gamma-1}(\theta_h-\theta_R)(\mathbf{M}_0+\mathbf{M}_1\theta_h)\cdot\nabla\mathbf{u}_h$$
$$+\frac{\beta}{2}(1-\phi_h)^{\beta-1}(\mathsf{C}_0+\mathsf{C}_1\theta_h)[\nabla\mathbf{u}_h]\cdot[\nabla\mathbf{u}_h]-G_{CR}\Big\rangle,\varsigma^i\Big). \tag{B.7}$$

The resulting application of the Crank-Nicholson time integration scheme yields the residual in (4.71),

$$\mathcal{R}(\xi_k^{n+1},\xi^n)=\mathcal{M}(\xi_k^{n+1})\left[\xi_k^{n+1}-\xi^n\right]-\frac{\Delta t}{2}\left[\mathcal{F}(\xi_k^{n+1})+\tilde{\mathcal{F}}(\xi_k^{n+1},\xi^n)\right]. \tag{B.8}$$

As a first attempt at calculating the jacobian, we assume that the quantity $M^c(\xi_k^{n+1})\left(M^c(\xi_k^n)\right)^{-1}\approx\mathbf{I}$. This is not unreasonable, given that material parameters $\mathbf{M}_1$ and c_1 for brittle graphite are expected to be very small and the timestepping can be adjusted to have small increases in damage, even for rapidly growing damage scenarios. This is precisely what would occur if one were to implement a semi-implicit scheme for finding $M^c(\xi_k^{n+1})$, and thus, the scheme about to be described is still a stronger statement than if we were to simply ignore the time dependence of the mass matrix entirely. Hence, the residual is reduced to

$$\mathcal{R}(\xi_k^{n+1},\xi^n)=\mathcal{M}(\xi_k^{n+1})\left[\xi_k^{n+1}-\xi^n\right]-\frac{\Delta t}{2}\left[\mathcal{F}(\xi_k^{n+1})+\mathcal{F}(\xi^n)\right]. \tag{B.9}$$

Since we have still retained the time-dependent nature of the mass matrix, the jacobian of the system is

$$\mathcal{J}(\xi_k^{n+1})=\frac{\partial\mathcal{R}(\xi_k^{n+1},\xi^n)}{\partial\xi_k^{n+1}} \tag{B.10}$$
$$=\frac{\partial\mathcal{M}(\xi_k^{n+1})}{\partial\xi_k^{n+1}}\left[\xi_k^{n+1}-\xi^n\right]+\mathcal{M}(\xi_k^{n+1})-\frac{\Delta t}{2}\frac{\partial\mathcal{F}(\xi_k^{n+1})}{\partial\xi_k^{n+1}}, \tag{B.11}$$

where the jacobian has a block structure

$$\mathcal{J}(\xi_k^{n+1})=\begin{bmatrix}J_{00}&J_{01}&0\\J_{10}&J_{11}&J_{12}\\J_{20}&J_{21}&J_{22}\end{bmatrix}, \tag{B.12}$$

and the entries are computed by:

$$J_{00} = (\varphi^j, \varphi^i) \tag{B.13}$$

$$J_{01} = -\frac{\Delta t}{2}(\varphi^j, \varphi^i) \tag{B.14}$$

$$\begin{aligned} J_{10} = {} & \frac{\Delta t}{2}\left((1-\phi_h^{n+1})^{\gamma}(\mathbf{M}_0 + \mathbf{M}_1\theta_h^{n+1})(\theta_h^{n+1} - \theta_R)\nabla\varphi^j, \nabla\varphi^i\right) \\ & + \frac{\Delta t}{2}\left((1-\phi_h^{n+1})^{\beta}(\mathsf{C}_0 + \mathsf{C}_1\theta_h^{n+1})\nabla\varphi^j, \nabla\varphi^i\right) \end{aligned} \tag{B.15}$$

$$J_{11} = (\rho_\kappa\varphi^j, \varphi^i) \tag{B.16}$$

$$\begin{aligned} J_{12} = {} & \frac{\Delta t}{2}\left((\mathbf{I} + \nabla\mathbf{u}_h^{n+1})(1-\phi_h^{n+1})^{\gamma}\mathbf{M}_1(\theta_h^{n+1} - \theta_R)\varpi^j, \nabla\varphi^i\right) \\ & + \frac{\Delta t}{2}\left((\mathbf{I} + \nabla\mathbf{u}_h^{n+1})(1-\phi_h^{n+1})^{\gamma}(\mathbf{M}_0 + \mathbf{M}_1\theta_h^{n+1})\varpi^j, \nabla\varphi^i\right) \\ & + \frac{\Delta t}{2}\left((1-\phi_h^{n+1})^{\beta}\mathsf{C}_1\nabla\mathbf{u}_h^{n+1}\varpi^j, \nabla\varphi^i\right) \end{aligned} \tag{B.17}$$

$$J_{20} = \frac{\Delta t}{2}\left(\gamma(1-\phi_h^{n+1})^{\gamma-1}(\theta_R\mathbf{M}_0 + \mathbf{M}_1(\theta_h^{n+1})^2)\dot{\phi}_h^{n+1}\nabla\varphi^j, \varpi^i\right) \tag{B.18}$$

$$J_{21} = -\frac{\Delta t}{2}\left(\theta_h^{n+1}(1-\phi_h^{n+1})^{\gamma}(\mathbf{M}_0 + \mathbf{M}_1(2\theta_h^{n+1} - \theta_R))\cdot\nabla\varphi^j, \varpi^i\right) \tag{B.19}$$

$$\begin{aligned} J_{22} = {} & \frac{\Delta t}{2}([(1-\phi_h^{n+1})^{\tau}(c_0 + c_1\theta_h^{n+1}) - 2\theta_h^{n+1}(1-\phi_h^{n+1})^{\gamma}\mathbf{M}_1\cdot\nabla\mathbf{u}_h^{n+1}]\varpi^j, \varpi^i) \\ & + \frac{\Delta t}{2}\left(\left[(1-\phi_h^{n+1})^{\tau}c_1 - 2(1-\phi_h^{n+1})^{\gamma}\mathbf{M}_1\cdot\nabla\mathbf{u}_h^{n+1}\right](\theta_h^{n+1} - \theta_h^n)\varpi^j, \varpi^i\right) \\ & + \frac{\Delta t}{2}\left((1-\phi_h^{n+1})^{\alpha}\mathbf{K}_1\nabla\theta_h^{n+1}\varpi^j, \nabla\varpi^i\right) \\ & + \frac{\Delta t}{2}\left((1-\phi_h^{n+1})^{\alpha}(\mathbf{K}_0 + \mathbf{K}_1\theta_h^{n+1})\nabla\varpi^j, \nabla\varpi^i\right) \\ & - \frac{\Delta t}{2}\left((1-\phi_h^{n+1})^{\gamma}(\mathbf{M}_0 + \mathbf{M}_1(2\theta_h^{n+1} - \theta_R))\cdot\nabla\mathbf{v}_h^{n+1}\varpi^j, \varpi^i\right) \\ & - \frac{\Delta t}{2}\left(2\theta_h^{n+1}(1-\phi_h^{n+1})^{\gamma}\mathbf{M}_1\cdot\nabla\mathbf{v}_h^{n+1}\varpi^j, \varpi^i\right) \\ & + \frac{\Delta t}{2}\left(2\gamma(1-\phi_h^{n+1})^{\gamma-1}\theta_h^{n+1}\dot{\phi}_h^{n+1}\mathbf{M}_1\dot{\phi}_h^{n+1}\cdot\nabla\mathbf{u}_h^{n+1}\varpi^j, \varpi^i\right) \\ & - \frac{\Delta t}{2}\left(\tau(1-\phi_h^{n+1})^{\tau-1}(c_0 + c_1\theta_h^{n+1})\dot{\phi}_h^{n+1}\varpi^j, \varpi^i\right) \end{aligned}$$

Appendix C

Non-Technical Abstract

The design of safe products and structures is a fundamental charge of the engineering discipline. As society continues to demand safer, more efficient and increasingly innovative products, the accurate prediction of product life becomes ever more relevant. This thesis seeks to advance the knowledge available to designers by introducing and analyzing a new model for predicting how brittle materials fail due to a combination of high temperatures, and dynamical mechanical loads.

Brittle materials are those substances that, when they fail, do so by fracturing. Examples of materials that can be considered brittle are glass, at room temperature, and graphite, as found in refillable pencil leads. It has been observed that when such types of materials break, a number of cracks propagate through the material very quickly. At the heart of this crack motion is the physics occurring at the tip of the crack. In particular, very localized heating has been observed, the effect of which can not always be over looked, especially when the fracture occurs in a very high temperature environment. One example of such a situation is that of rocket nozzles constructed of graphite. A primary constraint in the design of such rocket nozzles is that they can only withstand the force of the exiting rocket exhaust for a finite period of time before breaking, and hence sending the rocket off course.

Building and testing rockets is an expensive task, and is detrimental to the environment due to the toxicity of many of the fuel components. As such, it is very beneficial to the design engineers to know what configurations of the rocket nozzle will meet the design criteria before actually constructing the nozzle; however, there currently are only a few methods for making such predictions. In this dissertation,

physical principles are used to derive a new model, that is, a mathematical problem that describes the response of the nozzle to the high-pressure and high-temperature exhaust exiting the nozzle. Physically, we must consider many different processes at work — the conduction of heat, the deformation of the nozzle, and change in the nozzle at smaller scales. The last component is the most challenging, and includes many different physical phenomena all the way down to the atomic scale. We are most concerned with the breaking of the nozzle and therefore focus our attention on the development and propagation of cracks.

Simulating every atom in a nozzle is not feasible given today's current computing resources. Therefore, we turn to physical paradigms and mathematical techniques that allow us to transform the problem into one that can be more efficiently solved. One such branch of study is called *continuum damage mechanics*, and allows us to treat the nozzle, including information about how it is failing at small scales, as a continuous object. The result is a mathematical problem which can be solved by employing one of the many well known methods available for the solution of partial differential equations, while using high performance computing techniques to solve this problem efficiently. An original algorithm is developed in this dissertation for the express purpose of correctly and efficiently representing damage growth.

The results of this dissertation indicate that the coupling of the physical processes involved is crucial to properly predicting the response of brittle materials to external loads. In particular, the relationship between formation and the subsequent growth of cracks is highly influenced by temperature, and vice-versa, through specific properties of the materials. This discovery can help direct experiments to further determine the nature of brittle materials, as well as provide the design engineers with more insight, and hopefully better designed products. A secondary result of this dissertation is the application of various mathematical techniques to problems not usually associated with them, resulting in an expanded set of options for analysts when confronted with such tasks.

Bibliography

Aboudi, J., 1991. Mechanics of Composite Materials. Elsevier.

Acharya, R., Kuo, K., 2007a. Graphite Rocket Nozzle Erosion Rate Reduction by Boundary-Layer Control Using Ablative Materials. In: Proceedings of the 45th AIAA Aerospace Sciences Meeting & Exhibit. 8–11, January, 2007, Reno, NV.

Acharya, R., Kuo, K. K., November-December 2007b. Effect of Pressure and Propellant Composition on Graphite Rocket Nozzle Erosion Rate. Journal of Propulsion and Power 6 (23), 1242–1254.

Agiasofitou, E., Dascalu, C., 2007. Material forces in microfractured bodies. Archive of Applied Mechanics (Ingenieur Archiv) 77 (2), 75–84.

Antonietti, P. F., Heltai, L., 2007. Numerical validation of a class of mixed discontinuous Galerkin methods for Darcy flow. Computer Methods in Applied Mechanics and Engineering 196 (45-48), 4505–4520.

Augusti, G., Mariano, P. M., 1999. Stochastic evolution of microcracks in continua. Computer Methods in Applied Mechanics and Engineering 168 (1-4), 155–171.

Babuška, I., 1971. Error Bounds for Finite Element Method. Numerische Mathematik 16, 322–333.

Babuška, I., 1975. The selfadaptive approach in the finite element method. In: Whiteman, J. R. (Ed.), Mathematics of Finite Elements and Applications. Academic Press, London.

Babuška, I., Rheinboldt, W. C., 1978. Error Estimates for Adaptive Finite Element Computations. SIAM Journal on Numerical Analysis 15 (4), 736–754.

Bangerth, W., Hartmann, R., Kanschat, G., 2006. deal.ii differential equation analysis library, technical reference. Technical report, Texas A&M University.

Bažant, Z. P., 1986. Mechanics of distributed microcracking. Applied Mechanics Reviews 39 (5), 675–705.

Bowen, R. M., 1989. Introduction to Continuum Mechanics for Engineers. Plenum Press.

Brenner, S. C., Scott, L. R., 1994. The Mathematical Theory of Finite Element Methods. Springer-Verlag New York, Inc.

Brezzi, F., 1974. On the Existence, Uniqueness and Approximation of Saddle-Point Problems Arising from Lagrange Multipliers. R.A.I.R.O. 8 (R2), 129–151.

Budiansky, B., O'Connell, R. J., 1976. Elastic-Moduli of a Cracked Solid. International Journal of Solids and Structures 12 (2), 81–97.

Caiazzo, A., Costanzo, F., 2000. On the constitutive relations of materials with evolving microstructure due to microcracking. International Journal of Solids and Structures 37, 3375–3398.

Capriz, G., 1989. Continua with Microstructure. Vol. 35 of Tracts in Natural Philosophy. Springer.

Carlson, D. E., 1972. Linear Thermoelasticity. In: Handbuch der Physik. Vol. 6A. Springer-Verlag, Berlin.

Cermelli, P., Fried, E., Sep 1997. The influence of inertia on the configurational forces in a deformable solid. Proceedings of the Royal Society of London Series A-Mathematical Physical and Engineering Sciences 453 (1964), 1915–1927.

Chaboche, J. L., March 1988a. Continuum Damage Mechanics: Part I—General Concepts. Journal of Applied Mechanics 55, 59–64.

Chaboche, J. L., March 1988b. Continuum Damage Mechanics: Part II—Damage Growth, Crack Initiation, and Crack Growth. Journal of Applied Mechanics 55, 65–88.

Coleman, B., Gurtin, M., 1967. Thermodynamics with internal state variables. Journal of Chemical Physics 47, 597–613.

Coleman, B., Noll, W., 1963. The thermodynamics of elastic materials with heat conduction and viscosity. Archive for Rational Mechanics and Analysis 13, 167–178.

Cortopassi, A. C., Boyer, E., Acharya, R., Kuo, K. K., July 2008. Design of a Solid Rocket Motor for Characterization of Submerged Nozzle Erosion. In: Proceeding of the *44th AIAA/ASME/SAE/ASEE Joint Propulsion Conference & Exhibit.* 21–23 July 2008, Hartford, CT.

Costanzo, F., Walton, J. R., 2002. Steady growth of a crack with a rate and temperature sensitive cohesive zone. Journal of the Mechanics and Physics of Solids 50 (8), 1649 – 1679.

Davis, T. A., June 2004a. A column pre-ordering strategy for the unsymmetric-pattern multifrontal method. ACM Transactions on Mathematical Software 30 (2), 165–195.

Davis, T. A., June 2004b. Algorithm 832: UMFPACK, an unsymmetric-pattern multifrontal method. ACM Transactions on Mathematical Software 30 (2), 196–199.

De, J. P., Gago, S. R., Kelly, D. W., Zienkiewicz, O. C., Babuška, I., 1983. *A-Posteriori* Error Analysis and Adaptive Processes in the Finite Element Method: Part II—Adaptive Mesh Refinement. International Journal for Numerical Methods in Engineering 19, 1621–1656.

Deutsch, F., 2001. Best Approximations in Inner Product Spaces. Springer-Verlag New York, Inc.

Eriksson, K., Estep, D., Hansbo, P., Johnson, C., 1996. Computational Differential Equations. Press Syndicate of the University of Cambridge.

Evans, B., Kuo, K. K., Ferrara, P. J., Moore, J. D., Kutzler, P., Boyd, E., July 2007. Nozzle Throat Erosion Charaterization Study Using a Solid-Propellan Rocket Motor Simulator. In: Proceeding of the *43rd AIAA/ASME/SAE/ASEE Joint Propulsion Conference & Exhibit*. 8–11 July, 2007, Cincinnati, OH.

Fried, E., Gurtin, M. E., 1993. Continuum theory of thermally induced phase transitions based on an order parameter. Physica D 68, 326–343.

Fried, E., Gurtin, M. E., 1994. Dynamic solid-solid transitions with phase characterized by an order-parameter. Physica D. Nonlinear phenomena 72 (4), 287–308.

Gawin, D., Majorana, C. E., Schrefler, B. A., 1999. Numerical analysis of hygro-thermal behaviour and damage of concrete at high temperature. Mechanics of Cohesive-frictional Materials 4 (1), 37–74.

Griffith, A. A., 1921. The Phenomena of Rupture and Flow in Solids. Philosophical Transactions of the Royal Society of London. Series A, Containing Papers of a Mathematical of Physical Character 221, 163–198.

Gurtin, M. E., 1981. An Introduction to Continuum Mechanics. Academic Press, New York.

Gurtin, M. E., 2000. Configurational Forces as Basic Concepts of Continuum Physics. Vol. 137 of Applied Mathematical Sciences. Springer.

Gurtin, M. E., Podio-Guidugli, P., 1996. Configurational forces and the basic laws for crack propagation. Journal of the Mechanics and Physics of Solids 44 (6), 905–927.

Horii, H., Nemat-Nasser, S., 1983. Overall moduli of solids with microcracks: Load-induced anisotropy. Journal of the Mechanics and Physics of Solids 31 (2), 155–171.

Hutchinson, J. W., 1987. Crack Tip Shielding by Micro-Cracking in Brittle Solids. Acta Metallurgica 35 (7), 1605–1619.

Kachanov, L., 1986. Introduction to Damage Mechanics. Mechanics of Elastic Stability. Martinus Nijhoff Publishers.

Kachanov, L. M., 1958. On the Time to Failure under Creep Conditions. Otd. Tekn. Nauk 8, 26–31.

Kachanov, M., 1987. Elastic solids with many cracks: A simple method of analysis. International Journal of Solids and Structures 23 (1), 23–43.

Kelly, D. W., De, J. P., Gago, S. R., Zienkiewicz, O. C., Babuška, I., 1983. *A-Posteriori* Error Analysis and Adaptive Processes in the Finite Element Method: Part I—Error Analysis. International Journal for Numerical Methods in Engineering 19, 1593–1619.

Krajcinovic, D., 1996. Damage Mechanics. Elsevier Science.

Ladevéze, P., 1983. On an anisotropic damage theory. Tech. rep., Laboratoire de Mécanique et Technologie, France.

Lemaitre, J., 1996. A Course on Damage Mechanics, 2nd Edition. Springer-Verlag.

Lemaitre, J., Desmorat, R., 2005. Engineering Damage Mechanics. Springer-Verlag.

Lemaitre, J., Desmorat, R., Sauzay, M., 2000. Anisotropic damage law of evolution. European Journal of Mechanics - A/Solids 19 (2), 187–208.

Lemaitre, J., Sermage, J. P., 1997. One damage law for different mechanisms. Computational Mechanics 20 (1), 84–88.

Liu, I.-S., 2002. Continuum Mechanics. Spring-Verlag, Berlin, Germany.

Majumdar, B. S., Burns, S. J., 1981. Crack Tip Shielding—An Elastic Theory of Dislocations and Dislocation Arrays Near a Sharp Crack. Acta Metallurgica 29, 579–588.

Malvern, L. E., 1969. Introduction to the mechanics of a continuous medium. Prentice-Hall, Englewood Cliffs, NJ.

Mariano, P., 2000a. Premises to a Multifield Approach to Stochastic Damage Evolution. Vol. 410. Springer, Wien, Ch. 6, pp. 217–263.

Mariano, P. M., 2000b. Configurational Forces in Continua with Microstructure. Zeitschrift für angewndte Mathematik und Physik ZAMP 51, 752–791.

Mazars, J., 1996. From damage to fracture mechanics and conversely: A combined approach. International Journal of Solids and Structures 33 (20–22), 3327–3342.

Mazars, J., Pijaudier-Cabot, G., Feb 1989. Continuum Damage Theory — Application to Concrete. Journal of Engineering Mechanics—ASCE 115 (2), 345–365.

Nechnech, W., Meftah, F., Reynouard, J. M., 2002. An elasto-plastic damage model for plain concrete subjected to high temperatures. Engineering Structures 24 (5), 597–611.

Pannwitz, R., Rannacher, R., Bangerth, W., 2003. Adaptive Finite Element Methods for Differential Equations. Birkhauser Verlag.

Pijaudier-Cabot, G., Bazant, Z. P., 1988. Dynamic stability analysis with nonlocal damage. Computers & Structures 29 (3), 503–507.

Quarteroni, A., Sacco, R., Saleri, F., 2000. Numerical Mathematics. Springer-Verlag New York, Inc., New York, NY, USA.

Rabotnov, Y. N., 1963. On the Equations of State of Creep. Progress in Applied Mechanics The Prager Anniversary Volume, 307–315.

Ravi-Chandar, K., Lu, J., Yang, B., Zhu, Z., 2000. Failure Mode Transitions in Polymers under High Strain Rate Loading. International Journal of Fracture 101 (1-2), 33–72.

Sadd, M. H., 2005. Elasticity–Theory, Applications, and Numerics. Elsevier Butterworth–Heinmann.

Simo, J. C., Hughes, T. J. R., 1998. Computational Inelasticity. Springer-Verlag, New York.

Stabler, J., Baker, G., 2000. On the form of free energy and specific heat in coupled thermo-elasticity with isotropic damage. International Journal of Solids and Structures 37 (34), 4691–4713.

Tenchev, R., Purnell, P., 2005. An application of a damage constitutive model to concrete at high temperature and prediction of spalling. International Journal of Solids and Structures 42 (26), 6550–6565.

Truesdell, C., 1965. The elements of continuum mechanics. Springer-Verlag New York, Inc.

Truesdell, C., Noll, W., 1965. Non-Linear Field Theories of Mechanics. In: Flügge, S. (Ed.), Handbuch der Physik. Vol. III. Springer-Verlag, Berlin.

Voyiadjis, G. Z., Deliktas, B., Aifantis, E. C., Jul 2001. Multiscale analysis of multiple damage mechanisms coupled with inelastic behavior of composite materials. Journal of Engineering Mechanics-ASCE 127 (7), 636–645.

Voyiadjis, G. Z., Kattan, P. I., 2005. Damage Mechanics. CRC Press.

Zbolt, J. O., Bazant, Z. P., 1996. Numerical smeared fracture analysis: Nonlocal microcrack interaction approach. International Journal for Numerical Methods in Engineering 39 (4), 635–661.

Zimmerman, R. W., 1985. The effect of microcracks on the elastic moduli of brittle materials. Journal of Materials Science Letters 4 (12), 1457–1460.

Vita

Jonathan S. Pitt

Jonathan Pitt is a native of South Central Pennsylvania, where he was raised and attended high school. He subsequently attended Lebanon Valley College, in Annville, Pennsylvania, where he earned a Bachelor of Science with a double major in Physics and Mathematics in December of 2003. He then attended The Pennsylvania State University for graduate studies, earning a Master of Science in Engineering Mechanics in August of 2005.

Pitt has always had an interest in scientific and technical fields. As early as middle school, he was building simple electronic devices, including a basic intercom system for the family home. His interest then shifted to computers, which eventually led to a part-time job throughout high school and his undergraduate studies repairing computers and supporting the operations of a local internet service provider. During his collegiate education, his interests in mathematics, science, and computers drew him to the field of computational mechanics.

His current research interests include continuum and computational mechanics, with a focus in thermoelasticity and dynamic damage evolution, numerical solution methods for differential equations, solution methods for non-linear systems, and high performance parallel computing.